

2-9-2011

# Ultrafast terahertz spectroscopy and control of collective modes in semiconductors

Denis Seletskiy

Follow this and additional works at: [https://digitalrepository.unm.edu/ose\\_etds](https://digitalrepository.unm.edu/ose_etds)

---

## Recommended Citation

Seletskiy, Denis. "Ultrafast terahertz spectroscopy and control of collective modes in semiconductors." (2011).  
[https://digitalrepository.unm.edu/ose\\_etds/40](https://digitalrepository.unm.edu/ose_etds/40)

This Dissertation is brought to you for free and open access by the Engineering ETDs at UNM Digital Repository. It has been accepted for inclusion in Optical Science and Engineering ETDs by an authorized administrator of UNM Digital Repository. For more information, please contact [disc@unm.edu](mailto:disc@unm.edu).

**Denis V. Seletskiy**

*Candidate*

**Optical Science and Engineering - Physics**

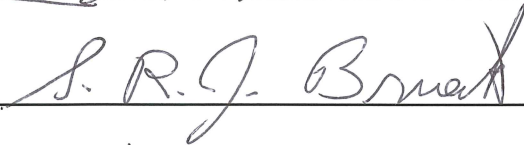
*Department*

This dissertation is approved, and it is acceptable in quality and form for publication:

*Approved by the Dissertation Committee:*

Dr. Sheik-Bahae, Mansour  , Chairperson

Dr. Brueck, Steve R. J.



Dr. Hasselbeck, Michael P.



Dr. Malloy, Kevin J.



---

---

---

---

---

---

---

---

# Ultrafast terahertz spectroscopy and control of collective modes in semiconductors

by

**Denis V. Seletskiy**

B.S., Physics, University of Alaska, Fairbanks, 2001

DISSERTATION

Submitted in Partial Fulfillment of the  
Requirements for the Degree of

Doctorate of Philosophy  
Optical Science and Engineering

The University of New Mexico

Albuquerque, New Mexico

December, 2010

©2010, Denis V. Seletskiy

# Dedication

*To my family*

Nature only uses the longest threads to weave her pattern so that each small piece of her fabric reveals the organization of the entire tapestry.

- R. P. Feynman

# Acknowledgments

I am fortunate and grateful for a chance to learn from my advisor, Mansoor Sheik-Bahae. Under him I had a great opportunity to work on a wide scope of problems and was given freedom to pursue some of my own ones. His unique insight into these problems and timely guidance and advice had been inspiring. Mansoor's encouragement of creative approach has amplified the excitement of pursuing research in our collaboration.

Michael Hasselbeck has become my second advisor and a great collaborator on this journey. His advice and help had been invaluable. His passion for science is addictive and is responsible for my own initial interest in the field of ultrafast terahertz spectroscopy.

I am grateful to have Richard Epstein as my mentor beginning from the time I worked at Los Alamos and throughout my UNM years. I appreciate inspiring discussions with him, Mansoor Sheik-Bahae, and Michael Hasselbeck. All three taught me how to be a good scientist.

I acknowledge unique chance to visit and work in the groups of Alfred Leitenstorfer and Rupert Huber at the Universität Konstanz, Germany. The mere thought of their amazingly supportive, productive, and collaborative research styles motivated me immensely.

A fun place to discuss and hone physical understanding had always been our "Center for amateur Studies." There, many pleasurable and thought provoking discussions with a colleague and friend Doug Bradshaw had served as a nucleation site for many new ideas and personal growth.

I had been fortunate for a chance to have teachers: Sudhakar Prasad, Krzysztof Wodkiewicz, Wolfgang Rudolph, and Nitant Kenkre. I acknowledge help from Luke Emmert, Vasu Nampootheri, Andreas Stintz and Steve Boyd at the UNM as well as from John O'Hara, Daniel Bender, Jeff Cederberg and Rohit Prasankumar at Los Alamos and Sandia National Labs. I savor professional and personal interactions with peers Sasha Neumann, Daniel Bender, Mukesh Tiwari, Animesh Datta, Amarin Ratanavis, Igor Cravechi, Babak Imangholi, Jared Thiede and Mark Mero. Working on day-to-day lab challenges with Chengao Wang, Seth Melgaard, Chia-Yeh Li, Aram Gragossian, Zhou Yang and Mohammed Ghasemkhani was enjoyable. I appreciate manuscript suggestions and insightful comments of my committee Steve Brueck, Mansoor Sheik-Bahae, Michael Hasselbeck and Kevin Malloy. Support from physics department staff and Johh DeMoss at the machine shop was unquestionable.

All would have lost its meaning if not for my family: support of my precious Olya and Danya, my parents, brother, and my grandparents. Dedication of this work to you is my feeble attempt to reciprocate.

# Ultrafast terahertz spectroscopy and control of collective modes in semiconductors

by

**Denis V. Seletskiy**

ABSTRACT OF DISSERTATION

Submitted in Partial Fulfillment of the  
Requirements for the Degree of

Doctorate of Philosophy  
Optical Science and Engineering

The University of New Mexico

Albuquerque, New Mexico

December, 2010



# Ultrafast terahertz spectroscopy and control of collective modes in semiconductors

by

**Denis V. Seletskiy**

B.S., Physics, University of Alaska, Fairbanks, 2001

Ph.D., Optical Sciences and Engineering, University of New Mexico,  
2010

## **Abstract**

In this dissertation we applied methods of ultrafast terahertz (THz) spectroscopy to study several aspects of semiconductor physics and in particular of collective mode excitations in semiconductors. We detect and analyze THz radiation emitted by these collective modes to reveal the underlying physics of many-body interactions.

We review a design, implementation and characterization of our ultrafast terahertz (THz) time-domain spectroscopy setup, with additional features of mid-infrared tunability and coherent as well as incoherent detection capabilities.

Temperature characterization of the collective plasmon excitation in indium antimonide (InSb) is presented to reveal the importance of non-parabolicity corrections in quantitative description. We also obtain electronic mobility from the radiation signals, which, once corrected for ultrafast scattering mechanisms, is in good agreement

with DC Hall mobility measurements. Exhibited sensitivity to non-parabolicity and electronic mobility is applicable to non-contact characterization of electronic transport in nanostructures.

As a first goal of this work, we have addressed the possibility of an all-optical control of the electronic properties of condensed matter systems on an ultrafast time scale. Using femtosecond pulses we have demonstrated an ability to impose a nearly 20% blue-shift of the plasma frequency in InSb. Preliminary investigations of *coherent* control of the electron dynamics using third-order nonlinearity were also carried out in solid state and gaseous media. In particular, we have experimentally verified the THz coherent control in air-breakdown plasmas and have demonstrated the ability to induce quantum-interference current control in indium arsenide crystals.

As a second focus of this dissertation, we have addressed manipulation of the plasmon modes in condensed matter systems. After development of the analytical model of radiation from spatially extended longitudinal modes, we have applied it to analysis of two experiments. In first, we established the ability to control plasmon modes in InSb by means of a plasmonic one dimensional cavity. By control of the cavity geometry, we shifted the plasmon mode into the regime where non-local electron-electron interaction is enforced. We observed the consequential Landau damping of the collective mode, in good agreement with the predictions made within the random-phase approximation. In the second experiment we have invoked plasmon confinement in all three dimensions via a nanowire geometry. We observed enhancement of terahertz emission which we attributed to leaky modes of the waveguide. We attributed this emission to the low-energy acoustic surface plasmon mode of the nanowire, which was also supported by our numerical modeling results and independent DC electronic measurements.

# Contents

List of Figures	xiv
Glossary	xvii
<b>1 Introduction</b>	<b>1</b>
1.1 Motivations . . . . .	1
1.2 Dissertation outline . . . . .	3
<b>2 Experiment I: UF</b>	<b>6</b>
2.1 Overview . . . . .	6
2.2 Femtosecond excitation sources . . . . .	7
2.2.1 Introduction . . . . .	7
2.2.2 Mode-locking . . . . .	9
2.2.3 Ti:sapphire oscillator . . . . .	13
2.2.4 Chirped-Pulse Amplification . . . . .	17
2.2.5 Optical Parametric Amplification . . . . .	20

<i>Contents</i>	xi
2.2.6 Toward higher energies . . . . .	28
<b>3 Experiment II: THz</b>	<b>29</b>
3.1 Historic overview . . . . .	29
3.2 Methods of THz pulse generation . . . . .	33
3.2.1 Photoconducting switch . . . . .	34
3.2.2 Optical rectification . . . . .	38
3.3 Methods of THz detection . . . . .	43
3.3.1 Incoherent detection of THz: bolometer . . . . .	44
3.3.2 Coherent detection: EOS . . . . .	47
3.4 THz-TDS experimental setup . . . . .	49
<b>4 Bulk plasmons</b>	<b>53</b>
4.1 Introduction . . . . .	53
4.2 Plasmons in narrow-gap semiconductors . . . . .	54
4.2.1 Starting mechanisms . . . . .	55
4.3 Spectral characteristics . . . . .	56
4.4 Radiation from a semi-infinite medium . . . . .	57
4.5 Experiments: InSb . . . . .	62
4.5.1 Plasma control: temperature . . . . .	64
4.5.2 Plasma control: photo-doping . . . . .	67

<i>Contents</i>	xii
<b>5 Non-local response</b>	<b>70</b>
5.1 Introduction . . . . .	70
5.2 Landau damping . . . . .	71
5.2.1 Background . . . . .	71
5.2.2 Numerical results . . . . .	74
5.2.3 Experimental results and discussion . . . . .	76
5.3 Acoustic plasmons in nanowires . . . . .	80
5.3.1 Samples and setup . . . . .	80
5.3.2 Experimental results and analysis . . . . .	82
<b>6 Coherent control</b>	<b>92</b>
6.1 Introduction . . . . .	92
6.2 Experimental details . . . . .	94
6.3 Coherent control via third-order optical rectification . . . . .	97
6.4 QUICC in InAs: preliminary results . . . . .	99
<b>7 Concluding remarks</b>	<b>102</b>
7.1 Dissertation summary . . . . .	102
7.2 Future outlook . . . . .	104
<b>A Appx: TEM modes</b>	<b>107</b>
<b>B Appx: Pulse duration</b>	<b>109</b>

<i>Contents</i>	xiii
<b>C Appx: Velocity matching</b>	<b>116</b>
<b>D Appx: Far-field radiation</b>	<b>118</b>
D.1 Lorentz gauge . . . . .	119
D.2 Far-field approximation . . . . .	121
D.3 Dipole radiation . . . . .	122
<b>E Appx: Dielectric function</b>	<b>125</b>
E.1 Plasma frequency . . . . .	125
E.2 Local dielectric function . . . . .	126
E.3 Longitudinal and transverse modes . . . . .	126
E.3.1 Transverse modes . . . . .	127
E.3.2 Longitudinal modes . . . . .	128
E.4 Non-local response . . . . .	128
E.5 Lindhard dielectric function . . . . .	130
<b>References</b>	<b>132</b>

# List of Figures

2.1	Layout of the Ti:sapphire laser cavity in the $z$ -fold configuration. . .	14
2.2	Mode-locked spectra of Ti:sapphire laser for various intra-cavity optics.	15
2.3	Stability of the mode-locked Ti:sapphire laser. . . . .	16
2.4	Schematic of chirped-pulse amplification . . . . .	19
2.5	Schematic of optical parametric amplifier and beam diagnostics . . .	23
2.6	Characterization of the signal pulses from the OPA . . . . .	25
3.1	Schematic of a photoconducting switch . . . . .	34
3.2	Temporal response of a photoconductive switch . . . . .	37
3.3	Phase-matching in ZnTe crystal . . . . .	41
3.4	Optical rectification in $\langle 110 \rangle$ ZnTe . . . . .	42
3.5	THz detection with bolometer . . . . .	45
3.6	THz emission modulated by water vapor absorption . . . . .	47
3.7	Diagram of an electro-optic effect . . . . .	48
3.8	Schematic of THz spectroscopy setup . . . . .	50

3.9	Bandwidth test of the THz-TDS . . . . .	52
4.1	Effect of spot size on the radiation pattern . . . . .	61
4.2	Experimental arrangement for incoherent THz detection . . . . .	63
4.3	Temperature dependent InSb plasma frequency . . . . .	65
4.4	Optical control of the plasma frequency . . . . .	68
5.1	Plasmon dispersion and single-particle excitations . . . . .	72
5.2	Plasmon dispersion in InSb at $T = 1$ K . . . . .	74
5.3	Observation of Landau damping of InSb plasmon . . . . .	77
5.4	SEM image and schematic diagram of the InAs nanowire samples . .	81
5.5	THz emission from bulk compared to InAs nanowires . . . . .	82
5.6	Power dependence of THz emission from InAs nanowires . . . . .	84
5.7	Bulk and nanowire THz emission versus angle . . . . .	86
5.8	Carrier concentration measurement in individual nanowires. . . . .	87
5.9	Dispersion of plasmon modes in InAs nanowires . . . . .	91
6.1	Experimental methods of coherent control . . . . .	95
6.2	Experimental verification of coherent control via SHG interferometer	96
6.3	Coherent control of THz from $\chi^{(3)}$ OR . . . . .	98
6.4	Preliminary results on coherent control in InAs . . . . .	100
A.1	Transverse Hermite-Gaussian modes of the Ti:Sa laser cavity. . . . .	108



C.1	Radiation from the polarization current . . . . .	117
D.1	Calculation of a radiation field from a current distribution . . . . .	120

# Glossary

Ti:Sa	Solid state laser, based on a sapphire crystal doped with titanium ions.
NIR	Near-infrared portion of electromagnetic spectrum.
THz	Terahertz, $10^{12}$ Hz.
FWHM	Full-width at half maximum.
$v_g$	Group velocity.
GVD	Group-velocity dispersion.

# Chapter 1

## Introduction

### 1.1 Motivations

Manipulation of electromagnetic fields at sub-wavelength dimensions is an emerging trend in nanoscience and nanotechnology. This is realized by modification and control of material properties and geometries on the nanoscale [1]. For example, spatial modulation of the real part of the dielectric function impresses Bloch states onto an incident electromagnetic plane wave. This can create a forbidden energy gap, i.e. a semiconductor of light! [2]. In plasmonics, light-matter coupling results in excitation of charge carrier waves at metallic surfaces. This gives rise to new propagation modes of coupled light-plasmon system, resulting in confinement and possibilities of geometric control of the light on the nanoscale [3]. Such exotic manifestations of electromagnetism as negative refractive index and optical cloaking are possible in meta-materials, where both real and imaginary parts of the response can be engineered [4]. The underlying theme of all of these approaches is the control of light and light-matter modes in the materials with engineered nanostructures.

Can we learn more about light-matter interaction and control by scaling the

problem down to low energies?

We argue that at low frequencies, namely terahertz, we can create a platform where fundamental concepts and ideas can be tested on scales that offer relatively easy access. There are several conceptual and technological advantages of such scaling. In this dissertation we motivate these advantages and provide early-stage proof-of-principle experiments that demonstrate our ideas.

Recent progress in metal plasmonics has seen remarkable success in both fundamental studies and application development [3]. Typical metals are characterized by dense gas of free electrons. This situation corresponds to high-energy plasma modes with fundamental frequency that cannot be easily controlled.

A combination of ultrafast terahertz spectroscopy and semiconductor materials offer an interesting complementary system for studies of the physics and engineering aspects of collective mode excitations. In particular to the case of plasmonics, this system offers several key advantages.

*Control of carrier density.* High mobility and high purity are prominent features of narrow-gap semiconductors. This provides the possibility of excitation of highly coherent plasmon modes. Equally important, the carrier density can be controlled in several ways, including sample temperature and crystal growth. Optically injected electron-hole pairs can be made comparable to intrinsic concentrations. This implies that ultrafast control of the plasma density is possible. One can couple plasmons to highly coherent phonon modes, resulting in optical control of the coupled plasmon-phonon system [5, 6]. It is also possible to couple conduction and valence bands of the semiconductor optically [7, 8], resulting in *coherent* control of the collective modes. These possibilities offer a direct path for fundamental as well as engineering studies of condensed matter systems.

*Spatial resolution.* Plasmons in semiconductors can be excited directly with light at optical frequencies. This offers another advantage because the excitation volume

can be minimized by a factor of  $r^3$ , where  $r$  is the ratio of optical to THz frequency. Using optical pulses in combination with engineered semiconductor structures, we envision an ability to efficiently excite, observe, and manipulate plasmons in areas up to a million times smaller than posed by the diffraction limit associated with the plasmon wavelength! [9]

*Coherent detection.* Techniques of ultrafast terahertz spectroscopy (UTS) are ideally suited for studies of the elementary excitations in semiconductors. Tunable broadband THz pulses provide direct access to the ultrafast dynamics at low energies. Full electric field resolution is possible so that the real and imaginary parts of the response can be obtained simultaneously. Recent developments in high-field THz pulse technology [10] offer a possibility of direct control [11, 12] of the collective modes or even possibility of coherently coupling them with the light field itself [13].

The advantages outlined above constitute a set of ideas that have provided motivation for our work. In the next section we outline some of our own efforts that make modest steps in these directions.

## 1.2 Dissertation outline

In this dissertation we apply methods of ultrafast terahertz spectroscopy to study the behavior of collective excitations in condensed matter systems. In particular, we focus on understanding of plasmon modes in narrow-gap semiconductors by characterizing the radiation that they emit. Furthermore, we experimentally demonstrate the possibility of controlling the plasmon modes on both ultrafast and nanometer scales.

The first part of the dissertation is concerned with the experimental apparatus, including the near-infrared excitation sources and details of THz spectroscopy.

- **Chapter 2** is on femtosecond sources. After an overview of the key developments in the field of ultrafast science, we present original contributions on the design of a stable broadband Ti:Sa seeding laser for the amplifier (Section 2.2.3). We conclude the chapter with a novel design and implementation of an optical parametric amplifier (Section 2.2.5).
- **Chapter 3** is on ultrafast THz spectroscopy. After a historical introduction, it proceeds with review of basic principles of THz generation. Some original remarks are made about THz waveform shapes in connection with our data (Section 3.2.2). We discuss and present characterization of incoherent and coherent THz detection schemes employed in this work. We conclude with a presentation of our configurable time-domain THz spectroscopy system.

In the second part of this work we discuss several experiments addressing spectroscopy and control of the plasmon modes.

- In **Chapter 4** we discuss spectroscopy of long-wavelength longitudinal plasmons in narrow-gap semiconductors. After review of the basic physical principles, we present data and analysis temperature-dependent coherent plasmon emission in InSb. We highlight the importance of non-parabolicity in quantitative understanding on the temperature dispersion of the plasma frequency. Non-contact measurement of electronic mobility is demonstrated – this is especially attractive for characterization of the nanoscale devices. We conclude this chapter with results from a pump-probe experiment, where we demonstrate over 15% plasmon frequency shift on a picosecond time scales (Section 4.5.2).
- **Chapter 5** is concerned with the geometric control of the plasmon modes. After brief introduction of the concept of Landau damping, we discuss our experiments where we confine a plasmon to a cavity in one of the three di-

mensions. By progressive shift of the plasmon mode we observe plasmon dispersion and the onset of Landau damping. Experimental results are compared with numerical simulations (Section 5.2). In the second part of this chapter we reduce the plasmon volume further by confining it in two dimensions in a nanowire (Section 5.3). This section is written in a style of a journal article. Here, we show enhanced THz radiation from the InAs nanowires compared to bulk crystal and assign emission to low-energy acoustic surface plasmon modes. Our conclusions are supported by numerical modeling and electrical transport measurements.

- In **Chapter 6** we discuss the possibility of *coherent control* of the collective modes. After brief overview of the theory, we present coherent-control of THz emission from an air-breakdown plasma. We generate and detect hybrid electric fields by performing nonlinear interferometry. We conclude this chapter with preliminary experiments where some evidence of coherent control in bulk InAs is presented.

The concluding **Chapter 7** provides an executive summary and future outlook of the presented work. The dissertation also includes several appendices that contain more technical parts of the discussion. This was done in an attempt to make the presentation more concise and readable.

## Chapter 2

# Experimental techniques I: Femtosecond sources

Knowing is not enough – we must  
apply. Being willing is not enough  
– we must do.

---

Leonardo da Vinci

### 2.1 Overview

Ultrafast science strives to uncover and control the dynamics of the underlying processes governing single and collective particle motions in various phases of matter. This task can only be accomplished if an event (probe) that is shorter than the dynamics of interest can be produced. Short events, such as pulses of electromagnetic radiation can be most naturally produced from repeating events, for instance Bremsstrahlung radiation of accelerating particles in synchrotron ring, i.e. synchrotron radiation [14]. However, a more practical source of pulsed events at optical frequencies is a mode-locked laser. A brief account of techniques to real-



ize short-pulse laser operation will be given below (Sec. 2.2), with the emphasis on the Ti:sapphire (titanium doped sapphire) technology in the near infrared (NIR) spectrum (Sec. 2.2.3).

An important consequence of short pulses is high peak intensity of electromagnetic field, which makes possible to drive nonlinear light-matter interaction processes with high efficiency. In fact, the peak electric field at the focus of a femtosecond source (e.g. from regenerative amplifiers (Sec. 2.2.4)) can greatly exceed the electron binding (Coulomb attraction) field of a typical atom. This would drive the system beyond the perturbative nonlinear response to a new regime where the atom gets completely ionized as a result of the interaction with the laser pulse. Accelerated by the optical wave, these electrons can be arranged to collide with their parent ions, giving off extreme ultraviolet (XUV) [15] and soft X-ray radiation [16] in the process. Advances in this non-perturbative regime of extreme nonlinear optics have led to the development of the new field of attosecond ( $1 \text{ as} = 10^{-18} \text{ s}$ ) science [17, 18, 19] and proposals for table-top laser-driven particle accelerators [20].

## 2.2 Femtosecond excitation sources

### 2.2.1 Introduction

Since the invention of the laser, optical pulse duration has seen a rapid decrease from the millisecond to the attosecond domains [21]. With each new time regime uncovered, we can get a glimpse at physical processes on shorter and shorter timescales, for instance observation of molecular rotations ( $10^{-12}\text{s}$ ), molecular and solid-state lattice vibrations ( $10^{-13}\text{s}$ ) free electron ( $10^{-14}\text{s}$ ) and bound electron dynamics ( $10^{-18}\text{s}$ ).

The method that fundamentally allowed the generation of short [22] and ultimately single-cycle pulses at the NIR frequencies [23] has been termed the

*mode-locking* technique.

Consider an inhomogeneously broadened gain medium which supports pulsed laser action at a number ( $N$ ) of the longitudinal modes, each separated by the free spectral range of the oscillator cavity:

$$\Delta\nu_{\text{FSR}} = \frac{c}{2nL}, \quad (2.1)$$

where  $n \sim 1$  is the refractive index of the cavity of length  $L$  much larger than the laser crystal thickness. The number of lasing modes depends on the gain bandwidth ( $\Delta\nu_g$ ) of the lasing medium, i.e.  $N \approx \Delta\nu_g/\Delta\nu_{\text{FSR}}$ . Thus, we have an equally spaced frequency comb (ignoring dispersion of the refractive index) of  $N$  modes, spanning the envelope of the gain bandwidth of the lasing medium. By the properties of the Fourier transform (for large  $N$ ), the time domain picture is also an equally-spaced comb of the identical pulses, with a separation

$$\tau_{\text{RT}} = \frac{2L}{c}, \quad (2.2)$$

which is the round-trip time of the cavity  $\tau_{\text{RT}}$ . The width of each pulse in the time comb is given by

$$\tau_p = \frac{1}{\Delta\nu_g}, \quad (2.3)$$

reinstating the inverse relationship of the Fourier-transform pairs. This is only true for the case of no dispersion. As discussed in Appx. B, for a case of real material (with dispersion), the two quantities  $\tau_p$  and  $\Delta\nu_g$  are related by the uncertainty principle (Eq. B.6):

$$\tau_p \Delta\nu_g \geq a \quad (2.4)$$

where  $a$  is a constant, depending on the assumed shape of the pulse ( $a = 0.44$  for Gaussian envelopes [24]) and  $\Delta\nu_g$  represents the full-width-half-maximum (FWHM) of the gain bandwidth  $\nu_g$ . The case when the left hand side of Eq. 2.4 is at its minimum is referred to as *transform-limited* pulse (Appendix B).

When performing the mental Fourier transform above we implicitly assumed that there is a definite phase relationship between the  $N$  frequency modes. In a case of a continuous wave (CW) operation, each lasing longitudinal mode oscillates with its own phase. This implies randomness of the output, such that coherence of the time comb is washed out up to the time scales of inverse  $\Delta\nu_{\text{FSR}}$ . This modulation on a longer time scales produces a true CW output. In order to preserve the time comb, a mechanism that maintains definite phase relationship between the modes has to exist. There are numerous experimental techniques that allow to lock the phase of longitudinal modes. These are divided into active and passive mode-locking schemes.

## 2.2.2 Mode-locking

### Methods of active mode-locking

If amplitude- or phase-modulated loss were to be introduced into the oscillator from an external source at multiples of the  $\nu_{\text{FSR}}$ , this would lead to locking of the phases of the modes, resulting in pulsed laser action [25]. This technique, originally referred to as synchronous intracavity modulation. Such approach was pioneered in the 1960's using external electronics to modulate the intra-cavity loss of a HeNe laser [26]. This produced pulses of duration on the order of one (or large fraction) of the cavity length, i. e. about 1 ns. In addition to limited bandwidth of the modulation electronics, HeNe lasers do not have large enough gain bandwidth to support short pulses (Eq. 2.4).

A breakthrough came when continuous wave (CW) lasing was demonstrated in a new medium of Rhodamine 6G organic dye [27], possessing the advantageous properties of large gain bandwidth, low saturation intensity and large emission cross section [28]. Active mode locking in the form of gain modulation by synchronous pumping soon followed, leading to sub-picosecond pulse duration [29]. Despite this progress,

active mode locking was unable to produce pulses much shorter than a picosecond due to the technological limitations imposed by the bandwidth of the various modulation techniques [28]. The passive mode-locking techniques came to the rescue.

### Methods of passive mode locking

Passive mode-locking typically relies on the self-action (nonlinearity) of the intracavity elements. The first implementation of the passive mode-locking occurred in the 1960s and used reversible bleachable dye cells inside of the laser cavity (DeMaria *et. al.* [30]), yielding  $\sim 100$  ps pulse duration. Demonstration of lasing in Rhodamine 6G dye allowed rapid progress, reaching pulse duration of 300 fs by means of a faster saturable absorber [31].

With the invention of the colliding pulse mode-locking (CPM) technique, laser pulse durations were reduced to 90 fs by the beginning of 1980s [32]. In CPM technique, two counter-propagating pulses in a ring cavity are overlapped on a saturable absorber. Transient reduction of the cavity loss favors short pulse formation, since it causes steepening of the leading edges for the interacting pulses. The ultimate limitation of pulse width produced by CPM method is due to the finite response time of the resonant<sup>†</sup> nonlinearity.

### Generation of few-cycle pulses

The gain bandwidth of the dye laser is not large enough to support few-cycle pulses. Reaching pulse durations beyond that allowed by the bandwidth of the gain media (Eq.B.6) requires additional spectral broadening. Such broadening can be generated in a third-order nonlinear process known as *self-phase modulation*. By focusing intense 90 fs dye laser pulses into the glass fiber, Shank *et. al.* were able to ob-

---

<sup>†</sup>meaning that population is generated in the excited state of the system.

tain spectral broadening due to SPM action which after recompression allowed for 30 femtosecond pulses [33]. Shorter than 90 fs pulses directly from the laser were obtained once the importance of minimizing intra-cavity *group velocity dispersion* (GVD, Sec. 2.2.3) had been realized [34, 35] and a simple method to compensate GVD had been developed [36, 37, 24] (Sec. 2.2.3). This led to realization of 30 femtosecond pulses directly from the CPM locked dye laser [38], which, after external SPM in a glass fiber, culminated in the development of 8 femtosecond pulses, i.e.  $\sim 3$  cycles of the carrier wave [39, 40].

### Mode-locking in broadband solid state lasers

In parallel with successes of the mode-locked dye lasers, solid state lasers based on broadband gain spectra of rare-earth and transition metal doped solids have been under intense investigation [28]. Titanium-doped sapphire (Sec. 2.2.3) has the largest known gain bandwidth and in the 1990s proved to be the femtosecond laser of choice in many ultrafast laboratories. Access to the full bandwidth [41] of the gain medium required ultra broadband mode-locking techniques.

A technique of *additive pulse modelocking* in Ti:sapphire laser was tried where loss modulation was achieved by an additional cavity coupled to the main resonator. The extra cavity optics induces temporal distortion (chirp) on the pulse, such that after the injection into the main cavity only the central (un-modulated) portion of the pulse interferes constructively [42, 43]. The drawback of this approach is that the slave cavity needs to be length matched to the lasing cavity to a small fraction of the wavelength, ensuring constructive interference.

Capitalizing on advances in the mature field of semiconductor growth and fabrication passive mode-locking by means of a saturable absorber was revisited in the mid 1990s [24]. Fast *semiconductor saturable absorber mirrors* (SESAM) [44] have been developed to allow state-of-the-art pulses as short as 10 fs to be generated in

Ti:sapphire oscillator [45]. Pulse durations of  $\sim 50$  fs are routinely obtained. The limitation on pulse duration is ultimately imposed by the resonant (and hence slow) nature of the nonlinearity. Due to resonant nonlinearity, SESAMs suffer from low optical damage threshold as well as associated linear losses.

Ultra broadband passive mode-locking has to rely on non-resonant nonlinearity. One consequence of non-resonant third-order nonlinearity is a self-focusing, an optical Kerr effect (AC Kerr effect). Phase shift is induced proportional to the intensity profile of the pulse, leading to formation of a lens in time and spatial domains ([46], Appx. B). The response time is inversely proportional to the bandwidth of the nonlinear process, and for bound electronic nonlinearity it is below a femtosecond. The duration of single cycle of light with wavelength  $\lambda = 800$  nm is  $\sim 2.7$  fs, hence Kerr lens can be considered of instantaneous action. This means that a Kerr lens can be used as an ultra broadband intra-cavity loss modulator, leading to the passive Kerr-lens mode-locking (KLM) technique with virtually unlimited bandwidth. The finding of Kerr lensing in the gain crystal of the Ti:sapphire has lead to the simplest design of a passively mode-locked ultra broadband laser [47] (Sec. 2.2.3). By 1993 pulses as short as 10 fs were demonstrated directly from the Ti:sapphire cavity [22] with GVD compensated by an intra-cavity prism pair.

With the recent advances in dielectric coating technology, it is now possible to produce dielectric-stack mirrors with variable spatial frequency of the alternating coating layers, including so called chirped mirrors [48]. Chirped mirrors can compensate large amounts of positive intra-cavity dispersion at least up to the third order. This is crucial for producing octave-spanning 1.5 – 2 cycle pulses directly from the Ti:sapphire laser [17, 49]. The required bandwidth for such pulses exceeds the gain bandwidth of the Ti:sapphire medium and hence relies on intra-cavity SPM process in the gain crystal to spectrally broaden the pulse beyond the gain medium profile. More exotic examples, such as two-color broadband Ti:sapphire oscillators with sub-30 fs pulse durations have also been implemented [50].

The technology of chirped pulse amplification (Sec. 2.2.4) has increased pulse energy and made it possible to explore SPM and optical parametric chirped-pulse amplification (Sec. 2.2.5) to obtain high energy few cycle in the visible [51] and even single cycle pulses in 2010 in the NIR [23].

### 2.2.3 Ti:sapphire oscillator

By the beginning of 1990s titanium-doped sapphire ( $\text{Ti:Al}_2\text{O}_3$ ) has emerged as the gain medium of choice for femtosecond lasers 2.1. Combined with stable diode-pumped solid-state (DPSS) pump laser and Kerr-lens mode-locking, Ti:sapphire is still the workhorse of most modern day ultrafast laboratories. In this work we used the Asaki *et. al. classic* design of the z-fold Ti:sapphire cavity. The laser crystal is pumped by the CW neodymium doped yttrium vanadate DPSS laser ( $\text{Nd:YVO}_4$ ), producing 532 nm wavelength after intra-cavity frequency doubling. The vanadate is pumped by a diode laser at a wavelength of 808 nm. Our Ti:sapphire pump can produce maximum of 5 Watt output power in the green (Coherent, Verdi 5). The standard output of our Ti:sapphire laser is: 88 MHz repetition rate,  $P_{ML} \sim 500$  mW of mode-locked power ( $P_{CW} \sim 0.7P_{ML}$ ),  $\lambda_0 \sim 790$  nm with a tunable bandwidth of 40-125 nm.

Absorbed 532 nm pump photons promote  $\text{Ti}^{3+}$  ions doped into the Brewster-cut sapphire crystal ( $L_c = 2.5$  mm,  $\alpha(532\text{nm}) \sim 4.4 \text{ cm}^{-1}$ , with figure of merit  $>150$ ) from the ground to the excited state, leading to population inversion after the fast relaxation to the intermediate level. Stable optical resonator [52] (folded asymmetric z-cavity, Fig. 2.1) provides feedback necessary for lasing. The isotropic spontaneous emission from the crystal is collimated by a pair of opposing spherical mirrors (CM1,2). The short collimated arm terminates with a wedged output coupler (OC,  $T \sim 12\%$ ), while the longer contains a pair of Brewster cut fused silica prisms (P1,2) and terminated by a broadband reflector (FM). Astigmatism (and coma) aberration

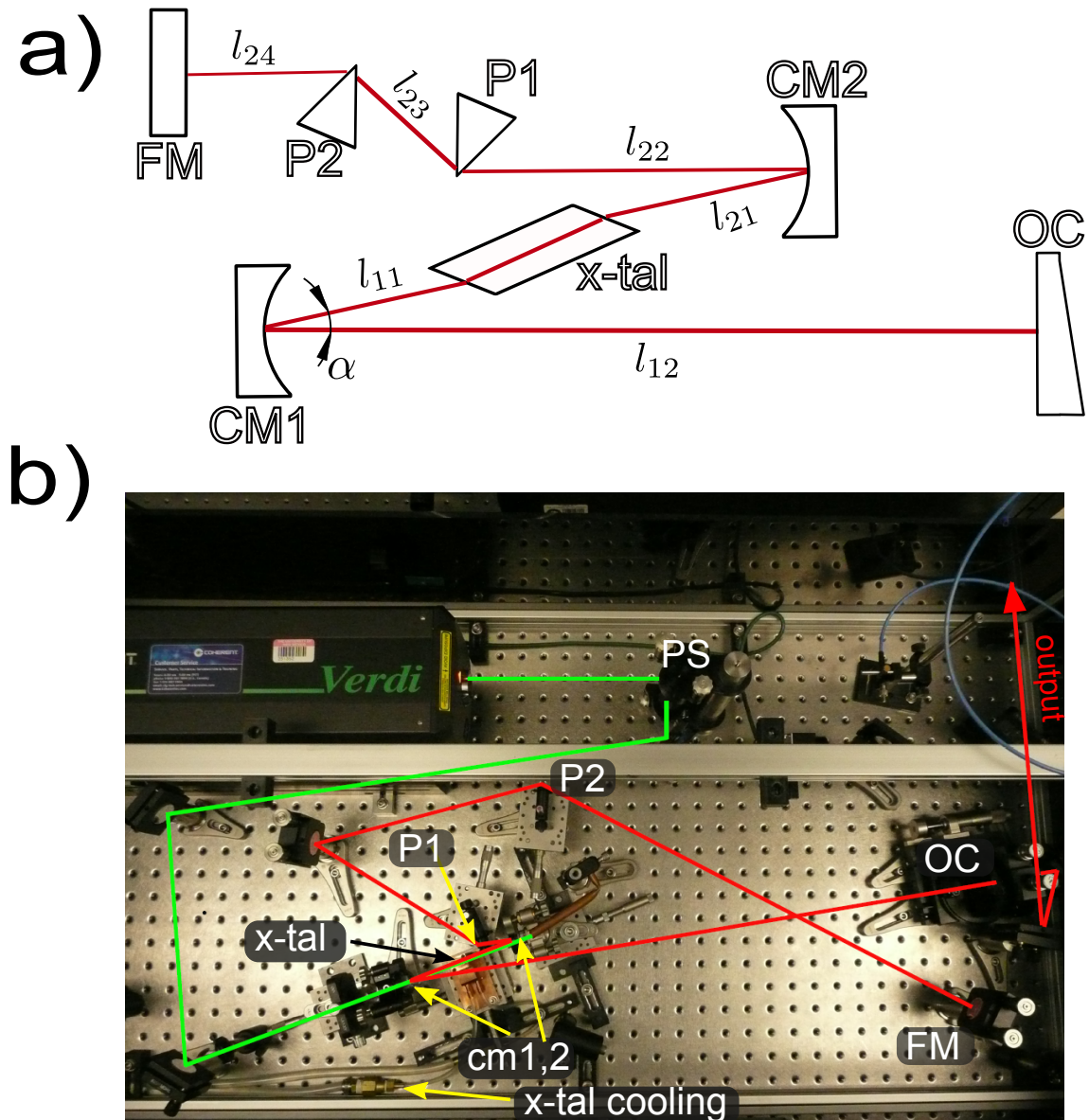


Figure 2.1: Layout of the Ti:sapphire laser cavity in the  $z$ -fold configuration: (a) Schematic of the cavity; (b) Corresponding photograph of the cavity with the main elements labeled.

introduced by the Brewster-cut Ti:sapphire crystal is compensated by the tilt angle



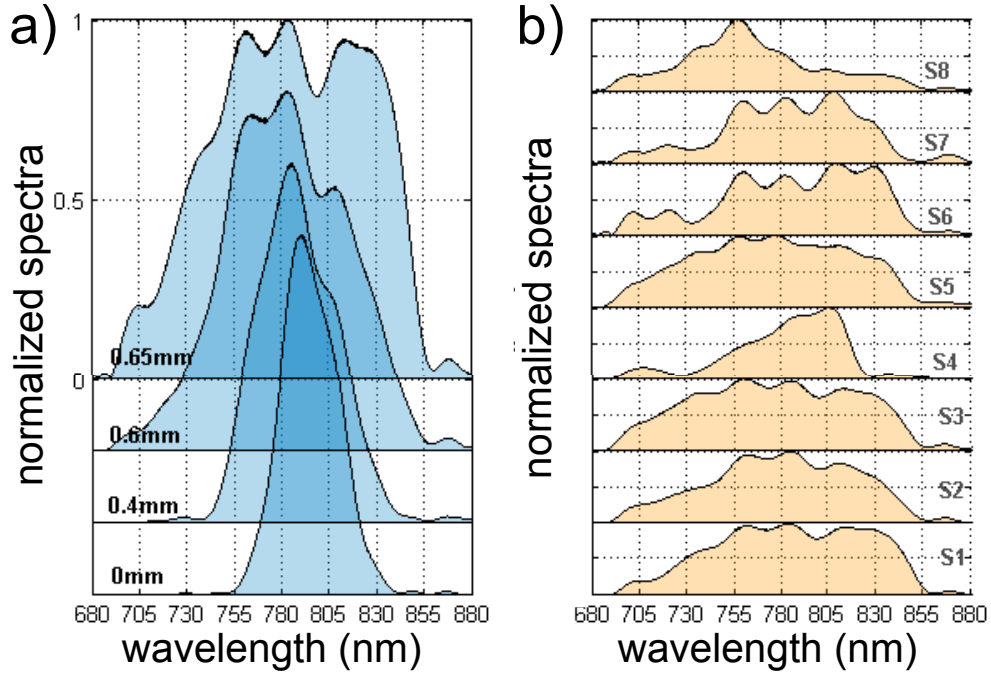


Figure 2.2: Modelocked spectra for various intra-cavity optic elements: (left) Change of mode-locked spectrum as a function of prism insertion. The numbers correspond to prism translation in millimeters; (right) Various mode-locked spectra as obtained for 8 permutations of the cavity mirrors, underscoring importance of mirror coatings for broadband operation of the laser. Spectral oscillations are due to nonuniform reflectivity of the dielectric coatings.

$\alpha$  (Fig. 2.1) of the spherical mirror pair in a z-fold cavity configuration [53]:

$$\alpha = 2 \arccos \left[ \sqrt{\frac{C^2}{4} + 1} - \frac{C}{2} \right] \quad (2.5)$$

$$C = \frac{L_c(n^2 - 1)}{n^4 R} \sqrt{n^2 + 1}$$

where  $n$  is refractive index of the Ti:sapphire crystal and  $R$  is the radius of curvature of the spherical mirrors. With  $n(800\text{nm}) = 1.76$  and  $R = 10$  cm, the resulting angle  $\alpha = 12.0^\circ$  and has resulted in optimized lasing at near  $\text{TEM}_{0,0}$  mode (more information on transverse modes from this laser is presented in Fig. A.1 of Appendix

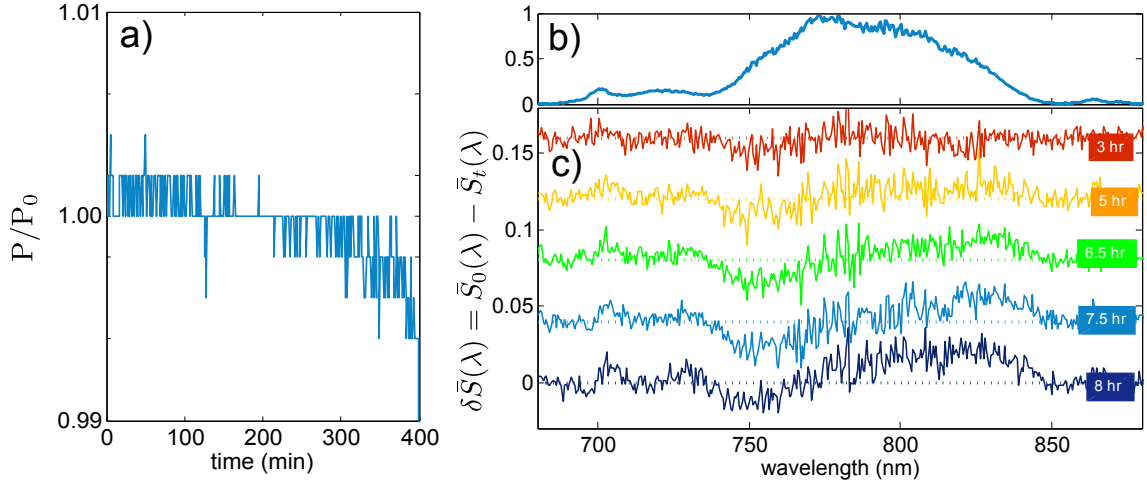


Figure 2.3: Stability of the mode-locked Ti:sapphire laser: (a) Drift of the mode-locked power is less than 1 percent per 6 hours; (b) Mode-locked spectrum and (c) spectral stability of the laser expressed as difference of normalized initial spectrum  $\bar{S}_0$  and spectrum  $\bar{S}_t$  for times  $t$  as shown in the labels,  $|\delta \bar{S}|$  of  $< 1$  percent is observed even after 6 hours of operation.

A).

Mode-locking commences upon external disturbance of a cavity by either moving a prism or an output coupler (on a translation stage). Dielectric cavity mirrors need to maintain low loss across a wide wavelength range to ensure broadband operation of the laser. We have investigated 8 permutations of various intra-cavity mirrors (Newport, CVI) to optimize for the broadest mode-locked spectrum out of the laser (Fig. 2.2b). Optimum configuration  $S3$  (all Newport mirrors) has yielded the maximum mode-locked bandwidth of 125 nm at FWHM, corresponding to transform-limited pulse duration of 7.5 fs (Eq.B.7). The dependence of mode-locked spectrum on the amount of intra-cavity dispersion (affected by the increase of beam path through one of the prisms) for  $S3$  configuration is shown in Fig. 2.2a. Negative GVD introduced by the prism pair is being compensated by the extra amount of prism material to bring the total second order dispersion in a cavity near zero. Laser was designed primarily as a seeding source for a regenerative amplifier, which uses

high dispersion elements to stretch the input pulse for the amplification process (Sec.2.2.4). One of the main design parameters in addition to the broadband operation was the long-term stability of the mode-locked pulse train. The advantageous feature of our design (Fig. 2.1) was to incorporate the pump laser onto the same breadboard as the Ti:sapphire cavity. Additionally, low-thermal conductivity short thick optics mounts resulted in less than 0.5 percent drift in mode-locked power (Fig. 2.3a), as well as less than 1 percent spectral distortion (Fig. 2.3b) over the course of 6 hours of operation.

## 2.2.4 Chirped-Pulse Amplification

Femtosecond pulses are attractive not only for the inherent time resolution but also for the available peak power and possibility to drive light-matter interaction into nonlinear and highly nonlinear regimes. Typical energy per pulse from an oscillator is on the order of several nano Joules, corresponding to instantaneous power of the order of  $\sim 0.5$  MW . Considering 10 fs pulse focused to a spot size of 10 micron (very hard to do!), the oscillating electric field at the focus (0.5 GV/m) is still *only* a fraction ( $\sim 10\%$ ) of the characteristic binding electric field of a valence electron and an atom. While a large perturbation to the atomic field and certainly enough to cause nonlinearity (e.g. second harmonic generation), a much larger electric field is required for non-perturbative regime of nonlinear optics (Sec. 2.1). Therefore researchers have been interested in various ways of amplifying these pulses.

Amplification techniques can be divided into passive and active. The easiest way to increase the energy per pulse is to decrease the repetition rate of the laser (at the same average power). Such effective amplification has been demonstrated by Ippen *et. al.* to produce 17 fs pulses with peak powers of  $\sim 1$  MW at repetition rates of 15 MHz [54]. Kerr-lens mode-locking is unaffected in such long cavities by utilizing multi-pass Herriott cell [55] with unity magnification, resulting in effective

zero thickness of the element and thus leaving KLM cavity design unchanged.

Another example of passive amplification is a technique termed *cavity dumping*, where an output coupler of a Ti:sapphire laser (Sec. 2.2.3) is replaced by a highly-reflective mirror, increasing the single-pass gain of the laser cavity. Once transient gain reaches saturation, an intra-cavity acousto(electro)-optic modulator redirects an amplified pulse out of the cavity, as long as the reaction time of the modulator is faster than one cavity round-trip. Cavity dumping has been demonstrated to produce sub-20 fs pulses of instantaneous power in excess of 10 MW at repetition rates of 0.1-4 MHz [56, 57]. Since amplification of the pulse occurs without external input (aside from the energy expenditure for modulation) this amplification technique is passive.

In active amplification techniques low energy pulses from the oscillator are allowed to pass through an amplifying crystal (also Ti:sapphire), which has been inverted by the action of the external pump laser (typically pulsed). This results in amplification of the seed pulse. A cw-pumped, cavity dumped Ti:sapphire with subsequent direct multi-pass amplification can produce 12 fs pulses at energies in excess of 200 nJ [58], corresponding to peak power of nearly 20 MW, but already requires cooling to 200 K to avoid thermal lensing. Such instantaneous power starts to approach regime of strong pulse self-focusing and ultimate damage of the amplifying crystal.

In the effort to avoid high peak power, in 1985 Mourou *et. al.* applied the technique of *chirped pulse amplification*, CPA [59] in the optical frequencies. The basic idea is to significantly stretch a pulse before the amplification, in the process lowering its peak power. Upon subsequent recompression pulse duration can be nearly restored, subject to the gain bandwidth of the amplifier, thus resulting in highly amplified pulses with avoided parasitic nonlinearities and damage of the gain medium. By the early 1990s instantaneous powers of TW ( $10^{12}$ ) have been demonstrated [60, 61].

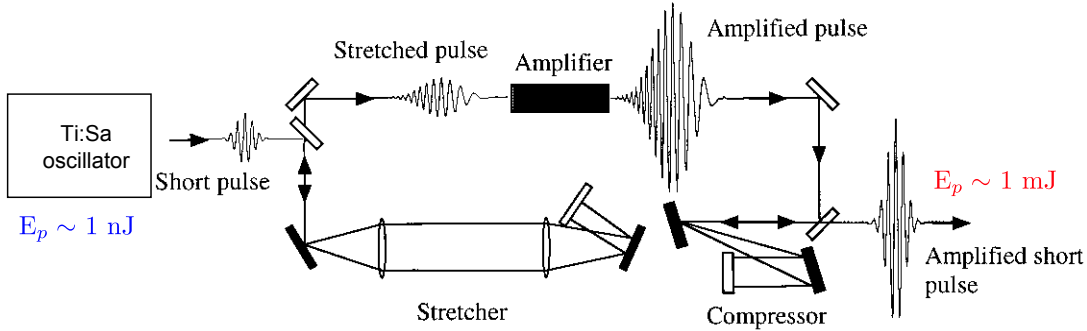


Figure 2.4: Schematic of chirped-pulse amplification: a low energy pulse from an oscillator cavity is stretched in a grating-pair stretcher to nearly one nanosecond. Stretched pulse is sequentially amplified in an inverted gain medium (Ti:sapphire crystal) by factor of  $\sim 10^6$ , reaching  $\sim 1 \text{ mJ}$  energy. In the final stage, stretched pulse is recompressed to peak power levels on the order of  $\sim 1 \text{ TW}$  (Figure is adapted from Fig. 1 of Ref. [62]).

A general scheme of the CPA is depicted in Fig.2.4. Amplification of the stretched pulses can either be performed in multi-pass geometries (multi-pass amplifiers) , or in resonant cavities (regenerative amplifiers).

In this work we utilized commercial regenerative amplifier system by Coherent (Legend Elite). The amplifier is seeded by a homebuilt oscillator (Sec. 2.2.3) and pumped by Q-switched intra-cavity doubled Nd:YLF DPSS laser, producing 20 mJ pulses at 527 nm with 1 kHz repetition rate. Pump pulse duration of 250 ns allows to efficiently amplify a train of stretched seed pulses by factor of a million. A combination of input and output electro-optic elements (Pockels cell) allow to inject and eject the seed pulse from the amplifier cavity. External grating-pair allows to compress pulses to transform-limited duration of 33 fs (32 nm bandwidth centered at 795 nm) at pulse energies up to 3.5 mJ at 1 kHz, corresponding to peak power of  $> 0.1 \text{ TW}$ .

There are numerous techniques to scale peak powers into the unprecedented Peta-

Watt regime ( $10^{15}$ ), but these are outside of the scope of this work. At these powers, laser-based linear particle accelerators and non-relativistic optic regimes are proposed to be explored [20].

## 2.2.5 Optical Parametric Amplification

While a great success, limiting characteristics of chirped-pulse amplifiers are still low peak powers and tunability. After all, the amplification process relies on a resonant transfer of energy from the pump laser to the seed source mediated by the Ti:sapphire crystal, the amount of energy being subject to the material parameters. In addition, operation only in the regions of 800 nm or frequency-doubled 400 nm is possible, again dictated by the natural resonance of the gain medium. One way to boost peak powers even further is to employ a non-resonant energy transfer - a nonlinear process where initial and final states of the *virtual* transition are the same [63]. Nonlinear response of a transparent dielectric medium is manifested through coupling of photons of different frequencies to produce a frequency-mixed output photon. Because of the virtual nature of the excitation, tunability is greatly extended as no longer limited by the natural resonances of the medium. Since no population is generated in virtual process, nonlinear amplification has much larger saturation threshold than in the case of Ti:sapphire amplifier.

### General principle

In the lowest (second) nonlinear-order process two photons couple through a anharmonicity of the induced polarization in the dielectric to produce a third photon at sum or difference frequency as well as frequency-doubled photons at each input frequency. Consider a situation where both high-intensity high-frequency *pump* beam at  $\omega_p$  and a weak-intensity low-frequency *signal* beam at  $\omega_s$  are coincident onto a suitable nonlinear crystal. In such scenario, weak signal beam will get amplified

by extracting energy from the pump beam, at the same time a third beam at *idler* frequency will be generated,

$$\hbar\omega_p = \hbar(\omega_s + \omega_p) \quad (2.6)$$

as a consequence of energy conservation ( $\omega_i < \omega_s$  by convention). For this interaction to be efficient, momentum conservation has to be satisfied simultaneously (phase-matching condition)

$$\hbar\mathbf{k}_p = \hbar(\mathbf{k}_s + \mathbf{k}_i) \quad (2.7)$$

where  $\mathbf{k}_{p,s,i}$  are the wavevectors of pump, signal and idler beams. From Eq. 2.6, signal beam is tunable from  $\omega_p$  to  $\omega_p/2$ , while idler from  $\omega_p/2$  to 0. In practice, low-frequency region can not be easily accessed due to the onset of the mid-IR absorption band of most crystals. In addition to momentum conservation, such nonlinear process is naturally more efficient for very high intensities and therefore is suitable for femtosecond pulses. This further implies that for such interaction to occur pump and signal pulse have to be overlapped in both space and time. Furthermore, the difference of their group velocities, or their *group velocity mismatch* (GVM) has to be small in order to maximize their overlap and hence parametric amplification.

## OPO

Signal pulse does not have to be present for this process to occur. Optical parametric generation (OPG) can self-start from fluctuations of zero point energy of vacuum. This fact is utilized in *optical parametric oscillators*(OPO), where an optical cavity resonant at one or both of the down-converted frequencies is placed around a non-linear crystal [64]. Just like in a laser, certain pumping level is required to overcome oscillation threshold associated with the losses of the cavity. OPOs have proven as robust and efficient widely tunable sources of electromagnetic radiation, a standard off-the-shelf product offered at various power, wavelength and repetition rate

regimes, enabled by a multitude of highly efficient nonlinear crystals. Just to give few very sparse and more recent examples from the research literature, multi-Watt oscillation has been demonstrated under pumping with CW [65, 66], picosecond [67, 68] and femtosecond [69, 70] pulses, with efficiencies as high as 50 - 90% in some cases and wavelengths covering from ultraviolet to mid-infrared. The main drawbacks of OPOs are relatively low output pulse energy, necessity for synchronous pumping and limited tunability range, limited by mirror coating bandwidth [71].

## OPA

If single-pass parametric gain is high enough then resonator cavity is no longer required. Optical parametric amplification (OPA) is performed with intense pulses and typically requires one or two passes through a nonlinear crystal to reach high conversion of the pump photons into the amplified signal and/or idler photons. There is a multitude of OPA schemes, depending on the wavelength range of interest and desired tunability range, determined by the nonlinear crystal properties such as phase-matching (birefringence), transparency range and damage threshold [71]. Conveniently pumped by the fundamental of the Ti:sapphire laser ( $\sim 800$  nm) OPAs are efficient sources femtosecond pulses in the mid-infrared range [72]. A novel class of mid-infrared OPAs has been emerging relatively recently with the discovery of a novel nonlinear optic crystal bismuth triborate ( $\text{BiB}_3\text{O}_6$ ) [73]. The BiBO crystal belongs to borate family of crystals, possessing large  $\chi^{(2)}$  nonlinearity. Examples of borate family include for instance well-known nonlinear crystals of beta barium borate ( $\beta\text{-BaB}_2\text{O}_4$ , BBO) and lithium triborate ( $\text{LiB}_3\text{O}_5$ , LBO). Advantages of BiBO crystal are its particularly large effective nonlinearity [74, 75] as well as extended transparency range [76].

In this work we implement 2-stage optical parametric amplifier with design guided by the designs of Ghotbi *et. al.* [77, 73, 78]. A schematic of the amplifier is depicted



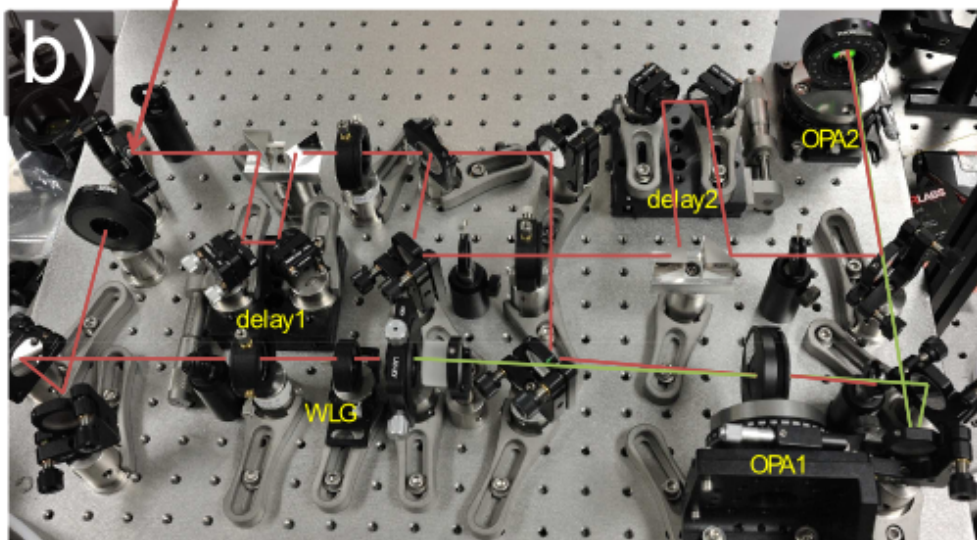
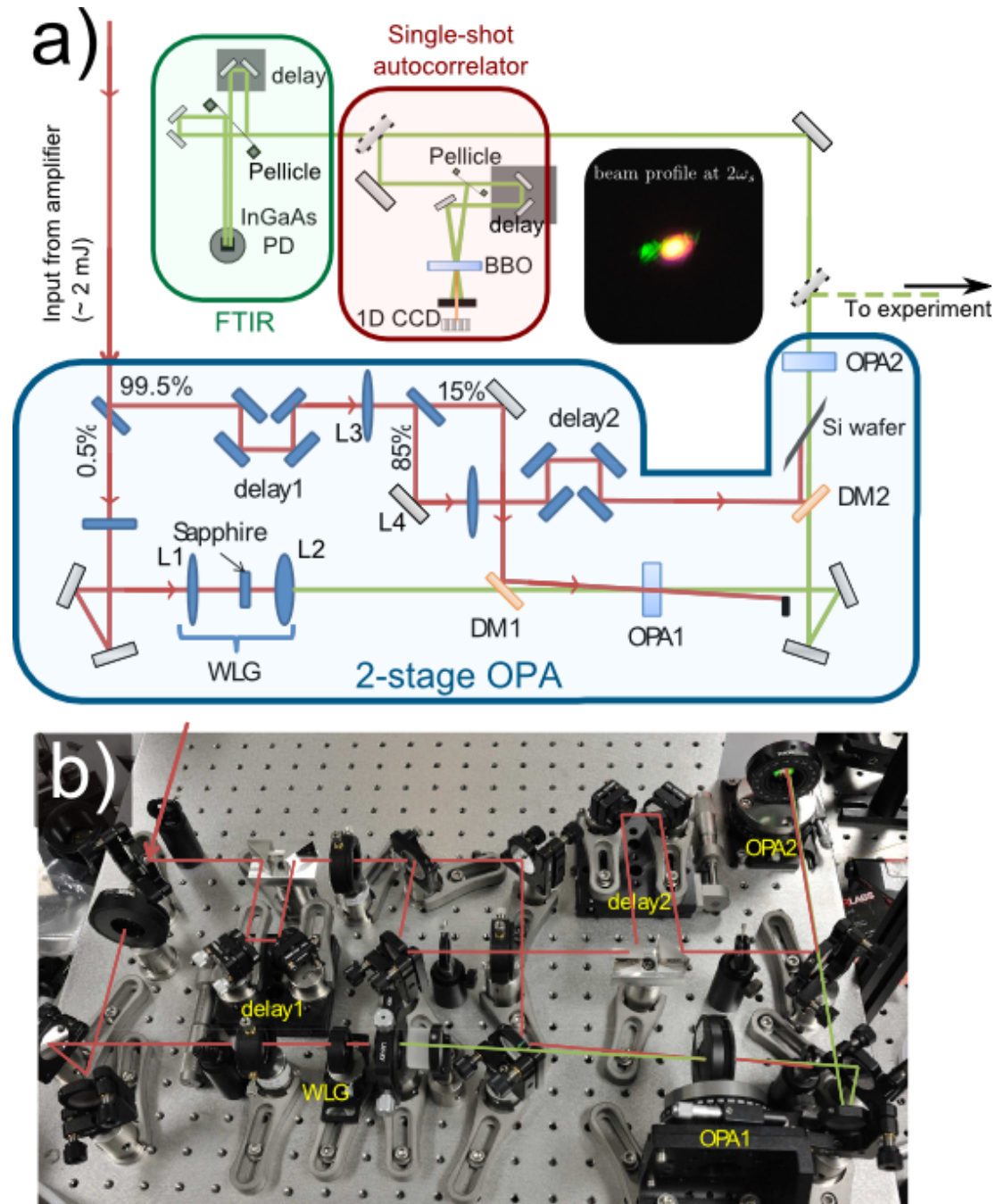


Figure 2.5: Schematic of optical parametric amplifier and beam diagnostics.

in Figure 2.5. Pulses from the Ti:sapphire regenerative amplifier (Sect. 2.2.4) at  $\sim 2$  mJ energy are split at the first dielectric mirror, reflecting over 99.5% of the power into the amplifier. Small portion of the transmitted light is focused into the 3 millimeter sapphire plate by means of an 5 cm focal length achromat lens ( $L1$ ). Relatively high peak intensity induces large and amplitude-stable self-phase modulation which results in generation of ultrabroadband white-light continuum ( $WLG$ ).  $WLG$  seed is needed to increase efficiency of the parametric amplification. The diverging white light is gradually refocused into the first amplification stage by a 3 cm focal length NIR achromat ( $L2$  with AR coating for 1200-1700nm, Thorlabs) through a dichroic mirror ( $DM1$ ,  $R \sim 95\%$  for p-pol 800nm,  $T > 90\%$  for 1200-1700nm, CVI). Uncoated BiBO crystal of  $5 \times 5$  mm<sup>2</sup> aperture cut for Type II phase matching ( $\theta = 42^\circ$ ,  $\phi = 0^\circ$  for  $o \rightarrow eo$  interaction [76]) from Newlight Photonics serves as the first stage of the amplifier ( $OPA1$ ). Portion of the pump beam ( $\sim 150$   $\mu$ J) is focused by 50 cm lens ( $L3$ ) into a  $OPA1$  and overlapped in time with the Stokes portion of the white light seed by means of the first delay stage ( $delay 1$ ) and the  $DM1$ . Type II interaction allows for slight noncollinearity without degradation to the phase-matching bandwidth [76]. A non-collinearity angle of 2 degrees at the  $OPA1$  between pump and  $WLG$  was exploited in our design. The non-collinear geometry allows to block used portion of the pump beam after the  $OPA1$ , and hence permits to avoid using another dichroic mirror for that purpose. This is an improvement over the existing designs [73] as it minimizes requirements for high bandwidth of the dielectric coatings as well as minimizes broadening of the amplified signal pulses. Half-wave plate is used to rotate polarization of either white-light generating beam or the pump beam to satisfy polarization requirement of the Type II interaction. Relatively narrow but constant bandwidth of the Type II interaction across most of the signal spectrum (1100 - 1600 nm) allows for flexible tunability via the first amplification stage [77, 76]. Amplified signal pulse and remaining  $\sim 85\%$  of the pump pulse are collinearly overlapped through a second dichroic mirror ( $DM2$ , identical to  $DM1$ ) in time in the second BiBO crystal ( $OPA2$ , Type I  $e \rightarrow oo$  :  $\theta = 11^\circ$ ,  $\phi = 0^\circ$  [76]).

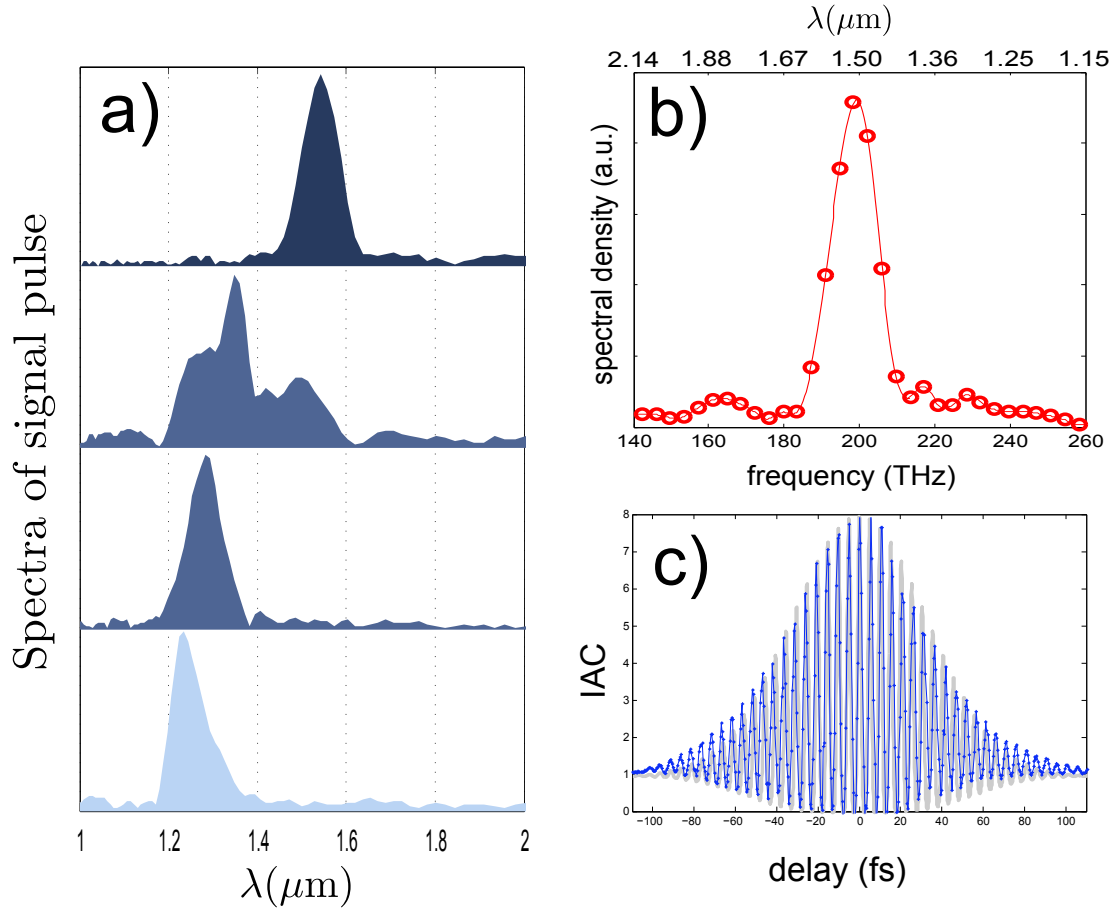


Figure 2.6: Characterization of the signal wave pulses from the OPA: (a) linear spectra of signal wave at some of the instances (defined by temporal overlap adjusted by *delay1* and *delay2* stages, as well angular tuning ( $\phi$ ) of the phase-matching condition by crystal tilting with respect to the k-vector of the incident beams); (b) Exemplary linear spectrum and (c) interferometric autocorrelation of the signal wave at one of the tuning positions. Qualitative fit (gray) to nearly transform limited Gaussian pulse IAC as well as FWHM yield  $\sim 60$  fs pulse duration.

Converging pump beam after the  $L3$  lens is re-collimated by means of a  $f=-20\text{cm}$  lens ( $L4$ ). Negative second lens is used to avoid focusing in air and hence generation of air-breakdown plasma which unavoidably leads to beam deterioration. The aperture of the OPA2 crystal ( $7\times 7\text{ mm}^2$ ) is designed to be below the damage threshold of the BiBO crystal, assuming maximum fill factor of the pump beam (achieved by

the aforementioned negative-lens telescope). Type I interaction in BiBO is nearly independent of the  $\theta$  angle and hence offers broadband parametric amplification bandwidth of the signal pulse generated in the *OPA1* stage [77, 76].

Type I interaction in the OPA2 allows to conveniently reject the residual pump beam from the output of an OPA by means of a 500  $\mu\text{m}$  crystalline Silicon wafer, placed at a Brewster angle for the MIR pulses. In this configuration, both signal and idler pulses are available from the output of the OPA, which was measured using a thermopile detector. A sum of signal and idler pulses yielded 0.3 mJ at 1.3  $\mu\text{m}$  when pumped by 2 mJ pulses, corresponding to 15% overall conversion efficiency. Combined signal and idler pulse energy of  $> 0.2$  mJ was maintained throughout the full tuning range of the amplifier, subject to the variation of the parametric gain of the OPA2 stage (Type I).

To characterize the output pulses of the OPA we have employed a Fourier transform interferometry (FTIR), comprised out of a Michelson interferometer with an uncoated 2  $\mu\text{m}$ -thick nitrocellulose membrane (pellicle) as a beam-splitter. While rejecting most of the incident energy ( $\sim 92\%$ ) usage of pellicle allows for dispersionless, ghost-free sampling of the input beams. Several detectors can be utilized to perform linear as well as nonlinear autocorrelation to extract either the linear spectra of the pulses or alternatively pulse width of the input beams. For instance, linear spectrum of the signal beam is provided by autocorrelation on an InGaAs photodetector, while two-photon absorption (2PA) of that beam in Silicon photodiode allows to measure its pulse width in performing interferometric intensity autocorrelation (IAC) [79]. Similarly, interferometric intensity autocorrelation of the idler pulses can be performed with the aid of the InGaAs photodetector when signal beam is blocked in transmission through a Germanium window (bandgap of  $\sim 0.67$  eV). Usage of typical mid-infrared to infrared detectors (for instance an uncooled lead selenide photodiode PbSe, bandgap  $\sim 0.27$  eV) allows for detection of the linear spectra of the idler wave as well as spectra of the possible difference frequency generated beam

between signal and idler waves (Sec.3, Chpt.6). Results showing tunability of the signal wave are presented in Fig. 2.6a. Tuning of the OPA is accomplished by optimization of phase-matching angles in both OPA1, OPA2 as well as temporal overlap of pump and signal pulses by means of two delay stages. Pulse characterization of the signal wave centered at a wavelength of 1500 nm is shown in Fig. 2.6. Interferometric autocorrelation is produced by slow scan of one of the delay arms of the Michelson interferometer and manually fitted with an IAC (grey) displaying some amount of second-order dispersion (Fig. 2.6). The pulse width of 50 fs is extracted from the fit for the assumed Gaussian pulse shape, corresponding to the time-bandwidth product of  $\sim 0.65$ . Our pulses are considerably shorter than in OPAs with similar geometry [73], mainly due to shorter pump pulses and less dispersive optics in the path of the signal wave. Current pulse width is largely limited by the relatively narrow phase-matching bandwidth of the type-II crystal. Reduction of amplification but shortening of the pulses has been observed in 2010 by Ghotbi *et. al.* in 2-stage OPA with both crystals in the Type-I configuration.

A single-shot autocorrelator allows for additional rapid verification of the pulse-width in a standard non-collinear geometry. Two pulses interact inside of the nonlinear crystal (here BBO or BiBO) to produce second harmonic at the overlap of the two pulses in time. Due to the tilt, time axis gets translated into the spatial coordinate. By measuring spatial distribution of the second harmonic and proper calibration of the spatial magnification it is possible to extract pulse duration without the need for a moving delay stage. Unlike detection via two-photon absorption, second harmonic generation is considerably weaker. Additional requirement of thin nonlinear crystal for broad phase-matching limits usage of single-shot autocorrelator only to intense pulses. Single shot pulse-width detection was used in this work only as a quick tool for to estimate pulse-width, typically yielding 20-40% larger pulse-width values than the IAC method, largely due to the use of a thick (200  $\mu m$ , tilted for MIR phase-matching) BBO crystal.

### 2.2.6 Toward higher energies

The success of optical parametric amplifiers in realizing high energy broadly tunable output pulses is still limited by the parasitic (third-order) nonlinearities, leading to self-phase modulation, self-focusing and damage of the nonlinear gain medium. The chirped pulse amplification techniques were realized to be applicable to the parametric processes in the first demonstration of optical parametric chirped-pulse amplification (OPCPA) by the early 1990's [80]. Modern day OPCPA's have been demonstrated to produce multi-teraWatt outputs with sub-10fs pulse duration [81]. The OPCPA has already been the enabling technology in the quest for high-harmonic generation with mid-infrared pulses. Research toward femtosecond OPCPA output in the petawatt regime is currently underway in Europe. Relativistic optics and particle physics are next on the horizon for the exciting field of high energy ultrafast science [20].

# Chapter 3

## Experimental techniques II: Terahertz spectroscopy

### 3.1 Historic overview

It is instructive to trace the historical developments of the discoveries associated with the infrared, mid- and far-infrared portions of the electromagnetic spectrum. It consists from an interweaving multitude of efforts: from the quest for highly sensitive detection methods to the development of the early quantum theory. In this review we are concerned with the technological progress to achieve frequencies lower than the visible portion of electromagnetic spectrum, i. e. infrared up to terahertz.

The first experimental investigation into the infrared part of the electromagnetic spectrum dates back to the year 1800 [82]. Wilhelm Herschel dispersed solar radiation and used a thermometer to measure the heat associated with the respective spectral components. He found that the thermometer reading peaks in the spectral region beyond the visible red light, as he concluded by moving the thermometer in the spectral plane of the prism [83]. Based on the distances that he reported, we estimate

that the detected peak corresponded to a wavelength of 1-2  $\mu\text{m}$ , most likely limited by the onset of the mid-infrared absorption of the dispersing glass prism. Herschel has attributed the detected peak to the invisible *heat* rays and believed them to be of the different origin than the visible light, despite his own confirmation of reflection and refraction laws [83, 84].

Interest in the solar emission continued to propel the investigation of the heat rays through the mid-1800s. In 1823 Seebeck discovered the thermoelectric effect by noticing a compass needle deflection when he applied a temperature gradient across a junction of two dissimilar metals. The discovery of the thermo-electric effect made it possible for the sensitive temperature measurements in devices analogous to the modern day thermocouple probes.

In light of and contemporary with the Maxwell's discovery of the governing laws of electromagnetism, new understanding of the solar radiation began to emerge. Driven by the advancements in experimental techniques, researchers had begun to take notice of the dependence of the strength of the infrared emission on the temperature of the emitter and to identify absorption lines as due to the atmosphere in the path of the heat rays. A need for a sensitive temperature probe was greater than ever, and in 1881 Samuel P. Langley invented the first *bolometer*<sup>†</sup>.

A bolometer is a highly sensitive probe of a thermal resistance of a metal, and in Langley's interpretation consisted of two black-coated platinum plates, one of which was placed in front of the radiation while the other was shielded. Sensitive electronics allowed him to measure the temperature-induced change of the differential resistance<sup>‡</sup> between the two platinum plates of the bolometer [84]. In combination with a galvanometer capable of measuring 100 pico-Ampere currents, Langley esti-

---

<sup>†</sup>etymology stemming from the Greek **bole** - *beam of light, stroke* and English **o-meter** [85]

<sup>‡</sup>Langley used a Wheatstone resistor bridge, which falls in a class of differential measurement techniques. Such techniques are highly sensitive in that they allow to measure small changes on top of the large background by subtracting the latter.



mated the resolution of his bolometer to be  $\Delta T \sim 10\mu\text{K}$  [86], proclaiming that he is capable of detecting heat radiated by a cow at a distance of over half a mile [87].

Using his bolometer at the height of  $\sim 3600$  meters above sea level (Mt. Whitney, CA, USA)<sup>†</sup>, Langley was able to precisely characterize the solar spectrum up to the wavelength of  $5.3\ \mu\text{m}$  [86]. More importantly, Langley's accurate measurements of the absorption lines in the solar spectrum (infrared Fraunhofer lines) paved a way to the revolution in atomic absorption spectroscopy. With an aid of a bolometer, infrared absorption series of hydrogen atom was discovered (for quantum number  $n=3$ , Paschen 1908). Together with the Balmer series in the visible, these progressions were captured by the general Rydberg formula and served as an early experimental proof of the validity of the quantum mechanical theory of Bohr.

Disadvantages of the bolometer included its long-term drift and high sensitivity to ambient perturbations. Experimentalists were looking for ways to improve the instrument. In a time span of 1890s-1900s Heinrich Rubens together with Ernest Fox Nichols extended the infrared measurements beyond the wavelength of  $50\ \mu\text{m}$ , corresponding to frequencies below 6 THz [87]. A combination of improvements to the thermopile detectors<sup>‡</sup> and black-body radiation sources allowed them to perfect the art of the bolometric measurement technique.

Rubens and Nichols discovered that a quartz crystal exhibits a strong and sharp reflectivity for incidence wavelengths around  $\sim 9\mu\text{m}$  [88]. They realized that after multiple of such reflections, they could achieve high monochromaticity of the residual infrared beam. The term *residual rays* (German: *Reststrahlen band*), first coined by them is still being used today. Unknowingly, they discovered one of the manifestations of the polariton modes of a solid, in that the electromagnetic wave can not be supported between longitudinal optical (LO) and transverse optical (TO) phonon fre-

---

<sup>†</sup>to minimize strong atmospheric absorption

<sup>‡</sup>Thermopile detector is based on a differential detection of temperature change between two thermocouples. Nichols and Rubens used dissimilar metals of Bismuth and Antimony.

quencies. By characterizing a collection of crystals [89], Rubens and Nichols came up with an impressive catalog of the monochromatic infrared *restrahlen* sources [90, 91].

In parallel with experiments, theoretical investigations concentrated on understanding the radiation spectrum of a blackbody. While the main problem was the divergence in the ultraviolet region (UV catastrophe), the existing models needed good data in the far-infrared to correctly fit the Boltzmann tail of the spectral distribution of a black body. In 1900 Rubens was able to provide Max Planck with the accurate far-infrared data of the blackbody spectrum. By analyzing most precise UV and IR data of the time, Planck came to realization of his famous distribution law, laying the foundation of the quantum theory [87].

In the span of 1900-1960, nearly 2000 research papers have been published on the subject of the far-infrared<sup>†</sup> radiation [87]. Few notable advances in the THz detection that still bear relevance to modern day devices included the invention of a sensitive pneumatic detection cell by Marcel Golay (1947)[92]. Semiconductor bolometers based on InSb (Putley, *et. al.* 1960, [93]) and Ge (Low *et. al.* 1961, [94]) were demonstrated at liquid-helium temperatures, becoming the predecessors for the modern day Si bolometer (Sec. 3.3.1).

In parallel with the advances in THz detection technologies, development of sources was sparse. Some highlights include strong<sup>†</sup> THz radiation from metal filings under electric discharge (Arkadiewa, 1924, [95]) as well as sub-THz and THz frequency generation by microwave techniques such as traveling wave tubes (e.g. backward wave oscillators [87]) and frequency harmonic generators [96].

Real breakthroughs in THz source development came with the invention of the laser. In 1960-70, far infrared and THz lasers based on rotational and vibrational transitions in various gases and liquid vapors were developed [97]. For instance, the

---

<sup>†</sup>referred to by contemporaries as “sub-millimeter”

<sup>†</sup>comparable to incandescent sources of the time.

rotational transitions in methanol can be inverted at various frequencies from 0.4-4 THz [98]. Economic and rugged methanol lasers are still being used today as CW THz sources, reaching 50 mW output with 0.4% optical efficiency when pumped with CO<sub>2</sub> [99]. Modern developments in CW and long-pulse THz sources include approaches such as quantum cascade lasers [100, 101], optical rectification [102] and linear photo-mixing [103]. However, major progress in the technology of pulsed THz sources and detectors occurred in parallel with the developments of the ultrafast science. Some details of this progress are described in the remaining sections of this chapter.

In 1880s, Heinrich Hertz demonstrated generation and detection of electromagnetic waves at radio frequencies by using a biased electric dipole<sup>†</sup>, sized much smaller than the wavelength of radiation [104]. Similarly, Auston *et. al.* in 1984 used a femtosecond pulse to produce (and detect) a burst of terahertz radiation by effectively shorting a biased metallic dipole deposited onto a photoconductor [105] – so called, photo-conductive (PC) switch. Grischkowsky *et. al.* modified the geometry of the PC switch and utilized a hyper-spherical sapphire lens to couple THz radiation into the free space [106]. This launched the field of ultrafast THz optoelectronics.

## 3.2 Methods of THz pulse generation

One of the consequences of charge acceleration is the emission of the electromagnetic radiation [107]. It can be shown that the radiated field  $E_{rad}(t)$  of a Hertzian dipole<sup>‡</sup> a distance  $r$  away, is well approximated by (Appx. D, Eq. D.19):

$$\mathbf{E}_{rad}(t) = \frac{k^2}{4\pi\epsilon_0} \frac{e^{ikr}}{r} \sin\theta \frac{d^2p(t_r)}{dt^2} \hat{\boldsymbol{\theta}} \quad (3.1)$$

---

<sup>†</sup>now known as a *Hertzian dipole*

<sup>‡</sup>two point charges separated a distance  $x$  and connected by a thin superconducting wire, such that  $x \ll \lambda$

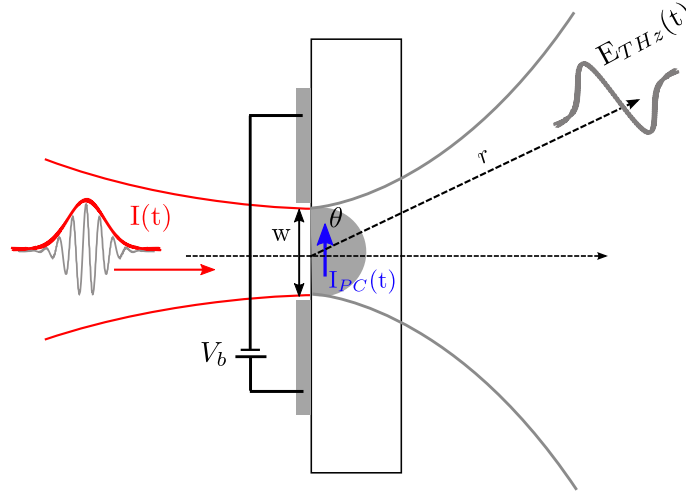


Figure 3.1: Schematic of a photoconducting switch. An optical pulse with intensity profile  $I(t)$  is incident onto a biased metallic gap of width  $w$ , deposited onto a semiconducting substrate. The generated photocurrent  $I_{PC}(t)$  radiates terahertz pulse  $E_{THz}(t)$  with an angular distribution of a Hertzian dipole (Eq. 3.1).

where  $p(t) = ex(t)$  is the dipole moment and  $t_r = t - r/c$  is the retarded time, assuring causality of the radiated field [107]. The radiated field is polarized along the unit vector  $\hat{\theta}$ , where  $\theta$  is the angle between the direction of the observation and the axis of the dipole (Fig. 3.1). As a consequence of such polarization, the radiated field cancels out at the points on the dipole axis (as is manifested by the  $\sin(\theta)$  dependence). The expression 3.1 is an approximation which is valid only in the *far-field*, i.e. when both the size of the dipole and its wavelength are much smaller than  $r$ .

### 3.2.1 Photoconducting switch

Consider a photoconducting switch as depicted in Fig. 3.1. An optical pulse with a temporal intensity profile  $I(t)$  is incident onto a semiconducting gap region of width

$w$  under a DC bias voltage  $V_b$ . The generated photocurrent  $I_{PC}(t)$  is given by:

$$I_{PC}(t) = \frac{1}{w} \frac{dp(t)}{dt}, \quad (3.2)$$

with an implicit assumption of a one dimensional charge distribution. Applying Eq. 3.1, the radiated field of a PC switch is proportional to:

$$E_{rad}(t) \propto \frac{dI_{PC}(t)}{dt}. \quad (3.3)$$

To calculate the radiated electric field, we have to consider the recombination and drift of the photocarriers, in response to the optical excitation. First, the photocurrent density is given by:

$$J(t) = N(t)ev(t) \quad (3.4)$$

where  $N(t)$ ,  $e$  and  $v(t)$  are the number per unit volume, charge and drift velocity of the photogenerated charge carriers. In general, both  $v(t)$  and  $N(t)$  quantities are time dependent.

The charge density is described by the rate equation:

$$\frac{dN}{dt} = \frac{\alpha I(t)}{h\nu} - \frac{N}{\tau_r}, \quad (3.5)$$

where  $\alpha$  is a linear absorption coefficient of the pulse at frequency  $\nu$  and  $\tau_r$  is the recombination time. The response function  $G_r(t)$  of the carriers to a delta-function excitation  $\delta(t)$  is:

$$G_r(t) = N_0\theta(t)e^{-t/\tau_r}, \quad (3.6)$$

where  $N_0 = \alpha I_0/h\nu$  and  $\theta(t)$  is a Heaviside step function.

The time dependence of the drift velocity of the photocarriers is well-described by a Drude model [108, 109]:

$$\frac{dv(t)}{dt} + \frac{v}{\tau_e} = -\frac{eE(t)}{m^*} \quad (3.7)$$

where  $\tau_e$  is the momentum relaxation time (due to inelastic scattering processes) and  $m^*$  is an effective mass of the charges [110]. The response function to a dispersive excitation is given by:

$$G_e(t) = \theta(t)\mu_e E_b (1 - e^{-t/\tau_e}), \quad (3.8)$$

where  $\mu_e = e\tau_e/m^*$  is the electronic mobility and  $E_b = V_b/w$  is the bias DC electric field. The total current due to photogenerated electrons is determined by a convolution of the input pulse  $I(t)$  with the determined response functions (Eq. 3.6 and Eq. 3.8):

$$I_{PC}(t) = \int_{-\infty}^{\infty} I(t-t')G_r(t')G_e(t')dt'. \quad (3.9)$$

This result is fairly general within the framework of the Drude theory. We do want to point out that it excludes the effect of photogenerated holes as they have much lower mobility and thus contribute negligibly to the current. By treating the problem in one dimension only, we have also ignored any inhomogeneities of the photocurrent distribution and the bias field (e.g. spatial beam profile, absorption depth, diffusion). Physical processes that fall outside of the Drude framework, such as high-density effects (e.g. screening or band-filling) are also not included in the analysis [111]. These omissions render results relevant for the cases when the generated photocarrier density is of the order of  $\sim 10^{17} \text{ cm}^{-3}$  or lower.

For an assumed case of the Gaussian-shaped optical pulse envelope  $I(t)$ , Equation 3.9 can be solved exactly in terms of the error functions [109]. The reader is referred to an article by Duvillaret *et. al.* for more details [113]. In the interest of clarity, we limit our discussion to a presentation of a numerical modeling of the transient photocurrent (Eq. 3.9) and resulting radiated field (Eq. 3.3) for a Gaussian-shaped input pulse  $I(t) = I_0 \exp(-t^2/\tau_p^2)$  (Fig. 3.2). Normalized  $I_{PC}(t)$  and the corresponding  $E_{rad}(t)$  are first calculated for the case of an infinite response, when  $\tau_e = \tau_r \rightarrow 0$  (Fig. 3.2(a,b)). The cases of finite response time of the photocurrent are shown in Fig. 3.2(c,d) for  $\tau_r = 2\tau_p$  and Fig. 3.2(e,f) for  $\tau_r = 4\tau_p$ , while keeping  $\tau_e = 0.1\tau_p$

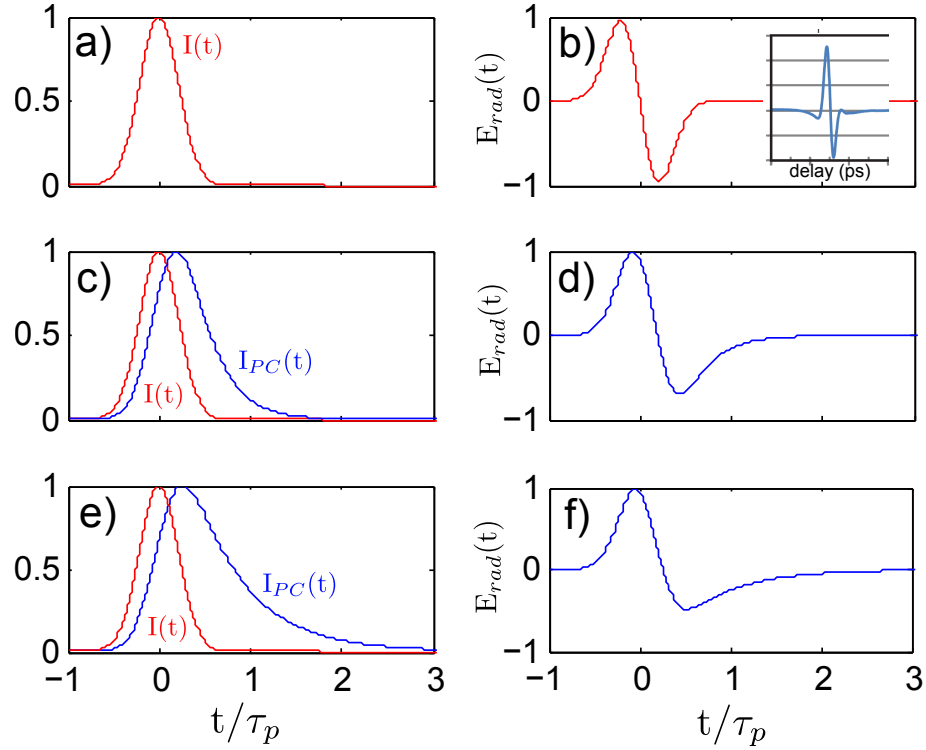


Figure 3.2: Temporal response of a photoconductive switch. (a) and (b) show  $I(t)$  and  $E_{rad}(t)$  for the initial pulse (effectively  $\tau_r = \tau_e = 0$ ); in (c) and (e) photocurrent  $I_{PC}(t)$  (blue) is shown for the cases of  $\tau_r/\tau_p = 2$  and  $\tau_r/\tau_p = 4$  respectively, while (d) and (f) display the computed radiation field  $E_{rad}(t)$  (in (c-f)  $\tau_e$  is kept the same at  $0.1\tau_p$ ). Inset in pane (b):  $E_{rad}$  from a typical commercially available PC switch [112].

the same. It is evident that the current is broadened in time by the rise ( $\tau_e$ ) and fall ( $\tau_r$ ) times of the response. The leading edge of the radiated field remains nearly unchanged (due to fixed  $\tau_e$ ), while the falling edge is drastically broadened due to the increase in the carrier recombination lifetime  $\tau_r$ . For the given semiconductor, the important design parameter of the antenna is to shorten the carrier recombination lifetime  $\tau_r$ . Radiation damaged silicon or low-temperature grown GaAs have been demonstrated with recombination times of around 100 fs [108]. This limits current performance of a typical PC switch to the frequencies below 10 THz.

### 3.2.2 Optical rectification

In general, an electric field  $E(t) = E_0 \cos(\omega t)$  induces a polarization  $P(t)$  inside of a dielectric which can be represented in a perturbative regime by Taylor series:

$$P(t) = \sum_{m=1}^M \chi^{(m)} E^m(t), \quad (3.10)$$

where  $\chi^{(m)}$  is an electric susceptibility of an integer order  $m$  and  $M$  represents a practical upper bound for the expansion. By direct multiplication in the time domain we have implicitly assumed an instantaneous response, which is a good approximation when the frequency of the field  $\omega$  is below material resonances. The term  $m = 1$  represents the usual linear response theory.

In this discussion we are interested in the nonlinearity associated with  $\chi^{(2)}$ . For the case of a monochromatic input, the second order polarization  $P^{(2)}$  becomes [63]:

$$P^{(2)}(t) = \chi^{(2)} E^2(t) = \chi^{(2)} E_0 \frac{1 + \cos(2\omega t)}{2}. \quad (3.11)$$

The nonlinearity leads to a second harmonic generation (SHG,  $2\omega$ ) of the fundamental frequency  $\omega$  as well as a DC electric field  $E_0/2$ . The second harmonic and the DC field are the degenerate cases of a sum and a difference frequency generation respectively. For the assumed case of the monochromatic input beam (Eq. 3.11), the manifestation of the DC field is a potential difference generated across the dielectric [114]. In other words, an oscillatory field has been *rectified* in order to produce a DC field. The reverse process of *optical rectification* (OR) has to be physical as well. A voltage, applied across a material possessing  $\chi^{(2)}$  response, will lead to a change of the refractive index of that material. The total polarization (up to the second order) can be written as

$$P(t) = [\chi^{(1)} + \chi^{(2)} E_{DC}] E_0 \cos(\omega t), \quad (3.12)$$



where the bracketed quantity corresponds to an effective linear susceptibility  $\chi_{eff}^{(1)}$ . The induced change of the refractive index is:

$$\Delta n \simeq \frac{1}{2} \chi^{(2)} E_{DC}. \quad (3.13)$$

The Eq. 3.13 is describing linear *electro-optic* effect or *Pockels* effect. By measuring the small change of the refractive index, a field-resolved detection of the THz radiation can be implemented. This detection technique is known as *electro-optic sampling* and its implementation is discussed in detail below (Sec. 3.3.2).

The commonly used electro-optic crystal for generation (and detection) of the optical rectification (THz) is zinc telluride (ZnTe). It is an intrinsic II-VI semiconductor with cubic crystal structure and an energy gap of  $\sim 2.24$  eV. It possess large nonlinear coefficient  $d_{eff}$  in addition to having favorable phase-matching conditions, considered below.

In general, phase-matching condition can be obtained by solving for the electromagnetic field, radiated by the oscillating polarization. This condition is given by (Appx. C):

$$\Delta k = \frac{\omega}{c} |n_{THz} \cos(\theta) - n_g| \quad (3.14)$$

where  $n_g$  is a group index at the optical frequencies and  $n_{THz}$  is the refractive index at the center frequency  $\omega$  of the THz pulse. Angle  $\theta$  is defined in Fig. C.1. For most electro-optic crystals  $n_{THz} > n_g$ , due to an additional refractive index contribution from the phonon modes at the THz frequencies (Appx. E). Since the THz wave propagates slower than the optical pulse, its phase front constitutes a cone, with an apex following the generating pulse. The angle of this cone is defined by the  $\Delta k = 0$  condition in Eq. 3.14. The boundary of the cone corresponds to the leading edge of the shock-wave – an analogous situation to Cherenkov radiation. Auston was first to predict [115] and measure [116] Cherenkov radiation at THz frequencies in a lithium niobate (LiNbO<sub>3</sub>) – an electro-optic crystal with a large nonlinear coefficient. Recently, Nelson’s group has demonstrated propagation of the optical pulse in

phase with the THz shock wave in LiNbO<sub>3</sub>. This was achieved by means of a prism geometry and pulse front tilting of the optical beam, resulting in generation of high field THz pulses [117].

Ideally, one desires  $\Delta k$  (Eq. 3.14) to be equal to zero for  $\theta \sim 0$ . This can be accomplished in the ZnTe crystal. Efficiency of the phase-matching is described by a *sinc* function ( $\text{sinc}(x) = \sin(x)/x$ , see Eq. C.4), so that:

$$E_{THz} \propto L \text{sinc}(\Delta k L / 2). \quad (3.15)$$

where  $\Delta k$  is given by Eq. 3.14 for  $\theta = 0$ . For a finite  $\Delta k$ , the two pulses would go out of phase after propagating a certain distance (called *coherence length*), corresponding to the first zero of the *sinc* function. After further propagation, some of the THz wave would convert back into the optical wave ( $\text{sinc} < 0$ ) until the next phase flip is encountered. It is clear that the crystal length  $L$  has to match the coherence length for the most efficient generation of the THz.

In Figure 3.3a we plot the optical group index  $n_g$  and the THz index  $n_{THz}$  for ZnTe, calculated from the following equations [118]:

$$n_o^2(\lambda) = 4.27 + \frac{3.01\lambda^2}{\lambda^2 - 0.142} \quad (3.16)$$

$$n_{THz}^2(\nu_{THz}) = \frac{289.27 - 6\nu_{THz}^2}{29.16 - \nu_{THz}^2} \quad (3.17)$$

where  $\lambda$  is in  $\mu\text{m}$ ,  $\nu_{THz}$  in THz and  $n_g = n_0 - \lambda dn_0/d\lambda$ . Perfect phase-matching between the THz wave at  $\sim 2.5$  THz and the optical excitation at  $\sim 775$  nm is evident from the figure. To estimate the bandwidth of the phase-matching, we calculate normalized efficiencies (Eq. 3.15) for several crystals with varying thickness  $L$  (Fig. 3.3)b, all when pumped by 800 nm at the peak gain of the regenerative amplifier (Chpt. 2.2.4). The trade-off in the choice of the crystal thickness is obvious: the desired flat efficiency spectrum of the thin crystal ( $L = 100\mu\text{m}$ ) is compromised

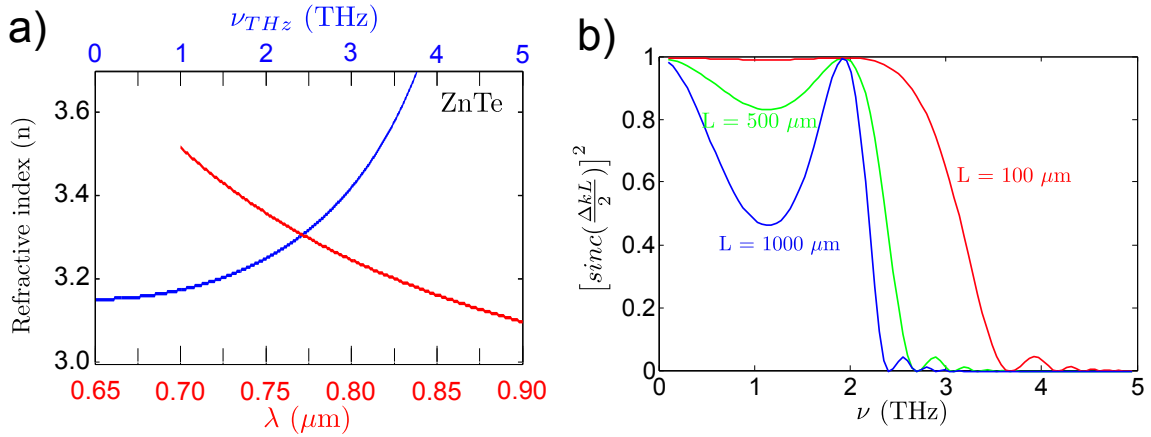


Figure 3.3: Phase-matching in ZnTe crystal. (a) Refractive index at THz frequencies (blue) and optical frequencies (red) in ZnTe [118]; (b) Spectra of phase-matching efficiency for various thicknesses  $L$  of the crystal (Eq. 3.15).

by a factor of 10 reduction in the radiated THz field (Eq. 3.15) in contrast to a more structured efficiency of the stronger emitter ( $L = 1000\mu\text{m}$ ). In all of the cases however, the phase-matching bandwidth is limited to frequencies below 3 THz. This limitation is due to the onset of the strong dispersion in the  $n_{THz}$  (Fig. 3.3a) for frequencies higher than 3 THz, which results from the proximity of the TO-phonon resonance at 5.3 THz.

Typical radiation signals from  $\langle 110 \rangle$  ZnTe crystal, when pumped by  $\sim 35$  femtosecond pulses from the regenerative amplifier (Chpt. 2.2.4), are shown in Fig. 3.4. Left panel (Fig. 3.4a) depicts radiated THz fields from the ZnTe crystals with  $L = 500\mu\text{m}$  and  $L = 1000\mu\text{m}$ . The corresponding magnitude of the field spectra is shown in Fig. 3.4b. The THz field is detected via the electro-optic sampling in a  $500\mu\text{m}$  ZnTe crystal by varying the delay  $\tau$  (see Sec. 3.3.2 for the description of the experimental setup). The measured ratio of the THz field strengths at  $\tau = 0$  is  $E_{1000}/E_{500} = 1.98 \pm 0.02$ , in excellent agreement with the  $E_{THz} \propto L$  scaling, as per Equation 3.15. Figure 3.4b shows that the OR spectrum for the case of the thinner crystal is broader, consistent with the calculation 3.3. The observed spec-

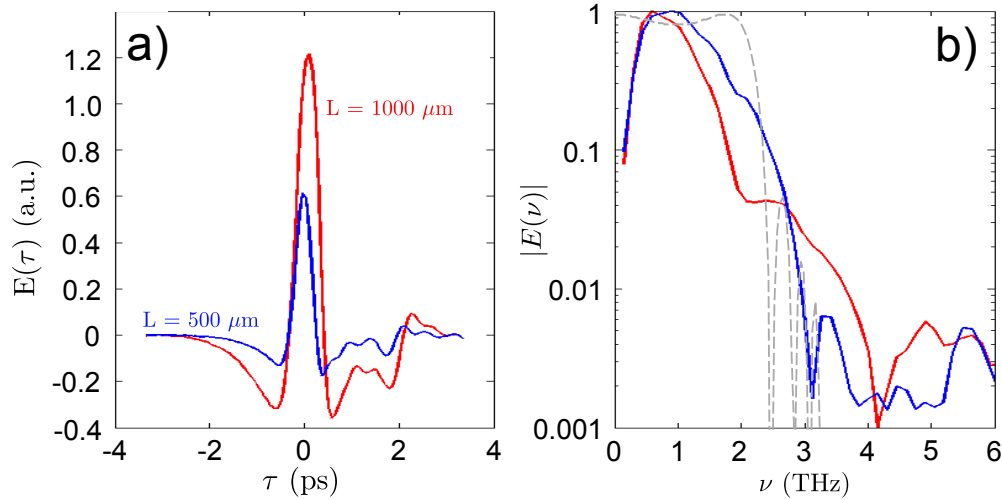


Figure 3.4: Optical rectification in  $\langle 110 \rangle$  ZnTe. (a) Radiated field  $E(\tau)$  from optical rectification in two ZnTe emitters of thickness 0.5mm and 1mm, as detected via electro-optic sampling in 0.5mm ZnTe; (b) Corresponding magnitude of the field spectra  $|E(\nu)|$  on a semi-log scale. Calculated phase-matching efficiency in 0.5mm ZnTe between THz and 800nm pump is shown as the dashed line.

tral drop-off around 2.5 THz is due to the phase-matching bandwidth limitation of the detection emitter/detector system, consistent with the phase-matching calculation for 500  $\mu\text{m}$  thick crystal (dotted gray line). Common spectral dips to both traces (e.g.  $\sim 1.75\text{THz}$ ) are due to the atmospheric water vapor absorption lines [119] (Fig. 3.6). This absorption is also visible in the time domain, corresponding to long-lived oscillations following the trailing edge of the THz pulse (Fig. 3.3a).

Another interesting aspect of the THz waveform is its shape. There is a qualitative difference in the waveforms, emitted by OR (Fig. 3.4a) and PC antenna (Fig. 3.2b(inset)). The radiation from antenna is predicted to have a characteristic “s”-shape in the time domain, a consequence of  $E_{rad}^{PC}(t) \propto dI(t)/dt$  (Eq. 3.3). In the case of OR, the waveform of the THz exhibits “w”-shape, consistent with a second time-derivative of the pulse envelope:  $E_{rad}^{OR}(t) \propto d^2I(t)/dt^2$  (Eq. 3.11 with Eq. D.20). A physical origin of this difference lies in the nature of the excitation itself. The case

of the PC antenna is described by the response of the photocarriers to an externally applied field (DC bias), resulting in the establishment of a new quasi-equilibrium for the carriers. The rise time of the photocurrent transient to approach the new equilibrium is an integral in the time domain (convolution), effectively removing time derivative in the radiated field. In using Taylor series expansion for the nonlinear polarization we have implicitly assumed bound nonlinearity, meaning that no displacement of the carriers following the excitation takes place (Eq. 3.10). In short, displacive excitation mechanism is responsible for the “s”-shape, while “w”-shape is a characteristic of an impulsive response. As will become evident from Chpt. 4, most cases of radiation from collective modes in a solid result from displacive excitation, as due to a longitudinal nature of these modes.

It should also be pointed out that THz generation via optical rectification has been also accomplished in a number of other electro-optic crystals, including GaP [120], GaAs [121, 122], GaSe [123], InP [121, 120], CdTe [121]. Organic crystal DAST has also been shown as an efficient broadband THz emitter due to its particularly large nonlinear coefficient [124]. Current state-of-the art ultrabroadband generation and coherent detection of single-cycle pulses utilizing electro-optic effect spans a range of (0 - 150) THz [125, 10], with peak field strengths exceeding 100 MV/cm [126].

THz generation has also been observed from surface nonlinearities [127]. Collective modes in solids, such as plasmons [128] and phonons [129] can also emit THz (for e.g. Fig. 3.6) and are the subject of the remaining chapters (Chpts. 4,5).

### 3.3 Methods of THz detection

There are two classes of THz detection methods, broadly classified into incoherent and coherent detection schemes.

- Incoherent detection method utilizes a slow detector (e.g. bolometer) for detection of the time-averaged intensity of the THz source, the so called *square-law detector*. Typical time response ranges from  $10^{-6} - 10^{-3}$  seconds, depending on the type of detection. Square-law detection relies on registering of the interference of signal produced from the two replicas of the unknown radiation source, and hence allows determination of the linear spectral content of the source (Sec. 3.3.1).
- Coherent detection implies detection of the electric field of the THz pulse and utilizes either fast electronic transport in semiconductors (PC antenna) or Pockels effect (Sec. 3.3.2). Ultrafast detection is possible by sampling the detected signal with a femtosecond probe pulse, in which case the time resolution is limited by the duration of the probe pulse.

### 3.3.1 Incoherent detection of THz: bolometer

Historically, detection of THz radiation was possible with the invention of the bolometer. Bolometers cooled to liquid helium-4 ( $^4\text{He}$ ) temperatures (4.2 - 2.17 K) still find applications in detecting THz in both optical labs and astronomical observatories [130]. In this section we discuss the use of bolometer to detect THz radiation.

Bolometer is a thermal detector, and hence the detector response time  $\tau_d \gg 1/\nu_{\text{THz}}$ . Therefore, one can use the bolometer for detection of time average power of the emitted THz. It is possible to determine spectral content of the high frequency source (THz) by autocorrelating it on a slow detector using a Michelson interferometer. Time domain trace is generated by using a stepper-motor driven translation stage in the moving arm of a Michelson interferometer. Fourier transform of the time-domain linear interferogram reveals spectrum of the source, subject to the spectral detection bandwidth of the detector. Ideal thermal detector acts as a blackbody, however practical limitations of the spectral bandwidth are imposed by

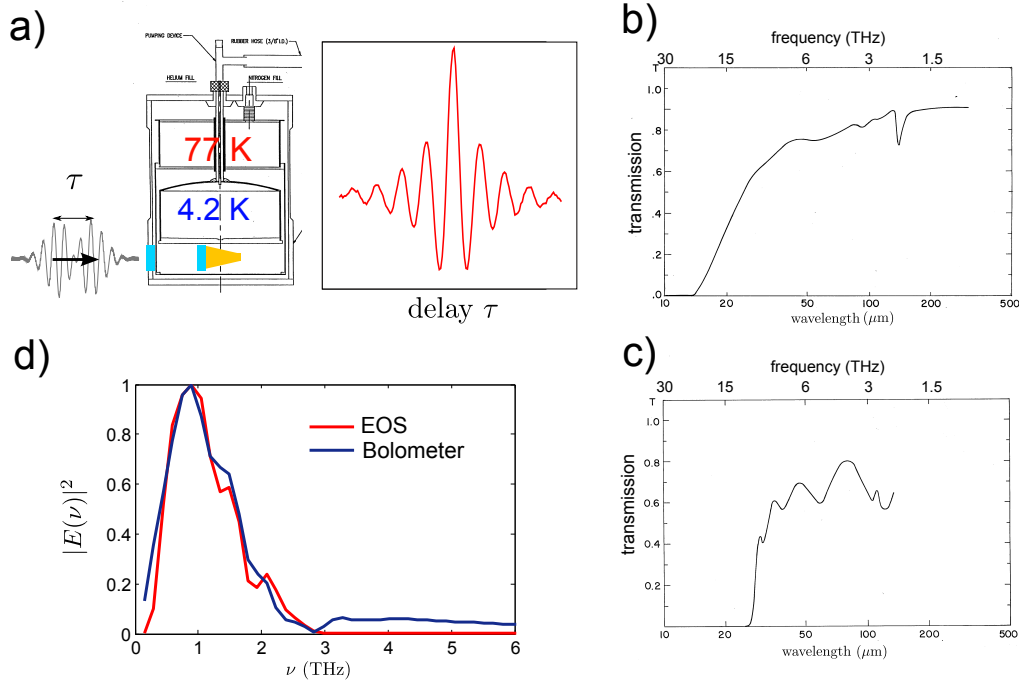


Figure 3.5: Detection of THz radiation using bolometer. (a) top: schematic of the bolometer with nitrogen and helium reservoirs; bottom: characteristic linear autocorrelation of THz emission from plasmon mode in InSb at 77 K (Chpt. 4); Transmission spectra of white polyethylene window ( $T=300\text{K}$ , b) and Winston cone filter ( $T=4.2\text{K}$ , c), consisting of a wedged sapphire with ZnO layer on one side and thin diamond scatter layer on the other; (d) Spectra of the emission from surface plasmon modes of InAs nanowires (Chpt. 4) as detected with EOS and bolometer. Note the 3 THz cut-off for the case of EOS (ZnTe,  $L=500\ \mu\text{m}$ ), due to the velocity mismatch of THz and NIR above 3 THz.

the necessity of the windows, described below. The bolometer used in this work is based on measurement of the temperature-dependent thermal resistance in silicon. In the particular implementation (Infrared Laboratories), silicon is thermally bonded to blackened diamond absorber and mounted at the apex of an off-axis gold-coated paraboloid (Winston cone) for efficient collection of the incoming radiation [131]. Bolometer is designed to be filled with liquid helium ( $^4\text{He}$ ) at 4.2 K <sup>†</sup> to ensure low thermal noise in the detector. Liquid helium reservoir in thermal contact with

<sup>†</sup>all temperatures of liquids are specified at standard atmospheric pressure.

an outer reservoir filled with liquid nitrogen ( $N_2$ ) at 77 K (Fig. 3.5a). Outer wall of the bolometer is thermally isolated from the environment by means of a vacuum jacket. Liquid nitrogen vessel is used to reduce conductive and radiative loads on the helium reservoir, important due to low latent heat of vaporization of the latter. Detector assembly (silicon + Winston cone) are at the bottom plate of the liquid helium reservoir, where a window in a wall of the bolometer provides optical access to the detector. There are two windows that affect spectral performance of the bolometer. First window (Fig. 3.5b) ensures vacuum seal between the detection bay of the bolometer and the ambient, in addition to blocking VIS-IR band of the incoming radiation. Second filter (Fig. 3.5c) further suppresses the VIS-IR background and diffuses the incoming radiation to suppress modal interference of the Winston cone waveguide. Combined average transmission of both windows is 0.3-0.5 and features nearly flat response in the range of 1 - 12 THz. In Figure 3.5d we have compared coherent (EOS) and incoherent (bolometer) detection for frequencies bounded to  $< 3$  THz ( $L_{ZnTe} = 500 \mu\text{m}$ ) by the velocity matching conditions in the ZnTe detection crystal and found very good agreement between the two measurement techniques.

Characteristic autocorrelation from THz radiation emitted by low-frequency, low-temperature plasmon mode (Chpt. 4), excited in indium antimonide (InSb) is shown in Fig. 3.5. As an example of broadband response of the bolometer, Fig. 3.6 shows emission from plasmon and phonon modes in indium arsenide (InAs). In passing we note that the analysis of the low-frequency part of the InAs emitted spectrum reveals spectral dips, attributed to the water (vapor) absorption lines in the atmosphere [119, 132]. Purging of the THz beam line with dry nitrogen has been verified to dramatically reduce this effect.

An obvious advantage of the bolometric detection is a nearly flat spectral response. This fact is particularly useful for frequencies above 3 THz [133], where real and imaginary parts of linear and nonlinear response make interpretation of coherently detected signals very problematic [134, 135]. Disadvantages of using a



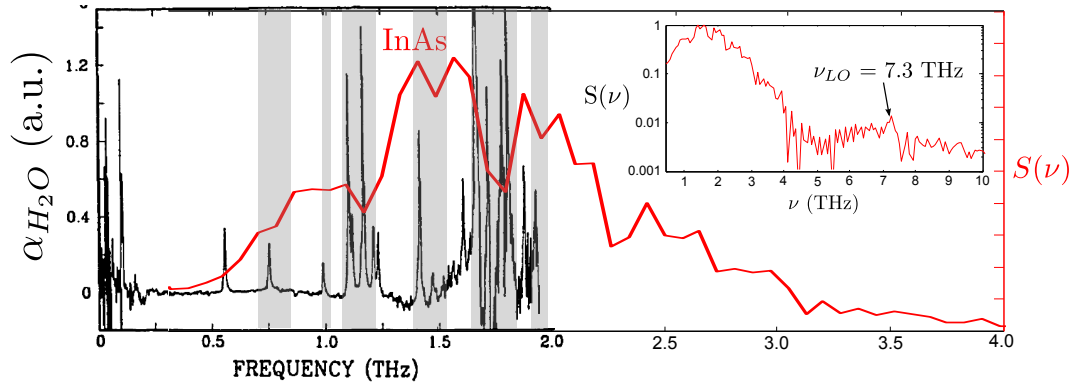


Figure 3.6: Spectrum  $S(\nu)$  of THz emission from bulk InAs semiconductor (red), superimposed with water vapor absorption spectrum (black) (Fig3b of Ref.[119]). Gray vertical bars highlight regions where decrease in InAs emission is in correspondence with the water absorption lines. Inset: THz spectrum of InAs on a semi-log scale with the frequency axis extending to 10 THz. Emission from plasmon ( $\sim 2$  THz) and  $LO$  phonon (7.3 THz) modes is resolved (Chpt. 4).

bolometer for THz detection include the fact of incoherent detection, microphonic noise due to the boiling liquids and recently publicized world-wide shortage of natural helium gas.

### 3.3.2 Coherent detection: EOS

By the virtue of reciprocity, any radiation mechanism can be used for detection. This was first demonstrated by Hertz who used two identical dipoles to emit and detect electromagnetic radiation. Methods of THz generation, discussed in Sec. 3.2 are all applicable for THz detection. For instance, in a case of detection with a photoconductive emitter, the role of a bias field is replaced with the THz transient (Fig. 3.1). An optical gating pulse generates photocarriers in the gap region of the antenna and carriers respond under the presence of the bias THz field. Generated current is directly proportional to field of the THz pulse and hence making possible to coherently detect the latter.

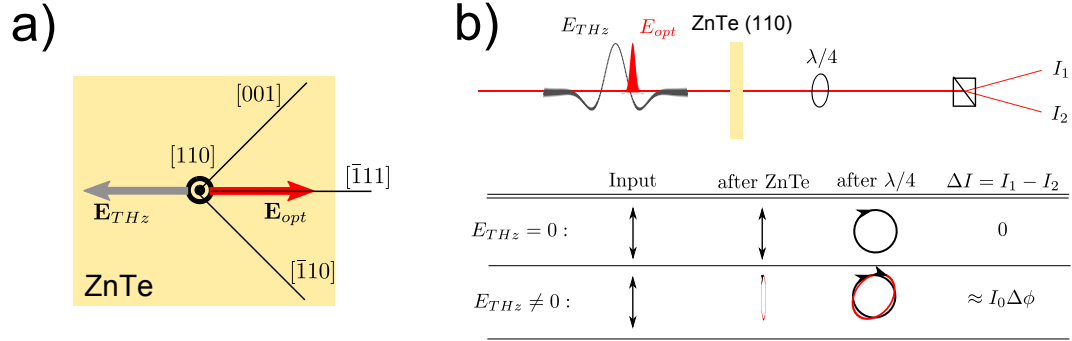


Figure 3.7: Diagram of electro-optic sampling (EOS) method; (a) ZnTe crystal, optical, and THz polarizations for the case of maximum THz-induced birefringence; (b) Schematic of how the polarization state of the probe pulse evolves through the optics train of the EOS setup, without and in the presence of a THz wave.

As was already mentioned in the previous section, electro-optic sampling (EOS) relies on the Pockels effect. When a DC electric field is applied to a material possessing  $\chi^{(2)}$  response, it induces an index of refraction change. In the case of THz pulse, the induced birefringence is sampled by analyzing the polarization state of a probe pulse. Since its first demonstration [136, 116, 137], EOS is one of the most common coherent methods of THz detection and is typically performed using a ZnTe.

Consider an optical pulse of intensity  $I(t)$  propagating through a very thin<sup>†</sup> zincblende crystal at an angle  $(\theta, \phi)$  with respect to the optic axis of the crystal. THz intensity can be expressed:

$$I_{THz}(\theta, \phi) \propto d_{14}^2 I_{opt}^2 \sin^2(\theta) [4 \cos^2(\theta) + \sin^2(\theta) \sin^2(2\phi)] \quad (3.18)$$

where  $r_{41}$  is the only non-vanishing  $\chi^{(2)}$  tensor-element in ZnTe. As can be shown,  $I_{THz}$  is maximized at  $(\pm\pi/4, \pm\pi/4)$  directions, or when the optical wave is incident onto a  $\langle 110 \rangle$  oriented crystal at normal incidence, making an angle  $\pi/4$  with respect to the  $[001]$  axis (Fig. 3.7a). In such case, THz is polarized in the opposite direction to

<sup>†</sup>effects of phase-matching in a thick crystal have already been discussed in the previous section.

the optical field, namely along the  $[1\bar{1}\bar{1}]$  axis. Detection of the  $E_{THz}$  is accomplished by analyzing the polarization state of the optical pulse after passing through the ZnTe crystal (Fig. 3.7b). A combination of quarter-wave plate and a polarizing beamsplitter (Wollaston prism) used to detect changes in birefringence of ZnTe, induced by the THz pulse. After propagation through a crystal of length  $L$ , phase-retardation difference between orthogonally polarized components of the optical pulse is:

$$\Delta\phi = \frac{\omega L}{c} n_o^3 r_{41} E_{THz}. \quad (3.19)$$

where  $n_o$  is the refractive index at the probe frequency. The intensity difference after the Wollaston prism becomes:

$$\Delta I \approx I_0 \Delta\phi = \frac{I_0 \omega L}{c} n_o^3 r_{41} E_{THz}. \quad (3.20)$$

The electric field of the THz can be measured coherently upon detection of the intensity difference by a balanced detector fed into a lock-in amplifier.

### 3.4 THz-TDS experimental setup

Below we present details of our spectroscopic setup. It is highly versatile in terms of pump and probe options. The remaining description will concentrate on the details of the arrangement relevant for this work.

A home-built broadband Ti:sapphire oscillator (Chpt. 2.2.3) seeds a Ti:sapphire 1 kHz regenerative amplifier capable of producing 35 fs 3.5 mJ pulses centered at 805 nm (Chpt. 2.2.4). Optional OPA is used to downconvert the fundamental pulses into the MIR frequency band with 15% conversion efficiency (Chpt. 2.2.5). Amplified pulses of various frequencies are optionally split 50/50 and subsequently 75/25 by means of thin broadband optics (CVI)<sup>†</sup>. An optional spitting permits generation of

---

<sup>†</sup>unless noted otherwise, all the reflective optics are silver coated

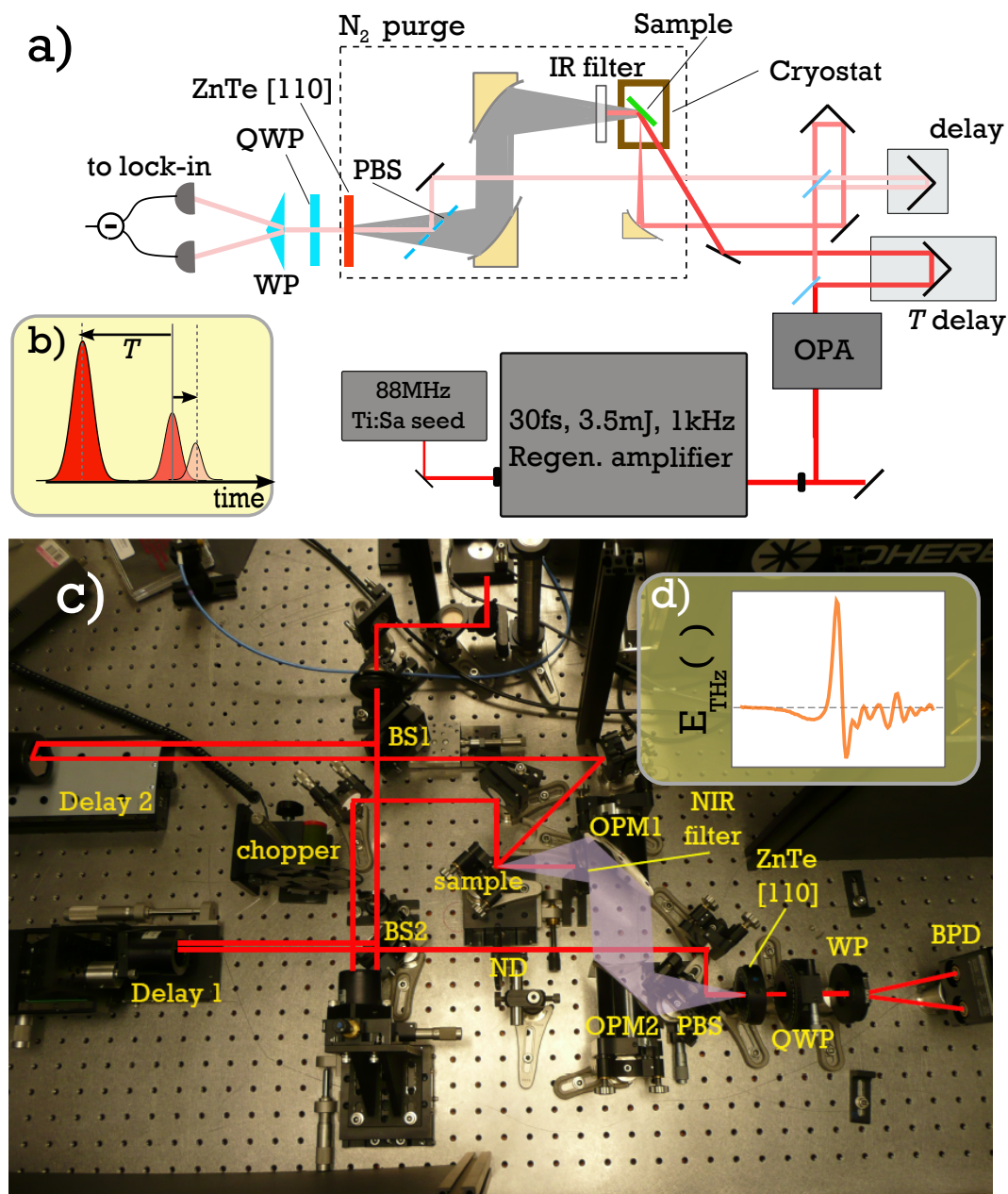


Figure 3.8: Schematic of the THz time-domain spectroscopy setup

3 unequal energy pulses (Fig. 3.8), which can be used for the pump-probe experiments. After the second unequal beamsplitter two more pulse replicas are generated. The stronger pulse is used to interrogate the sample (as described below), while the weak

is used as a gating pulse for electro-optic sampling of the emitted THz fields (EOS, Sec. 3.3.2). The interrogation pulse is focused onto the sample of interest by spherical metallic mirrors (various focal lengths used). Samples under study are optionally placed in the cryostat. A combination of movable focusing mirror and cryostat position enables the setup to function either in sample reflection or transmission modes. In both cases, generated THz radiation is imaged onto the detection crystal by a pair of aluminum-coated off-axis parabolic mirrors (OAPM), constituting a 1-1 telescope. The large numeric aperture OAPMs are used to efficiently collect diverging THz radiation and to avoid chromatic aberrations, otherwise present in the refracting telescopes. After THz generation in the sample, residual NIR/MIR beam is blocked by means of a silicon/teflon filter.

Weak NIR probe beam and THz are recollimated by means of a 20/80 pellicle beamsplitter. Focused THz spot and collimated NIR are incident onto a detection crystal of  $\langle 110 \rangle$  ZnTe of various thicknesses. After ZnTe, polarization state of the probe is interrogated as previously discussed (Sec. 3.3.2). Silicon based balanced detector (New Focus) is used in combination with a lock-in amplifier to detect electric signals proportional to the THz electric field. Two LabView controlled delay stages (one optional for the pump beam) are used to ensure time overlap and provide delay scan between relevant pulses. Delay stage calibrations are routinely checked by interference fringes from the NIR pulses. In the optional case of the OPA pulses, separate 90/10 pellicle beam splitter (before the parametric amplifier) is used to generate the gate pulse for the EOS (Fig. 2.5).

Bandwidth of the THz-TDS setup is determined by the detection crystal (Sec. 3.3.2) and probe pulse duration. To test the limits of our system we use 1mm GaSe emitter crystal in transmission geometry with the 0.5 mm ZnTe detector crystal. Gallium selenide is chosen as an emitter due to its Reststrahlen band lying at higher frequencies than in ZnTe. Figure 3.9 shows the emitted THz transient as detected using (typical) settings of 400 Hz chop frequency, 100ms/point lock-in integration time,

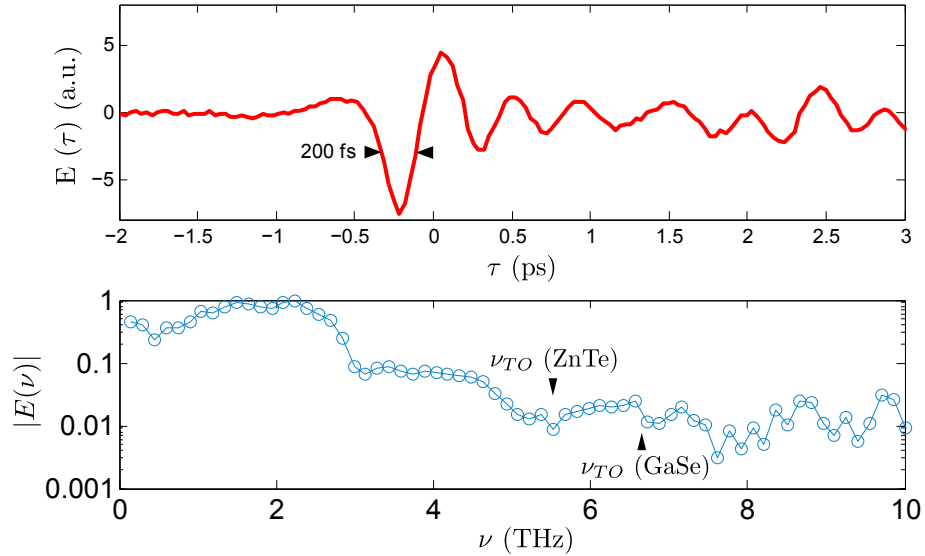


Figure 3.9: (a) Electric field emitted by 1 mm GaSe ( $\theta = 24\text{deg}$ ) and detected with 0.5 mm  $\langle 110 \rangle$  ZnTe; (b) Magnitude of the field spectrum reveals signal up to 7 THz, as verified by resolution of the absorption lines at TO phonon frequencies of the emitter (6.5 THz) and the detector (5.3 THz) crystals.

24 dB/oct bandpass filter and transimpedance gain of  $10^5$  on the balanced detector. The bandwidth test reveals that while most of the detected bandwidth is limited by the velocity-matching conditions in ZnTe (Sec. 3.2.2), there is still above-noise signal that extends to 7 THz, limited by the onset of the Reststrahlen band of the emitter crystal. This test also verifies that gate pulse duration is currently not the limitation of the temporal response of the system.

While the standard experimental arrangement is described above, we want to emphasize the generality of this spectroscopic system. In fact any arrangement with NIR/MIR/THz pump and NIR/MIR/THz probe is currently possible.

# Chapter 4

## Plasmon spectroscopy: local response

### 4.1 Introduction

In principle the dielectric function depends on both space and time, i.e.  $\epsilon(k, \omega)$ . In this chapter we are concerned with the long-wavelength limit of the dielectric function, namely  $\epsilon(k \rightarrow 0, \omega)$ . This is the local response of the medium and we focus on this regime for the remainder of this chapter.

Longitudinal modes do not emit radiation. We review conditions under which radiation is possible and discuss some of the consequences in coupling of that radiation to light line. Experimental results are provided in support of the explanation of the diffraction-based low-pass filtering.

We continue with the investigations of the temperature dependence of the long-wavelength plasmon in InSb semiconductor. The observed behavior can only be quantitatively explained by invoking non-parabolicity of the conduction band. Furthermore, we extract electronic mobility and show 20-30% agreement with the DC mea-

surements. These demonstrations position ultrafast THz spectroscopy as an ideal *non-contact* method to study transport on the nanoscale.

We conclude this chapter with the experimental demonstration of all-optical plasmon frequency control on an ultrafast time scale. Pre-injecting the photocarriers with a pump pulse, we probe the distribution to reveal nearly 20% induced plasmon frequency upshifts. Results are in good agreement with quantitative estimations.

## 4.2 Plasmons in narrow-gap semiconductors

Ultrafast terahertz spectroscopy provides an excellent low-energy probe of the collective excitations in a solid [108, 109]. Some of the most recent hallmark experiments include time-resolved studies of a role of phonons in formation of Cooper pairs in high- $T_c$  superconductivity [138, 139], magnon excitations via ultrafast magnetic field transients [140], polaronic nonlinear response [12], just to name a few. In this dissertation we are mainly concerned with the ultrafast terahertz spectroscopy of the plasmon modes.

Semiconductor plasmas have been the subject of study for a long time [141], but only recently have they been examined with the techniques of ultrafast spectroscopy [142]. Coherent oscillations of plasmon mode were first observed in pump-probe experiments with a biased GaAs p-i-n structures by Sha *et. al.* [143]. Electron-hole pairs are optically injected with 100 fs Ti:sapphire laser pulses and their subsequent oscillation observed in differential transmission. Cho *et. al.* monitored small changes in the reflectivity of 50 fs probe pulses from the surface of n-GaAs samples [144]. They found complicated oscillatory behavior involving cold plasmons doped into the semiconductor, hot plasma due to electron-hole pairs of the pump pulse, as well as coherent phonons. The emission of electromagnetic radiation by coherent plasmons in GaAs structures was reported by Kersting *et. al.* [128, 145]. The plasma frequency is



controlled by optical carrier injection or with donor-doping. A significant advantage of THz emission spectroscopy compared to pump-probe experiments is that radiation of *cold*, bulk plasmons is readily detected. Photocarriers from the ultrashort pump pulses are evidently too hot and/or inhomogeneous to contribute significantly to collective, macroscopic dipole emission.

The narrow-gap semiconductors such as InSb and InAs are attractive crystals for studying coherent plasmons because they possess high mobility leading to long-lived plasmon modes. They can be grown relatively very pure, which allows the intrinsic carrier concentration to be adjusted by many orders of magnitude, for instance by changing the sample temperature. In this way, the center frequency of the radiation can be temperature-tuned. We also perform experiments to blue-shift the plasma frequency by optically injecting carriers.

### 4.2.1 Starting mechanisms

The essential mechanism for starting coherent oscillations in narrow-gap semiconductors is the photo-Dember effect [146, 147]. Partial screening of the surface field by ultrafast photocarrier injection is known to initiate coherent plasmon oscillations in wider gap semiconductors such as GaAs [145], where these fields are  $\sim 10$  kV/cm. Surface field screening is expected to be negligible in the semiconductors n-InAs and n-InSb because the accumulation and depletion fields, respectively, are much weaker compared to GaAs [147, 148, 149]. The surface field screening and photo-Dember current are examples of displacive excitation<sup>†</sup> (see also Chpt. 3.2). It was recently shown that impulsive stimulated Raman scattering can launch both coherent plasmons and phonons in InSb, but requires pumping near the electronic resonance at 1.85 eV [150].

---

<sup>†</sup>excitation that is accompanied by the displaced equilibrium state of the electron ensemble

The photo-Dember mechanism works as follows: the near-infrared pump pulse (photon center energy: 1.5 eV) excites photocarriers far above the semiconductor bandgap ( $E_g = 0.228$  eV for InSb at 77 K). The absorption depth of pump light in InSb is  $\sim 100$  nm [151]. Ultrafast, ambipolar diffusion of electrons and holes leads to charge separation, with the resulting electric field pointing from the photo-generated holes to more rapidly moving electrons further beneath the surface. Cold electrons in the bulk move in response to this perturbing charge gradient. If the bandwidth of the electric field transient extends to cover the plasmon frequency, the cold electrons commence plasma oscillations between cold electrons and stationary ions.

### 4.3 Spectral characteristics

Consider an electron gas, subject to applied longitudinal field  $\mathcal{E}$ . As a result, the gas is displaced from equilibrium as a whole by a distance  $\mathbf{x}$ . The resulting collective motion of an electron ensemble (plasmon) can be represented by a simple harmonic oscillator [152]:

$$\frac{d^2\mathbf{x}(t)}{dt^2} + \gamma \frac{d\mathbf{x}(t)}{dt} + \omega_p^2 \mathbf{x}(t) = \frac{e\mathcal{E}(t)}{m} \quad (4.1)$$

where  $\gamma$  is the mobility of electrons (i. e. inverse momentum relaxation time, largely due to LO phonon scattering),  $\mathcal{E}(t)$  is the driving field (photo-Dember),  $m^*$  is the effective mass of the electrons. The electrons undergo an oscillation at frequency:

$$\omega = \sqrt{\omega_p^2 - \frac{\gamma^2}{4}}, \quad (4.2)$$

where  $\omega_p$  is:

$$\omega_p = \sqrt{\frac{Ne^2}{\epsilon_\infty m^*}} \quad (4.3)$$

with  $N$  - carrier density and  $\epsilon_\infty$  arises from the contributions of the valence electrons [153].

After performing Fourier transform on Eq. 4.1 and multiplying by  $eN$  ( $\mathbf{P} = Ne\mathbf{x}$ ) we can solve for electronic polarization  $\mathbf{P}(\omega)$ :

$$\mathbf{P}(\omega) = \frac{\omega_p^2 \boldsymbol{\mathcal{E}}(\omega)}{\omega_p^2 - \omega^2 + i\gamma\omega}. \quad (4.4)$$

Electromagnetic radiation is  $\mathbf{E}_{rad}(\omega) \propto i\omega\mathbf{J}(\omega) = -\omega^2\mathbf{P}(\omega)$  (Eq. D.14) and hence the spectral power density of the emitted radiation  $S_{rad}(\omega) \propto |E_{rad}(\omega)|^2$  is:

$$S_{rad}(\omega) \propto \omega^4 \frac{\omega_p^4 \mathcal{S}(\omega)}{(\omega_p^2 - \omega^2)^2 + \gamma^2\omega^2} \quad (4.5)$$

where  $\mathcal{S} = |\boldsymbol{\mathcal{E}}|^2$ . For small  $\gamma$ , radiation spectrum  $S_{rad}(\omega)$  is shaped by the plasmon pole at  $\omega_p$ . This means that even though the excitation mechanism emits broadband radiation  $\mathcal{S}(\omega)$ , the system will emit into the narrow mode defined by the plasmon frequency<sup>†</sup>, amplitude of the emission  $\propto \mathcal{S}(\omega_p)$  (Eq. 4.5) [5]. When we analyze the emitted spectrum from plasmon systems, we can attribute the lineshape as due to the plasmon only, provided it overlaps with the excitation bandwidth  $\mathcal{S}(\omega_p)$ . This fact becomes important when we use the lineshape to extract carrier density and electronic mobilities. Note that if excitation spectrum  $\mathcal{S}(\omega)$  overlaps with the plasmon mode, then only for the cases of  $\gamma \gg \omega$  or  $\omega_p \sim 0$  one can expect to see emitted spectrum directly from the  $\mathcal{S}(\omega)$  contribution.

## 4.4 Radiation from a semi-infinite medium

An arbitrary-wavelength plasmon is a longitudinal mode of the system (Appx. E). Fundamentally speaking, an infinitely extended longitudinal mode can not emit electromagnetic radiation. In cases when *excitation volume is much smaller than the emitted wavelength*, radiation is allowed by the virtue of a Hertzian dipole approximation (Eq. D.19). In this case, the wavevector  $\mathbf{k}$  of the radiation acquires high degree of directional bandwidth (uncertainty principle), which leads to possibility of

---

<sup>†</sup>or other poles of the response, for instance a phonon mode

coupling to light line. In the local response approximation ( $q \rightarrow 0$ ), the bulk plasmon mode is dispersion-less and hence has a definite intersection with the lightline. The coupling to lightline is ensured by the Hertzian nature of the radiator.

These arguments are valid in the limit of point source excitations. For extended sources, the coupling can be examined from the standpoint of the radiation integral (Eq. D.14). It relates the far-field radiation to the spatial Fourier transform over the current distribution, namely:

$$\mathbf{E}(\mathbf{r}, \omega) = -\frac{i\omega}{4\pi\epsilon_0 c^2} \frac{e^{ikr}}{r} \hat{\mathbf{k}} \times \hat{\mathbf{k}} \times \int e^{-i\mathbf{k}\cdot\mathbf{r}_s} \mathbf{J}(\mathbf{r}_s, \omega) d^3 r_s. \quad (4.6)$$

By inserting the Fourier representation for the  $\mathbf{J}(\mathbf{r}_s, \omega) = -i\omega\mathbf{P}(\mathbf{r}_s, \omega)$ , where  $\mathbf{q}$  is the wavevector of the source:

$$\mathbf{J}(\mathbf{r}_s, \omega) = -i\omega \frac{1}{(2\pi)^{3/2}} \int e^{i\mathbf{q}\cdot\mathbf{r}_s} \mathbf{P}(\mathbf{q}, \omega) d^3 q \quad (4.7)$$

into Eq. 4.6 we obtain:

$$\mathbf{E}(\mathbf{r}, \omega) = -\frac{\omega^2}{4\pi(2\pi)^{3/2}\epsilon_0 c^2} \frac{e^{ikr}}{r} \hat{\mathbf{k}} \times \hat{\mathbf{k}} \times \int d^3 q \mathcal{E}(\mathbf{q}, \omega) \left(1 - \frac{1}{\epsilon(\mathbf{q}, \omega)}\right) \int d^3 r_s e^{-i(\mathbf{k}-\mathbf{q})\cdot\mathbf{r}_s} \quad (4.8)$$

where we used consequential relationship between  $\mathbf{P}$  and  $\mathcal{E}$  from Eq. 4.4.

We first perform integral over the spatial extent of the source, therefore some specifications of the excitation geometry are required. Without loss of generality consider a planar interface in x-y plane of index  $n$  (such that  $\mathbf{k} \rightarrow n\mathbf{k}$ ). In this work, all the plasmon excitations are nearly *cylindrically symmetric*, which naturally leads us to the choice of cylindrical coordinates:

$$\int d^3 r_s e^{-i(n\mathbf{k}-\mathbf{q})\cdot\mathbf{r}_s} = \int_0^L dz e^{-iQ_z z} \int_0^{2\pi} \int_0^{D/2} \rho d\rho d\phi e^{-iQ_\rho \rho \cos\phi} \quad (4.9)$$

where  $Q_z = (nk \cos\theta - q_z)$  and  $Q_\rho = (nk \sin\theta - q_\rho)$ . This gives solution of the form:

$$\int d^3 r_s e^{-i(n\mathbf{k}-\mathbf{q})\cdot\mathbf{r}_s} = \pi L D e^{iQ_z L/2} \text{sinc}\left(\frac{Q_z L}{2}\right) \mathcal{A}\left(\frac{Q_\rho D}{2}\right), \quad (4.10)$$

where

$$\mathcal{A}\left(\frac{Q_\rho D}{2}\right) = \frac{J_1\left(\frac{Q_\rho D}{2}\right)}{\frac{Q_\rho D}{2}} \quad (4.11)$$

is an Airy disk function with  $J_1$  being the Bessel function of the first kind. The radiated field from the dielectric response to an excitation  $\mathcal{E}(\mathbf{q}, \omega)$  in the cylindrical volume with diameter  $D$  and length  $L$  is:

$$\begin{aligned} \mathbf{E}(\mathbf{r}, \omega) &= \omega \frac{k^2}{4(2\pi)^{3/2}\epsilon_0} \frac{e^{ikr}}{r} LD \hat{\mathbf{k}} \times \hat{\mathbf{k}} \times \int d^3q \mathcal{E}(\mathbf{q}, \omega) (1 - \epsilon^{-1}(\mathbf{q}, \omega)) \times \\ &\quad \times e^{iQ_z L/2} \text{sinc}\left(\frac{Q_z L}{2}\right) \mathcal{A}\left(\frac{Q_\rho D}{2}\right) \end{aligned} \quad (4.12)$$

For the cases of interest here, plasmon modes propagate perpendicular to the interface, due to the nature of the longitudinal excitation mechanism. Therefore, the plasmon wavevector  $\mathbf{q} = q_z \hat{\mathbf{z}} + q_\rho \hat{\rho} \rightarrow q \hat{\mathbf{z}}$ , in that we assume no transverse component ( $\mathcal{E} = \mathcal{E} \hat{\mathbf{z}}$ ). With this, Equation 4.12 becomes:

$$\begin{aligned} \mathbf{E}(\mathbf{r}, \omega) &= \hat{\boldsymbol{\theta}} \frac{k^2 LD}{4(2\pi)^{3/2}\epsilon_0} \sin \theta \frac{e^{ikr}}{r} \mathcal{A}\left(\frac{nk \sin \theta D}{2}\right) \times \\ &\quad \times \int dq \mathcal{E}(q, \omega) (1 - \epsilon^{-1}(q, \omega)) e^{iQ_z L/2} \text{sinc}\left(\frac{Q_z L}{2}\right). \end{aligned} \quad (4.13)$$

where  $\hat{\mathbf{k}} \times \hat{\mathbf{k}} \times \hat{\mathbf{z}} = \sin \theta \hat{\boldsymbol{\theta}}$  was used (see Eq. D.22) and  $Q_z = (nk \cos \theta - q_z)$ .

First we analyze the term  $\mathcal{A}(x \sin \theta)$  which results from the diffraction from circular aperture of radius  $R$ , with  $x = n2\pi D/\lambda$ . We require our excitation to be much smaller than the radiated wavelength ( $x \ll 1$ ), in which case  $\lim_{x \rightarrow 0} \mathcal{A}(x \sin \theta) = 1$  for all angles  $\theta$ . In this limit, the angular properties of the radiation are dictated not by the diffraction but by the Hertzian dipole term, namely  $\sin \theta$  (Eq. 3.1). For cases when  $D$  becomes comparable to  $\lambda/n$ ,  $\sin \theta$  has to reduce accordingly in order to keep the argument of Airy disk function small (ensuring constructive contribution to the total radiation). This situation is depicted in Figure 4.1, where the radiated

pattern is plotted in a polar plot. For instance, in the case of  $x = \pi$  (black), constructive interference is only observed for small angles, leading to total cancellation of the radiation for  $\theta = \pi/2$ . Reduction of the angle  $\theta$  implies that the k-vector of the radiated energy points parallel to the dipole axis, implying reduced out-coupling of the radiation (Fig. 4.1). These arguments also can be made about the spectral response. For a fixed spot size  $D$ , radiated spectrum contains wavelengths that satisfy  $\lambda \gg nD$ . *The excitation spot size exhibits a high-pass wavelength filter for the emission spectrum.* Contribution from wavelengths smaller than the excitation spot size is effectively averaged out. This is in direct analogy with the phase-matching arguments presented in the previous chapter. This wavelength filtering is diffraction.

In general,  $q_z$  is not zero. The finite nature of  $q_z$  is considered in the next chapter where we are concerned with the non-local response. In the case of local response,  $q \rightarrow 0$ , the phase-matching condition for the *sinc* becomes:

$$\frac{2n \cos(\theta)L}{\lambda} = 0. \quad (4.14)$$

This can either be accomplished with  $\theta \rightarrow \pi/2$  or  $L/\lambda \ll 1$ . The former will lead to bound modes and it is not surprising, since the spatially-extended longitudinal modes do not radiate. Thus, we see again that the Hertzian condition ( $L \ll \lambda$ ) has to be satisfied to couple to light cone.

These “phase-matching” conditions put constraints onto the excitation volume. For instance, in photo-Dember excitation,  $z$  direction is ensured to be much smaller than wavelength by narrow absorption depth (100 nm) and fast ambipolar diffusion. In the transverse dimension, laser spot excitation has to be matched for the given detection bandwidth of interest. To give an example, we consider plasmon radiation from InAs centered at 1 THz, with the corresponding internal wavelength of  $80\mu\text{m}$ . This length scale poses no problems for the the  $z$ -axis: absorption and diffusion length scales are  $< 1\mu\text{m}$ , but the in-plane (x-y) focusing must be near or below

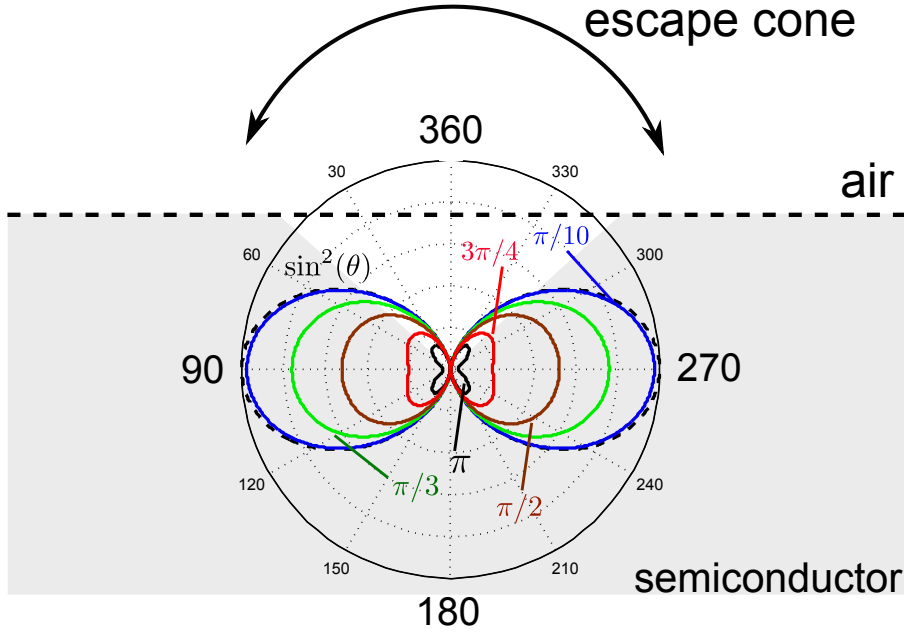


Figure 4.1: Polar plot showing the effect of the spot-size-to-wavelength ratio ( $x$ ) on the radiation pattern and out-coupling efficiency. Plotted equation is  $\sin^2 \theta [2\mathcal{A}(x \sin \theta)]^2$ , for cases  $\frac{\pi n D}{\lambda} = x = [0, \pi/10, \pi/3, \pi/2, \pi/3, 3\pi/4, \pi]$ . Dipole is depicted inside of the semiconductor material with indicated escape cone. Modes that overlap with the escape cone are considered radiating, while the bound modes are trapped via total internal reflection [154]. Reduced overlap of the radiation pattern with the cone for increasing  $x$  is observed; the largest overlap corresponds to the Hertzian dipole  $\sin^2 \theta$  case. For a beam size much larger than the wavelength.

the  $80\mu\text{m}$  scale. To resolve the phonon modes,  $\sim 8$  times smaller excitation spot is required.

To summarize, for the case of the localized excitation (in three dimensions) the radiator behaves as a Hertzian dipole. Once the excitation volume approaches the size of the wavelength, however, decrease in efficiency and spectral cut-offs are expected. In essence, we have started with the spatial distribution and reduced it to point-source dipole. The expressions will prove useful however when dealing with cases of non-local response, where  $\mathbf{q} \neq 0$  in the next chapters.

Even for small excitation volumes, problem of radiation outcoupling is severe in

high index semiconductors. Coupling to light line is only possible within a narrow cone defined by  $\theta_c = \arcsin(1/n)$ , - the condition of total internal reflection, and sketched as the triangle in (Fig. 4.1). For example, for InAs with  $n = 3.7$  at 1 THz [155], the resultant  $\theta_c = 15.6^\circ$  implies that less than 0.5% of the total radiated Hertzian dipole power is coupled into free space. For incidence angles  $\theta$  greater than the apex angle of the escape cone, radiation results in bound modes [154, 148]. We note for completeness that the refractive index is a complex quantity and can be highly dispersive in the vicinity of the plasmon and optical phonon frequencies. Plasma oscillations are strongly damped in InAs, however, so the complex index is relatively constant at and above 1 THz.

The radiation trapping problem is well understood (see for e. g. [154] and discussion in Chpt. 4). Several schemes have been developed for improving the extraction efficiency. The direction of charge carrier motion has been altered by the Lorentz force where a large DC magnetic field ( $\sim 1$  Tesla) which rotates the dipole to preferentially orient one lobe of the radiation pattern in the escape cone [148, 156]. Another approach is to implement structured surfaces such as low absorption, index-matched prism stripes[157] or metal edges [158]. As will be shown in Chpt. 5, free standing nanowires possess natural geometric advantage for radiation outcoupling. In the case when waveguide is much smaller than the wavelength, all modes can radiate. This in effect is equivalent to stating that the effective index of the waveguide is near unity.

## 4.5 Experiments: InSb

We measure the frequency and coherence length of far-infrared radiation emitted by slab plasmon oscillations by use of an interferometric arrangement. Excitation is a p-polarized, 60-fs Ti:sapphire laser oscillator (center wavelength:  $\sim 820$  nm). Two pulses are temporally delayed and spatially separated in a Michelson interferometer (Fig. 4.2). The two near-infrared beams irradiate slightly separated spots on the



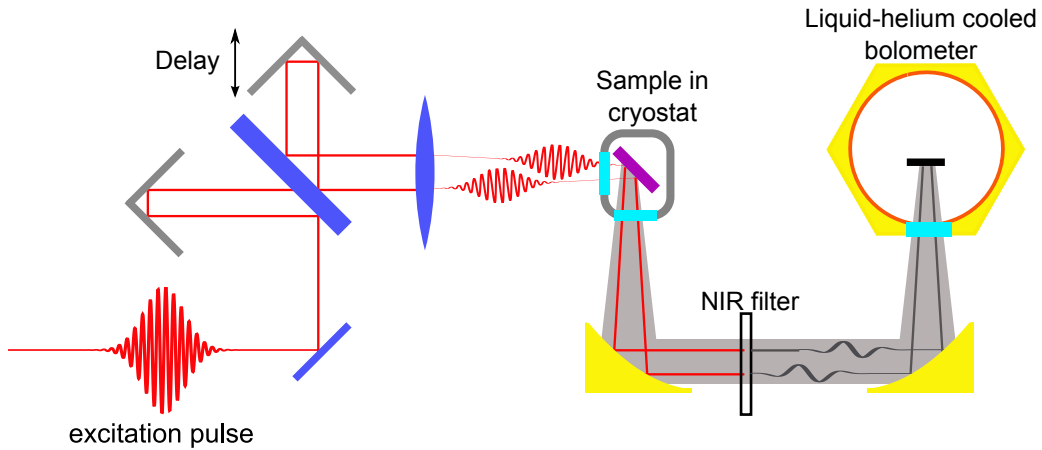


Figure 4.2: Experimental arrangement for incoherent THz detection.

semiconductor at an incidence angle of approximately  $45^\circ$ . The generated THz beams propagate along the direction of specular reflection where they are collected and collimated by an off-axis parabolic mirror. Reflected pump light is absorbed with a thin Teflon filter placed in the collimated path; this filter transmits in the far-infrared. A second mirror focuses the THz radiation onto a silicon bolometer detector cooled with liquid helium. Linear autocorrelation traces are generated by scanning one arm of the interferometer. A mechanical chopper modulates the pump beams at  $100\text{Hz}$  to permit lock-in detection of the bolometer signal. We limit the pump beam irradiance to prevent generation of THz radiation due to nonlinear difference frequency mixing in the broad spectrum of the ultrashort pulse. The THz beam path can be purged with dry nitrogen gas to mitigate water vapor absorption. Low temperature experiments are performed by placing the sample on the cold finger of an optical cryostat. The  $\text{MgF}_2$  output window of the cryostat limits the high frequency response to below 3 THz.

This arrangement approximates THz Michelson interferometer, relying on the assumption of spatial homogeneity of the sample properties. This arrangement is beneficial in that it avoids losses introduced by a THz beamsplitter or the difficulty

of individually aligning weak, far-infrared beams [159]. In addition, pump beam spatial overlap on the sample surface and effects of a temporally-advanced third pump pulse can be studied.

It is important to point out that THz interferometry prevents us from measuring the phase of the electric field relative to the excitation laser pulse, i.e. these measurements are not phase-resolved. This is in contrast to electro-optic sampling, and the benefits of either detection scheme have been reviewed in Chpt. 3. The main advantage of our approach is its nearly uniform, broadband response.

### 4.5.1 Plasma control: temperature

To study the temperature dependence of the plasmon mode in a (111) InSb bulk semiconductor with the trace donor concentration of  $N_D = 3 \times 10^{14} \text{ cm}^{-3}$ . We place the sample onto a coldfinger of a top-fill liquid nitrogen cryostat. Figure 4.3 depicts the results of the experiment of varying the sample temperature. In panel (a) autocorrelations of the radiation emitted by the sample are shown as a function of temperature. Traces are plotted on the same relative scale and displaced vertically for clarity. The temperature-dependent plasmon frequency is obtained from a Fourier analysis of the interference signals and plotted in Fig. 4.3b (filled circles). Next, we model the temperature dependence in order to understand this behavior.

With increasing temperature, three features can be observed: 1) the amplitude of the oscillations decreases, 2) the damping increases, and 3) the frequency blue-shifts [160]. The temperature-dependent plasma frequency is explained by the changing electron concentration in the semiconductor. The intrinsic concentration of InSb follows the empirical formula [162]:

$$N_i = 5.7 \times 10^{14} T^{3/2} e^{-0.125/k_B T} \quad (4.15)$$

where  $T$  is in Kelvin and density is in units of  $\text{cm}^{-3}$ . There is no donor freeze-

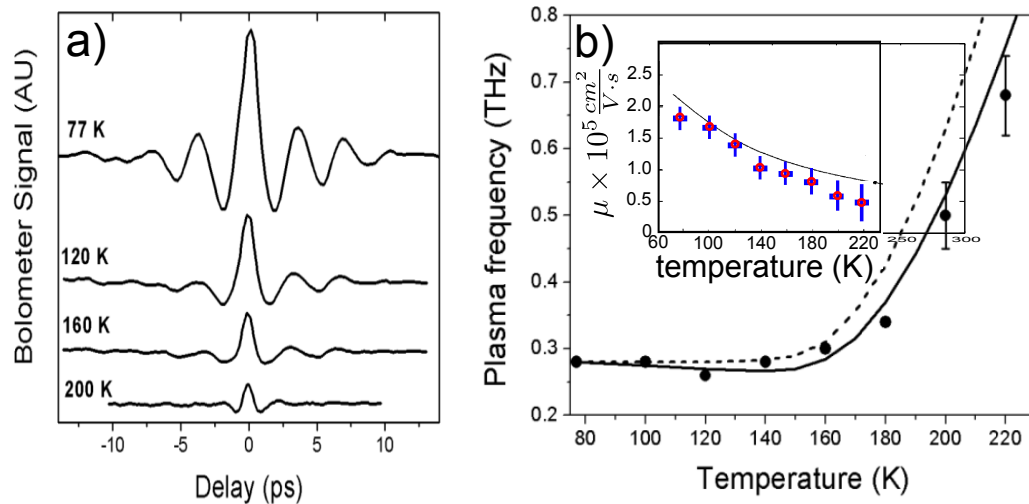


Figure 4.3: Temperature dependent InSb plasma frequency: (a) Autocorrelation traces of InSb plasmon emission as a function, parametrized by temperature; (b) Experimentally obtained plasma frequency versus temperature (solid circles) versus the predicted behavior with (solid line) and without (dashed line) taking into account conduction band non-parabolicity; (inset) Temperature-dependent InSb mobility is determined from plasmon emission with constant (blue) and density-dependent (red) effective mass and compared to published Hall mobility (black line, Mathur *et. al.* Fig.1 [161]).

out in narrow-gap InSb, so the donor concentration does not change with  $T$ . The conduction electron density  $N$  is determined from the condition of charge neutrality:

$$N^2 - NN_D - N_i^2 = 0. \quad (4.16)$$

With  $N_D$  and  $N_i$  (Eq. 4.15) we can compute  $N$ . To determine the plasmon frequency we have to know  $m^*$ . We assume that the positive donor ions are stationary, which means that only curvature of the conduction band contributes to the mass. With  $m^* = 0.013m_e$ , and  $\epsilon_\infty = 15.64\epsilon_0$ , the result of the calculation is shown in Fig. 4.3b as dashed line. The fit is not particularly good for temperatures higher than 160 K. Around these temperatures this sample exhibits transition from extrinsic to intrinsic regime. It is known that in narrow gap semiconductors, such as InSb, the electron

effective mass depends on both temperature and density [163]. Using this dependence (Eq. 12 of Ref. [163]) we plot the modified temperature dispersion of the plasmon as a solid line in Fig. 4.3b. Good agreement is found, emphasizing the importance of non-parabolicity correction. We point out the contribution of the photocarriers generated by the ultrashort pump pulse is not included in this calculation.

In addition to center frequency, we also analyze the damping rate, as given by the plasmon linewidth  $\Delta\nu_{FWHM}$ . Electronic mobility can be determined by:

$$\mu = \frac{e}{m^* \Delta\nu_{FWHM}}. \quad (4.17)$$

We compute the mobility from Eq. 4.17 using both density-dependent [163] and constant effective mass (respectively red and blue curves in Fig. 4.3b(inset)). These results are compared with the measured Hall mobility of a relatively pure InSb [161]. The temperature trend is in good agreement with the DC measurement. Ultrafast mobility is 20-30% lower throughout the studied temperature range. We attribute this reduction to additional scattering processes which result from ultrafast dynamics, for instance the prominent electron scattering with hot holes [5, 144, 164, 165]. Therefore, the mobility, as determined from the THz emission, sets the low-bound estimate of the DC response.

To summarize, we applied techniques of ultrafast THz spectroscopy to study long-wavelength plasmon mode in InSb semiconductor. We measured and analyzed the plasma frequency shift, underscoring the importance of the non-parabolicity corrections. We have determined a lower bound of the electronic mobility in a *contact-less* method. As demonstrated, the data is in good agreement with the published results. While ultrafast scattering processes lower the electronic mobility, we argue that THz spectroscopy proves invaluable in characterization of micro- and nano- structures, as Hall-type measurements are complicated by unavoidable Schottky barriers, where the accompanying depletion region can be comparable to the nanostructure itself. Finally we note that the ultrafast nature of the THz probe results in direct charac-

terization of the plasma linewidth. CW THz spectroscopy is also possible, but more inferences have to be made during the analysis [9].

### 4.5.2 Plasma control: photo-doping

Next, we investigate the possibility of injecting the electron-hole pairs on an ultrafast time scale, preceding the probe pulses. We are motivated by the possibility of controlling the plasma response on an ultrafast timescale.

In these experiments we utilized 60fs oscillator with bolometric detection. To accomplish pump-probe arrangement, we split oscillator beam into 3, where strongest is used for the pump and two weaker ones serve as a probe in the Michelson interferometer (Chapter 3). We control mutual temporal delays between these pulses via two independent delay stages. The experiment is arranged such that the near-infrared pump pulse precedes the probe pulses by 50 ps. At this temporal separation, photocarriers from the pump have time to diffuse into the bulk, partially cool (but not recombine), and thus contribute to the cold carrier density. Results of plasmon frequency dependence on the pump intensity are shown in Figure 4.4. A blue-shift of the plasmon, accompanied by increased dephasing is clearly visible in the time domain autocorrelations (Fig. 4.4a). By analyzing the Fourier transforms (panel b), we plot the plasma frequency versus the excitation power (Fig. 4.4b). On a picosecond time scale the effects of recombination can be ignored<sup>†</sup> and thus the excited photocarrier density  $N_{ext}$  is:

$$N_{ext} = \frac{\alpha F_{ext}}{h\nu} \quad (4.18)$$

where  $\alpha$ ,  $F$  and  $\nu$  are absorption coefficient, fluence ( $\int I(t)dt$ ) and frequency of the pulse. Consider the plasma frequency before the pump pulse arrives:

$$\nu_0 = a\sqrt{N_0} \quad (4.19)$$

---

<sup>†</sup><http://www.ioffe.ru/SVA/NSM/Semicond/InSb/electric.html>

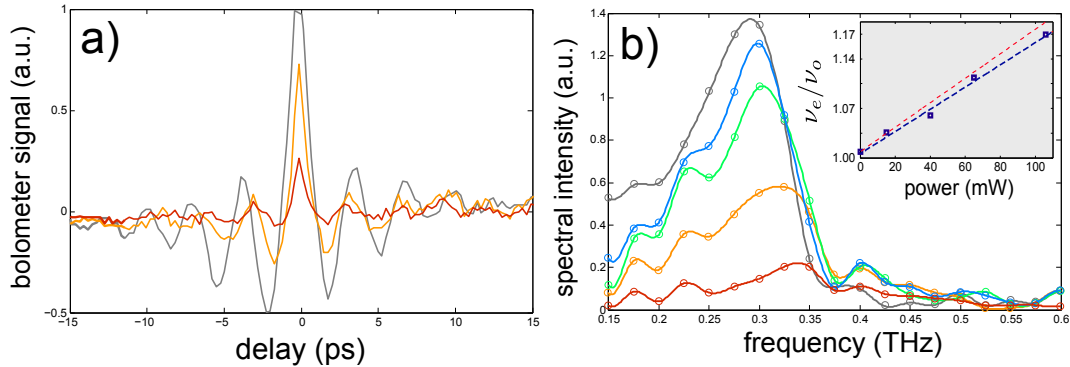


Figure 4.4: Optical control of the plasma frequency with the variable power pump at -50 ps: (a) Autocorrelation traces for several pump powers, the frequency blue-shift and pump-induced broadening (electron - hot hole scattering) is observed; (b) the resultant spectra also show blue-shift and spectral broadening; (inset) shows normalized plasmon frequency shift, defined as a ratio of the excited frequency  $\nu_{ext}$  to the background frequency  $\nu_0$  as a function of pump power. Data is fit with linear slope (blue) that is in good agreement with the prediction in the linearized approximation (red slope, Eq. 4.20); note nearly 20% pump-induced plasmon frequency upshift.

where  $a$  is a constant and  $N_0$  is the initial carrier density. The effect of the pump pulse on the frequency is:

$$\frac{\nu_{ext}}{\nu_0} = \sqrt{1 + \frac{\alpha F}{h\nu N_0}} \approx 1 + \frac{\alpha F}{2h\nu N_0} \quad (4.20)$$

for small frequency shifts. Figure 4.4b(inset) shows linear relationship of the normalized frequency with the pump power, consistent with Eq. 4.20. We note that at highest power we measure 17% pump-induced frequency shift. With  $\alpha = 10^5 \text{ cm}^{-1}$  [151],  $N_0 = 3 \times 10^{14} \text{ cm}^{-3}$  (no-pump), the slope in Eq. 4.20 is  $650 \text{ cm}^2/\mu\text{J}$ . With 110 mW, 88 MHz pump pulse train focused to  $50 \mu\text{m}$  (as verified by the aperture), the resultant fluence is  $145 \mu\text{J}/\text{cm}^2$ . The predicted frequency shift  $\nu_{ext}/\nu_0$  is 22%, in good agreement with the observed value of 17%. We note that the presence of additional broadening is due to electron collisions with hot holes [5, 144, 164, 165].

In summary, we have shown continuous tuning of the plasmon frequency on a picosecond time scale. The maximum shift of nearly 20% is currently limited by the

pump fluence. This serves as a proof-of-principle demonstration of a possibility to control plasmon dynamics on an ultrafast time scale.

# Chapter 5

## Non-local response: plasmon confinement

### 5.1 Introduction

Spatial non-local response is manifested in wavevector dependence of the dielectric response function,  $\epsilon(\mathbf{q}, \omega)$  (see Appx. E). Generally speaking, any characteristic length scale will affect modes of a system that have wavelengths comparable to that dimension.

A natural length scale in the case of an electron gas is posed by the inverse Fermi wavevector  $k_F$ , that describes the momentum distribution of the electronic states in a solid. For wavelengths of plasmon modes shorter than the inverse  $k_F$ , collective behavior is lost to individual particle excitations. This is the phenomenon of *Landau damping*. Landau damping is a manifestation of many-body interactions, which forms an important problem in theoretical condensed matter physics. For instance, correlated systems exhibit strong characteristics of non-local response.

For typical semiconductors, the onset of Landau damping occurs at length scales



of 50 - 100 nanometers. While posing no concerns for electron-quantum-confinement devices, this length scale is becoming increasingly important in the field of plasmonics. For carrier densities of  $\sim 10^{18} \text{ cm}^{-3}$ , effects of plasmon-electron interaction can be detrimental to the operation of plasmonic devices.

Motivated by these considerations, we study Landau damping in a solid-state plasma, as described in Section 5.2 of this chapter. We use InSb heterostructures to confine the plasmon mode in the direction of propagation. The plasmonic cavity allows us to clearly map both the dispersion relation and the onset of Landau damping. We compare our results with detailed calculations and discuss the role of phase-matching in considerations of radiation damping of the plasmon wave.

Devices based on control of plasmon resonances introduce new length scales, set by the geometry of the nanostructure design. Resonance is a manifestation of the non-local response and hence leads to modified dispersion relations of plasmon modes. Experimental investigations into the consequences of geometry-modified dispersion relations are particularly important for devices based on reduced dimensionality, such as nanowires. In Section 5.3 we present our experiments where we study THz emission from plasmon modes in InAs nanowires (NW). We identify these modes to be low-energy acoustic surface plasmons. This identification is also supported by modeling and independent electric transport measurements.

## 5.2 Landau damping

### 5.2.1 Background

Landau damping describes the behavior of an electron gas as it transitions from a collective, plasma state for modes with wavevector  $q \ll k_F$  to a system of individually interacting particles [166]. At sufficiently small dimensions, screening of Coulomb

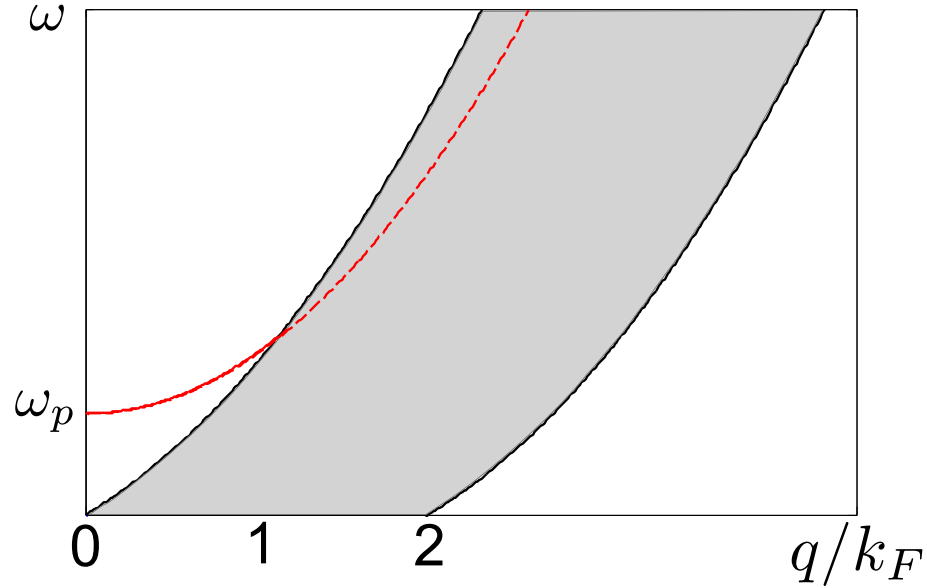


Figure 5.1: Plasmon dispersion of the form  $\omega^2(q) = \omega_p^2[1 + a(q/k_F)^2]$ ; shaded area, bounded by  $E_{max}$  and  $E_{min}$  ((Eq. 5.2), represents region of single-particle excitations. In that regime, collective plasmon mode loses energy to electrons, resulting in damping of the wave (dashed line).

perturbations cannot take place because the necessary collective behavior of the electron gas is lost. This corresponds to the case when  $q \sim k_F$ . Consider an electron gas at  $T = 0$  K occupying a sphere of radius  $k_F$  in momentum space. When an electron with momentum  $\hbar\mathbf{k}$  † absorbs a plasmon wave with momentum  $\hbar\mathbf{q}$ , the energy of the electron increases by:

$$E = \frac{\hbar^2(\mathbf{k} + \mathbf{q})^2}{2m^*} - \frac{\hbar^2\mathbf{k}^2}{2m^*} = \frac{\hbar^2}{2m^*}(\mathbf{q}^2 + 2\mathbf{k} \cdot \mathbf{q}). \quad (5.1)$$

The maximum electron wavenumber is  $k_F$ , so  $\mathbf{k} \cdot \mathbf{q}$  identifies the energy bounds for which this interaction can take place:

$$E_{max,min} = \frac{\hbar^2}{2m^*}(q^2 \pm 2qk_F). \quad (5.2)$$

---

†here Umklapp processes are ignored as the magnitude of electronic wavenumbers of interest is considerably less than the inverse lattice periodicity.

Figure 5.1 displays the area of energy and momentum conservation for the case of plasmon-electron interaction (shaded). A plasma wave is described by the dispersion of the form  $\omega^2(q) = \omega_p^2(1 + a(q/k_F)^2)$  ( $a=\text{const}$ , Eq. E.12) will cross the shaded region of allowed single-particle excitations (SPE) at some wavevector  $q' \sim k_F$ . For wavevectors larger than  $q'$ , the plasmon mode will be accompanied by excitation of the electrons above the Fermi surface, leading to energy dissipation of the collective mode. This is the description of the collision-less damping and is in principle a reversible process. The boundary of the single-particle excitation region is sharply defined for  $T = 0$  K and becomes broadened for finite temperatures.

Landau damping was first experimentally verified in gaseous plasmas [167]. In solid-state plasmas it has been studied using Raman scattering [168] and electron energy loss spectroscopy [169], but these experiments are usually difficult to interpret because of the highly inhomogeneous charge carrier distributions involved. Such spatial inhomogeneity implies finite and wide bandwidth in the wavenumber describing the plasmon mode. Finite bandwidth results in complications for determining the dispersion relation of the plasmon (Fig. 5.1).

Our experiments are based on an electron-donor ion plasma in bulk indium antimonide (InSb). By controlled confinement of the plasmon wavevector and analysis of the radiation it emits we can map the dispersion of the plasmon mode directly. Indium antimonide is an excellent material for this study because of its high mobility and possibility of high-purity growth, leading to long-lived plasmons in a bulk crystal ([160], Chpt. 4). This coherence is essential for observing both the plasmon shift due to the dispersion and mode broadening as expected in the Landau damping regime. The plasmon linewidth at  $q \approx 0$  is mostly determined by the incoherent scattering of electrons with the LO phonons [160]. We perform our experiments at 77 K, where reduced phonon population allows for a more coherent plasmon mode to exist.

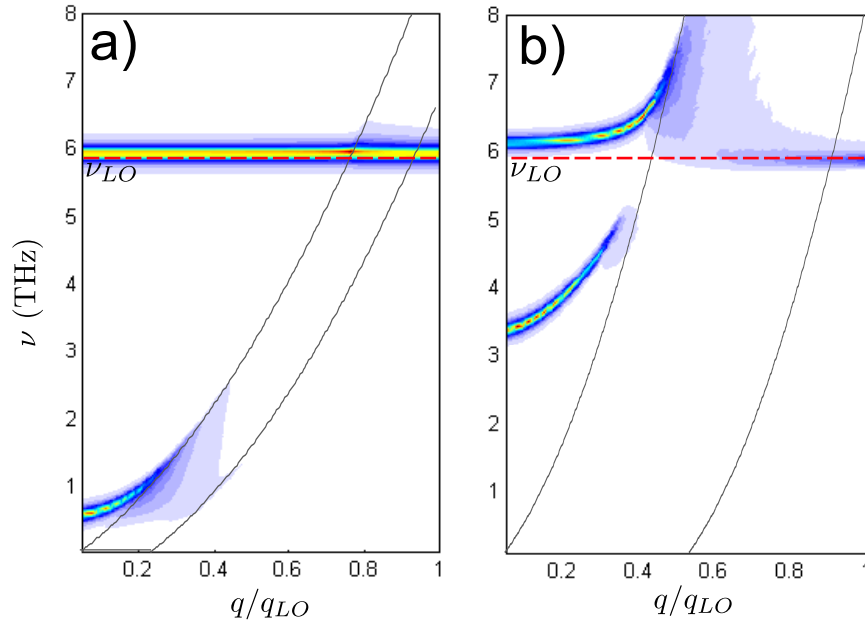


Figure 5.2: Calculated spectrum of longitudinal mode excitations in InSb at  $T = 1$  K for (a)  $N = 10^{15} \text{ cm}^{-3}$  and (b)  $N = 2 \times 10^{16} \text{ cm}^{-3}$  carrier concentrations. The color coding represents maxima in the  $\Im 1/\epsilon(q, \omega)$  function, which corresponds to the existence of the longitudinal modes (Appx. E). The region of single-particle excitation (SPE, Eq. 5.2) is bounded by two gray curves.

### 5.2.2 Numerical results

To correctly model the dispersion relation of the solid-state plasma waves we have to consider both the electron-electron interaction and lattice contributions to the dielectric function [166]. In this work, the electron-electron interaction is calculated within the random-phase approximation, using the Lindhard formalism (Appx. E) with the Mermin correction that incorporates the mode broadening self-consistently [166, 170]. Both Fermi-Dirac statistics (Eq. E.18) and conduction band non-parabolicity are included in the calculation [163]. Non-parabolicity is an important correction to the electron dispersion in narrow-gap semiconductors such as InSb.

In Figure 5.2 we present numerical results of the calculated spectrum of longi-

tudinal modes in InSb at  $T = 1$  K for two values of carrier concentrations. In the case of  $N = 10^{15} \text{ cm}^{-3}$  is shown in Fig. 5.2a. For the  $q = 0$ , the resulting plasma frequency  $\nu_p$  is at  $\sim 0.6$  THz and is considerably less than the bare LO phonon frequency  $\nu_{LO}$  at 5.91 THz. This frequency difference implies that both modes are nearly decoupled. There evidence of small coupling can be seen from a slight phonon frequency upshift with respect to the bare frequency shown as a red dashed line. For increasing values of  $q$ , plasmon mode exhibits frequency blueshift, as per the dispersion relation (Eq. E.12). The situation changes drastically when the plasmon mode overlaps the region where both energy and momentum are satisfied for interacting with the individual electrons. The result is a sudden damping of the plasmon mode. The oscillation loses coherence and exhibits spectral components that spread over the entire SPE region. As a manifestation of coupled modes, the phonon oscillation is also seen to broaden when in the region of SPE. The situation becomes even more complicated for the case of higher doping, as shown in Fig. 5.2b. Here,  $\nu_p$  is higher than in previous case which results in strong coupling with the phonon. This coupling is evidenced by a strong departure of the phonon frequency from the the bare  $\nu_{LO}$  frequency (dashed line). Upon increase in  $q$ , both modes are upshifting in frequency as yet another manifestation of the strong coupling. When the hybrid wave approached the SPE regime, both plasmon-like and phonon-like branches exhibit Landau damping. Here, the gray lines only approximate the SPE regime, since they represent bounds that were derived ignoring plasmon-phonon coupling (Eq.5.2). Upon further increase of  $q$ , when outside of the SPE regime, collective electron oscillations are lost, but the phonon mode emerges undressed, precisely at its own frequency  $\nu_{LO}$ .

Below we describe experimental results that are similar to the first numeric case, namely where coupling with the LO phonon can be ignored.

### 5.2.3 Experimental results and discussion

The experimental setup is identical to what was described in previous chapters. In short, a 60-fs Ti:Sa oscillator excites InSb samples at a 45 degree incidence angle. Short pulses excite a collective plasmon mode, which emits far-infrared radiation at THz frequencies. The radiated signal is detected in the direction of specular reflection using a liquid-helium cooled bolometer (Chpt. 3.3.1). The InSb sample is held at 77 K in an optical cryostat, fitted with a MgF<sub>2</sub> window that ensures high transmission for frequencies below 2 THz. Radiation emitted by coherent LO phonons (5.9 THz) however, cannot be detected in this arrangement. Using two identical pulses [128, 159, 160] we generate two THz excitations that interfere on the bolometer. The resulting autocorrelation traces provide spectral information (Chpt. 4).

Experiments are performed on a set of 5 high quality InSb heterostructures, grown by molecular beam epitaxy (MBE). Each heterostructure consists of a top layer of InSb which is separated from the (100)-oriented InSb substrate by a 40 nm barrier of Al<sub>0.1</sub>In<sub>0.9</sub>Sb. The resulting energy barrier in the conduction band is estimated to be  $> 80\text{meV}$ . The presence of the barrier defines a boundary condition for the plasmon wavevector confinement. The set of 5 samples is different in the thickness  $d$  of the top layer, which defines a plasmon cavity with the wavenumbers given by [171]:

$$q = \frac{l\pi}{d}, \quad (5.3)$$

where  $l$  is an integer. For a given layer thickness  $d$ , the minimum wavenumber occurs for  $l = 1$ , or  $q_{min} = \pi/d$ . By controlling the thickness  $d$  we can impose a varying low wavenumber cut-off for the plasmon mode. To accomplish this, the thickness is varied as follows:  $d = 1.5\mu\text{m}$ ,  $0.65\mu\text{m}$ ,  $0.5\mu\text{m}$ ,  $0.35\mu\text{m}$  and  $0.2\mu\text{m}$ . The exact values are based on the calculation and are chosen to adequately sample the dispersion relation near the onset of the Landau damping.

In the design of this experiment we rely on an assumption that the cold carrier

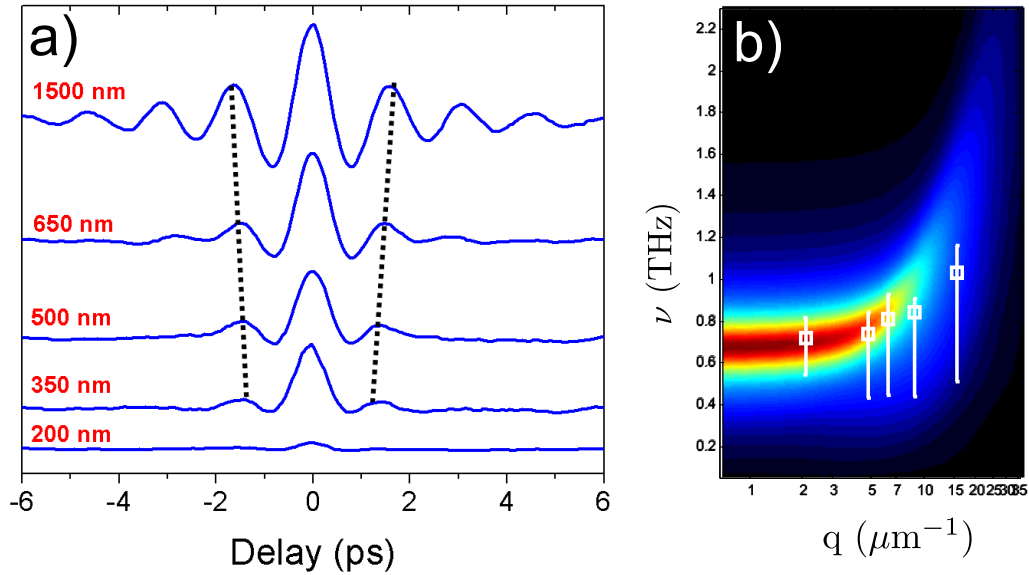


Figure 5.3: Observation of Landau damping of longitudinal plasmon mode in InSb at 77 K. (a) autocorrelation traces of the THz emission from progressively confined plasmon mode, blue shift (dotted lines) and damping (reduction in amplitude and coherence) are clearly visible; (b) Calculated spectrum of the plasmon dispersion (contour plot) and corresponding data, as obtained from Fourier analysis of (a).

density is the same in all the samples. We are operating in a regime of unintentional doping and hence it is nearly impossible to control the background doping precisely. To minimize this potential variation, our samples were grown in the course of one day (Center for High Technology Materials, Prof. Ralph Dawson). The samples of various thickness were grown in random order to further minimize potential systematic errors which could result from the slow MBE drift.

To estimate the effect the confinement has on electronic states, we assume the layer to represent a one dimensional square well potential of width  $d$ . The ground-state energy  $E_g = \hbar^2 \pi^2 / (2m^* d^2)$  of the electrons in the thinnest sample ( $d = 0.2 \mu\text{m}$ ) along the confinement direction is 0.7 meV, which is still much lower than the  $k_B T$  at the temperature of interest. We conclude that the confinement results only in the quantization of the plasmonic wavevector  $q$ , with negligible effects on the electronic

density of states.

Following the excitation of the plasmon mode by an ultrafast pulse, we detect the emitted radiation by interfering it on a bolometer in the far-field (Chpt. 4). The resulting autocorrelations are depicted in Figure 5.3a, where the background-subtracted traces are displaced vertically for clarity. The traces clearly show a progressive blue-shift of the plasmon mode (tilted dotted lines). Damping of the wave is evident from both loss of coherence (less fringes in the autocorrelation) and amplitude reduction. The contour plot of the calculated dispersion relation for the plasmon mode is shown in Figure 5.3b. The parameters of the calculation are obtained by fitting the plasmon linewidth for the long-wavelength response with  $q = 2.1\mu\text{m}^{-1}$  ( $d = 1.5\mu\text{m}$ ) and are:  $N = 1.5 \times 10^{15} \text{ cm}^{-3}$ ,  $\gamma = 1.2 \text{ ps}^{-1}$ . The Fourier transform data from the sample set is superimposed on the surface plot and is shown in white. The data qualitatively matches the calculation in that it reproduces both dispersion and broadening of the mode.

Before we make a conclusion that we indeed observe Landau damping of the plasmon wave we have to address the longitudinal nature of the plasmon mode. This implies that the plasmonic cavity can affect both the wavevector and the amplitude of the mode. The cold electrons see amplitude of the driving field  $E(t)$  (Eq. 4.1) that is bounded by the maximum Dember field, i.e. the field between the diffusing electrons and holes near the surface (Chpt. 4). Determining the time-varying amplitude of the excitation requires a self-consistent solution of the drift-diffusion and Poisson equations [145]. This is problematic because photocarriers injected by the ultrashort laser pump pulse are very hot and their mobility and diffusion coefficients are uncertain. We can place an upper limit on the excitation field by noting that inter-valley transfer occurs at  $\sim 500 \text{ V/cm}$  in InSb accompanied by drastically reduced mobility [172, 173]. This inter-valley scattering occurs on a timescale that is short compared to a plasma period [174]. The experimental realization of long-lived plasma oscillations damped at a rate consistent with LO phonon scattering sug-



gests that inter-valley scattering of cold electrons is not present in our experiments with bulk InSb. This in turn implies that photo-Dember fields are estimated to be  $E < 500$  V/cm. By modeling a spatially uniform field  $E(t) = 500$  V/cm with 50 fs rise time, we estimate an upper limit for the maximum displacement of coherent plasmon motion in our cold InSb sample as 250 nm. We conclude that in our samples amplitude is not distorted by the presence of a plasmonic cavity. It was important to estimate these effects in that it allows us to attribute observed blue-shift with the subsequent broadening increase to the onset of the Landau damping.

A plasmon in a local response is well approximated by the Hertzian dipole, in that  $\mathbf{q} \approx 0$ . In the case of the non-local response some modifications to the radiation pattern are expected (Chpt. 4). Since excitation is perpendicular to the surface, we can use Eq. 4.13 with the  $\int dq_z \rightarrow \pi/L \sum_l$ , such that:

$$\begin{aligned} \mathbf{E}(\mathbf{r}, \omega) &= \hat{\boldsymbol{\theta}} \frac{\pi k^2 D}{4(2\pi)^{3/2} \epsilon_0} \sin \theta \frac{e^{ikr}}{r} \mathcal{A} \left( \frac{nk \sin \theta D}{2} \right) \times \\ &\times \sum_{l=0}^{\infty} \mathcal{E}(l\pi/L, \omega) (1 - \epsilon^{-1}(l\pi/L, \omega)) e^{iQ_l L/2} \text{sinc} \left( \frac{Q_l L}{2} \right), \end{aligned} \quad (5.4)$$

where  $Q_l = nk \cos(\theta) - l\pi/L$  (see Chpt. 4). Phase-matching occurs when argument of *sinc* function  $Q_l L/2$  goes to zero. Phase-matching can not be accomplished in this case, because  $L/\lambda \ll 1$ . Radiation however can still occur when:

$$\frac{\pi n \cos(\theta) L}{\lambda} - \frac{l\pi}{2} = n \frac{\pi}{2} \quad (5.5)$$

where  $n$  is an odd integer. Since plasmon cavity length  $L$  is much smaller than the wavelength, Eq. 5.5 is satisfied for nearly any arbitrary  $\theta$ , provided  $l$  is also odd, with the dominant term being  $l = 1$ . The Airy disk function affects the phase-matching conditions in the plane of the interface, by imposing a high-pass filter for the wavelength content of the detected spectrum (Chpt. 4). In this experiment the excitation spot size  $D$  is 100  $\mu\text{m}$  and internal wavelength for low-q mode at 0.6 THz is  $3 \times 10^8 / 0.6 \times 10^{12} / 4.5 = 110 \mu\text{m}$ . Upon sampling the plasmon at higher

wavevectors the frequency blueshifts to 1 THz, corresponding to 55  $\mu\text{m}$  wavelength, which is below the spot size of the excitation. As can be seen from the data, the high- $q$  modes are red-shifted with respect to the calculation, which is qualitatively explained by the low-pass frequency filtering due to the excitation spot size.

In summary, we have engineered a plasmon cavity by which we were able to control the collective mode dispersion, as verified experimentally from the systematic blue-shift of the emission. By selection of the cavity modes, we forced the plasmon into the dispersion region with the onset of Landau damping regime. We have observed the increased broadening and amplitude damping, in agreement with the calculation.

## 5.3 Acoustic plasmons in nanowires

In this part of the work we confine the plasmon mode in all 3 dimensions. Nanowires serve as natural plasmon nanocavities. Our investigation reveals them to be unusually efficient emitters of the THz radiation, originating from the low-energy acoustic surface plasmons. Supporting DC electric measurements are briefly discussed.

### 5.3.1 Samples and setup

We use InAs nanowires that were grown and characterized by our collaborators at Sandia National Labs in Albuquerque, NM and Livermore, CA. NWs are grown by metal-organic vapor phase epitaxy (MOVPE) using the vapor-liquid-solid (VLS) technique, on a (111)B surface of a Si-doped (n-type) GaAs wafer. A 1 nm layer of gold is deposited by surface electron beam evaporation. Gold is used for seeding the growth process of the NWs. To form these seeding sites, the sample is annealed under  $\text{AsH}_3$  at 600°C, resulting in formation of  $\sim 20\text{nm}$  gold nanoparticles. NWs

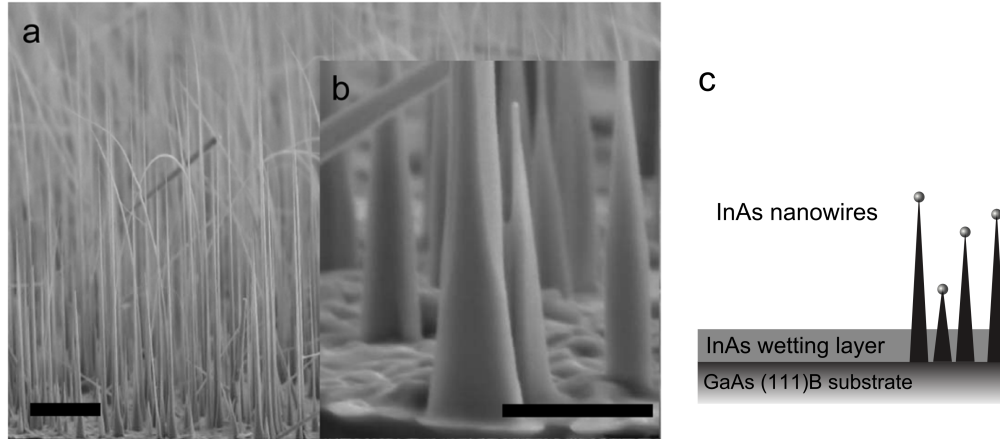


Figure 5.4: SEM image and schematic diagram of the InAs nanowire samples: (a) cross-sectional SEM image of the InAs NWs, the scale bar is  $3 \mu\text{m}$  (bottom-right corner); (b) higher magnification SEM image showing substrate-NW interface with the visible wetting layer (the scale bar is  $1 \mu\text{m}$ ); (c) Schematic diagram of the NW geometry.

are grown at a temperature of  $400^\circ\text{C}$ , in the presence of trimethyl indium (TMIn). Self-assembly nucleates at the gold sites, resulting in predominantly vertical growth, as can be seen from the scanning electron microscope (SEM) images, Fig. 5.4a,b. On average, nanowires are of conical shape of length  $15 \pm 5 \mu\text{m}$ , with the base of  $450 \pm 150 \text{ nm}$  tapering to the tip of  $65 \pm 15 \text{ nm}$ . The surface coverage is  $\sim 0.2 \mu\text{m}^{-2}$ . In the process of growth, the gold nanodroplet remains attached to the tip. Self-assembly at the gold sites is not the only growth process. As a result of competitive growth processes, a planar InAs *wetting layer* also forms on the GaAs surface (Fig. 5.4b). The layer thickness was estimated to be around  $200 \text{ nm}$  if all of the TMIn atmosphere was used for its production. The presence of the NWs indicates wetting layer thickness to be  $< 200 \text{ nm}$ .

We excite the InAs nanowires using ultrashort pulses from a mode-locked Ti:Sapphire laser oscillator (average pulse energy  $5 \text{ nJ}$ , duration  $60 \text{ fs}$ ) with wavelength centered at  $820 \text{ nm}$ . The p-polarized pulses are focused on the samples ( $\sim 400 \text{ nJ/cm}^2$ ) at

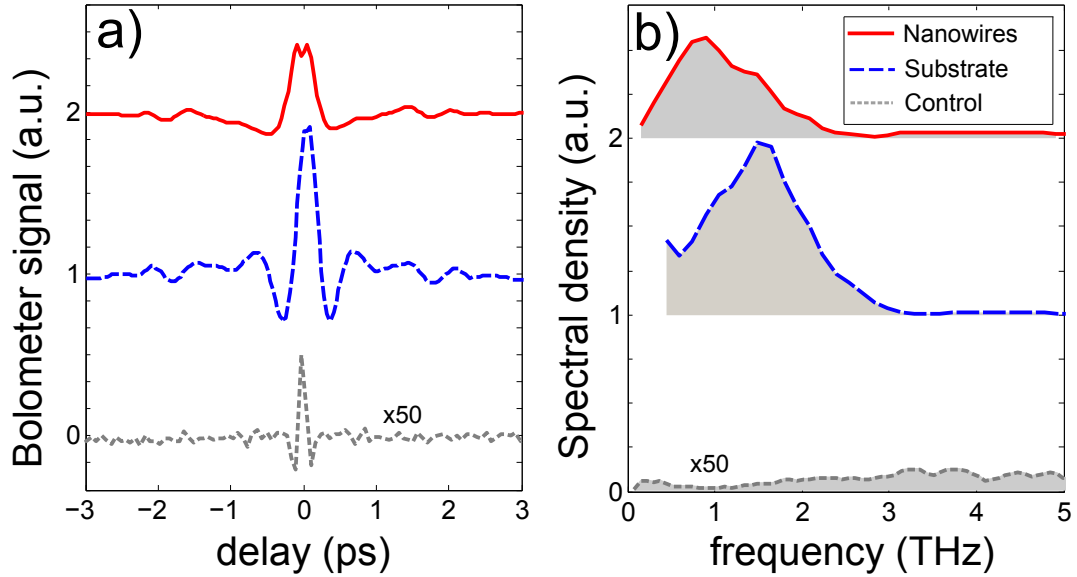


Figure 5.5: THz emission from bulk compared to InAs nanowires. Autocorrelation signals (a) and corresponding Fourier spectra (b) for an InAs nanowire sample (top), an InAs substrate (middle), and control sample (bottom) as described in the text. The top two signals are plotted on the same relative scale while signals from control sample are multiplied  $50\times$ . Top two curves are vertically offset for clarity.

an incidence angle of  $45^\circ$  with respect to the substrate surface. We characterize the emitted electromagnetic transients using linear autocorrelation [128, 5, 160, 159], i.e. by measuring the coherence length of the radiation with a Michelson interferometer (Chpt.3.3.1). The THz radiation is collected in the specular direction and imaged onto a liquid-He cooled Si-bolometer with a pair of off-axis parabolic mirrors. A teflon filter is inserted into the THz beam path to remove background laser light.

### 5.3.2 Experimental results and analysis

To isolate NW THz radiation from possible contribution from the wetting layer, we cleave one of the samples in two parts and remove nanowires from one of the pieces. This is done by ultrasonic cleaning and mechanical methods. We also verify under

optical microscope that no NWs are present after the removal procedure (NWs can still be seen on the untouched part of the substrate). In addition to the NW sample and control sample, we also consider THz emission from a bulk planar substrate of InAs for comparison.

Figure 5.5 shows linear autocorrelations and corresponding Fourier spectra obtained for InAs nanowires (top), bulk InAs (middle) and control (wetting layer, bottom) samples. Three important observations can be made from this. First of all, practically no THz is radiated from the control sample, which allows us to attribute the source of radiation to the nanowires.

The second observation concerns the linewidth of the emission. The fact that the quality factors ( $\nu/\Delta\nu_{FWHM}$ ) of both bulk InAs and InAs NW emission are nearly the same suggests the the source of the emission is the same.

To identify the excitation mechanism and the physical origin of the emission we take a look at some possible scenarios. As was discussed in Chpt. 4, photo-Dember current is one of the ultrafast mechanisms of carrier relaxation, which occurs after the absorption of the pump pulse in a bulk narrow-gap semiconductor. Cold carriers move to screen the resulting current and if the excitation bandwidth extends above the plasma frequency, plasma oscillations would commence. Another possible emission mechanism may occur at sufficiently high excitation where nonlinear mixing of disparate frequency components in the broad-band laser pulse results in parametric down-conversion into the far-infrared, i. e. optical rectification (OR).

To understand the origin of the NW emission, we study the pump fluence dependence of the THz from NWs. If the THz pulses originate from OR, the signals would increase quadratically with the excitation power. The inset of Fig. 5.6 shows the emitted power dependence is linear as the pumping level varies by over 2 orders of magnitude. This rules out any meaningful contribution from OR. We can also analyze the power-dependent emission spectrum. Radiation from the photo-Dember

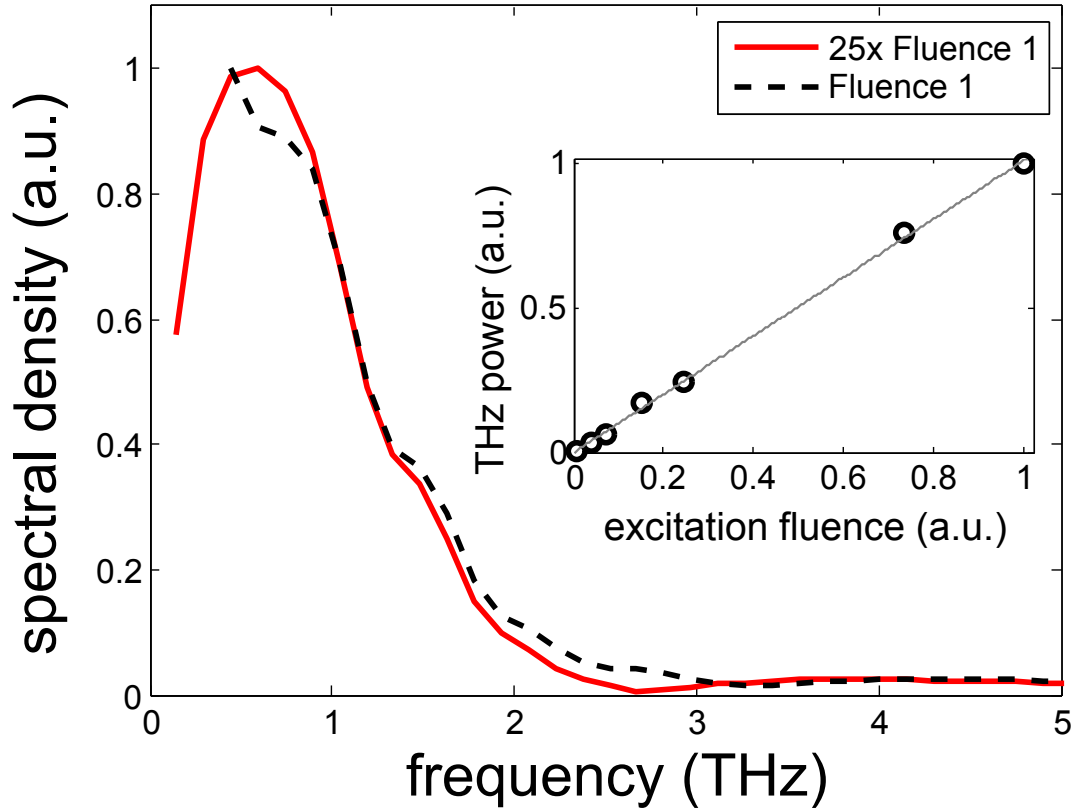


Figure 5.6: Power dependence of THz emission from InAs nanowires: normalized spectra of THz transients from InAs nanowires as the excitation laser power varies by a factor of 25. Absence of a spectral shift is consistent with radiation emanating from coherent plasma. Inset: THz power changes linearly as excitation fluence is varied over a range of 150.

current has a spectral bandwidth that exhibits slight blue-shifting with increase of excitation power, whereas a surface field transient will broaden [165]. The normalized NW radiation spectra display no appreciable blue-shift nor broadening when pump power is increased by 25 times (Fig. 5.6). However, because the spectrum is modulated by the plasmon mode (Chpt. 4), we cannot conclusively identify which ultrafast mechanism drives the emission. Recent experimental studies of THz emission from InN and Si nanorods of varying geometry indicated the dominant role of the photo-Dember excitation mechanism [175, 176]. While the starting mechanism

is still uncertain, an excitation-independent spectrum (Fig. 5.6) centered at  $\sim 1$  THz points to the motion of cold plasma as the primary source of the radiation signal from InAs nanowires. A possible Schottky barrier resulting from the presence of gold nanoparticles at the tips of nanowires has been shown to be negligible in InAs [177]. Even if significant barrier did exist, the associated depletion region would correspond to a very small fraction of the nanowire.

The third observation we can make is that the amplitude of the signal (at zero delay) obtained with the nanowires (Fig.5.5a, top) is only 2 times weaker than a slightly n-doped InAs substrate (Fig.5.5a, middle), despite the fact that the fill factor of the former (judging by the base size) is only  $f = (0.03 \pm 0.01)$ . This shows that nanowires are unusually good emitters of THz radiation, with the estimated radiation enhancement factor of  $0.5/f = 16 \pm 5$ , compared to the bulk InAs. This enhancement can be explained by the effective index of the nanowire waveguide, which is much smaller than the THz wavelength – resulting in no bound modes and all radiation in the leaky modes of the guide. Our numerical comparison of radiation outcoupling from the bulk ( $n=3.7$ , Fresnel included) and NW ( $n \approx 1$ ) predict a factor of 31 enhancement for the nanowires [178]. This is in reasonable agreement with observed enhancement of  $16 \pm 5$  considering the simplicity of our estimate [148]. The disparity in refractive index between bulk and NW can be verified versus the emission angle. We kept the excitation incidence at  $45^\circ$  and varied the angle of the detection with the bolometer by observing autocorrelation amplitude at zero delay between two probe beams. In this configuration, the collected solid angle by the bolometer is limited by the size of a Winston cone. Bolometer-sample distance is kept constant at all angles. The results are plotted in Fig. 5.7 along with the qualitative fits of the Hertzian dipole emitting from the bulk ( $n=3.7$ ) and NW ( $n \approx 1$ ) samples. We note that signals are normalized in both cases. Nanowires, unlike bulk exhibit weak signal for small detection angles. This is consistent with the lower index description. Bulk sample is clearly exhibiting the Brewster condition, for the p-polarized dipole

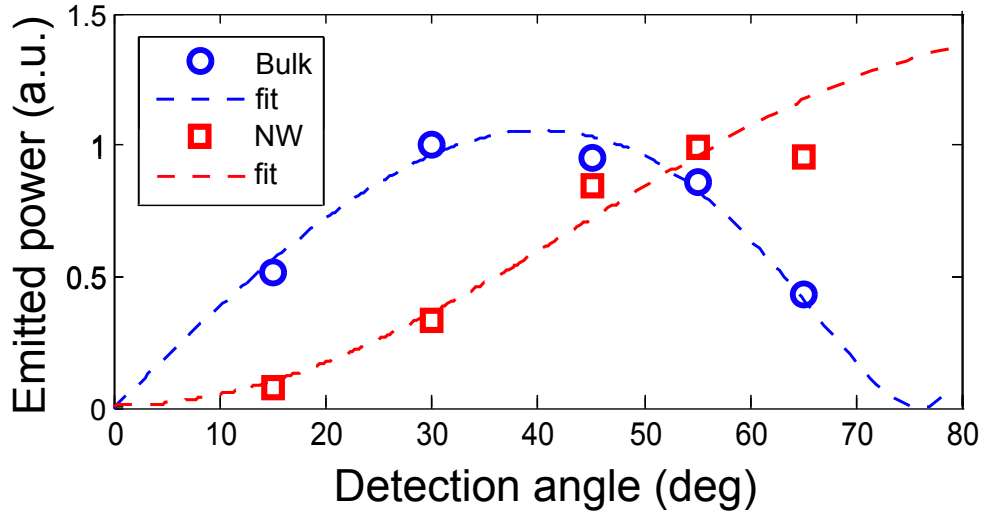


Figure 5.7: Bulk (blue, circles) and nanowire (red, squares) THz emission is plotted versus detection angle. Data at high incidence angles is not available due to the geometric constraints of the experiment. Fits represent qualitative curves for the p-polarized Hertzian dipole emission. Bulk was assumed to have  $n=3.7$ , NW  $n \approx 1$ .

emission. NW sample is exhibiting much smaller drop near the same angles. This serves as an indication that NW effective index is much lower than the bulk, leading to the enhanced radiation outcoupling. It should also be pointed out that similar THz enhancement was observed with InN nano-pillars with larger surface fill factor [175].

We analyze the lineshapes to extract carrier density from the plasmon emission (Chpt. 4). We first attempt to use classical Drude response [145] to analyze the spectra in Fig. 5.5b. The plasmon oscillates at frequency (Chpt. 4):

$$\omega = \sqrt{\omega_p^2 - \gamma^2/4}, \quad (5.6)$$

where  $\omega_p$  is the plasma frequency (Eqn. E.4) and  $\gamma$  is the damping rate (i. e. inverse momentum relaxation time) attributed mainly to electron-LO phonon scattering. Assuming an electron-donor ion plasma (i.e. neglecting holes), we estimate an electron density for the wire ensemble to be  $5 \times 10^{15} \text{ cm}^{-3}$  from the peak and broadening



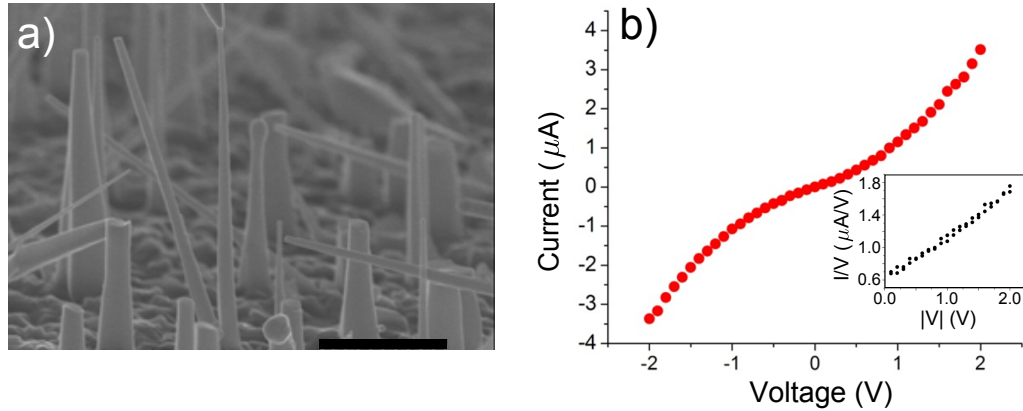


Figure 5.8: (a) SEM image of a tungsten STM tip in contact with one of the wires (middle top), with scale bar =  $1.5\mu\text{m}$ ; (b) Current versus voltage curve for an InAs nanowire, as measured on the contacted wire; inset plots  $I/V$  versus  $|V|$ , as determined from the I-V curve, this allows determination of the cross-over voltage  $V_c$ .

of the emission.

To test whether the bulk plasmon theory could explain our results, our collaborators at Sandia have independently obtained the carrier concentration by performing electronic transport measurements. This was accomplished by probing individual nanowires directly on the growth substrate inside of a SEM [179]. In this method, individual nanowires are contacted with a tungsten STM tip retrofitted inside of a SEM. A large area backside Ohmic contact completes the electrical circuit (Fig. 5.8). From the I-V measurements and some assumptions on the transport [180] the carrier density can be determined from:

$$N = \frac{\epsilon V_c}{eR^2} \quad (5.7)$$

where  $V_c$  is the cross-over voltage and  $R$  is the radius of the nanowire. Figure 5.8b depicts the current versus voltage measurement performed on the contacted NW. The cross-over voltage  $V_c$  is determined from the  $I/V$  versus  $|V|$  plot (Fig. 5.8b-inset) and is due to the pure Drude (conductivity) response. The nonlinearity in the I-V

curve is explained by the unscreened space-charge limited current for higher applied voltages [180]. The STM-probe measurements show that for an average radius of the nanowire  $\sim 150$  nm, the carrier concentration is  $\sim 2 \times 10^{17}$  cm $^{-3}$ . This measurement differs by nearly two orders of magnitude with the density estimate as determined by the bulk model (Eq. 5.6). This is not after all surprising, because in assuming bulk analysis we have completely ignored the presence of the NW boundary, i. e. the non-local nature of the modes.

In attempt to resolve this discrepancy, we consider a more realistic description of the longitudinal modes in the nanowire geometry. To that end, we consider the formalism of Pitarke *et.al.* who apply Poisson equation to solve for the inverse longitudinal dielectric function, with boundary conditions of an infinitely long cylinder along the z-axis, with radius  $R$  and dielectric constant  $\epsilon_\omega$  [181]:

$$\epsilon^{-1}(\mathbf{q}, \omega) = \frac{1}{\epsilon_0} - \left( \frac{1}{\epsilon_\omega^{-1}} - \epsilon_0^{-1} \right) \times \left\{ 1 + \frac{2}{\bar{Q}^2 + \bar{q}^2} \times \sum_{m=0}^{\infty} \frac{A(m, \bar{q}, \bar{Q})}{\epsilon_\infty \alpha_m(\bar{q}) - \epsilon_0} \right\} \quad (5.8)$$

where  $\epsilon_\omega = 1 - \omega_p^2/(\omega^2 + i\gamma\omega)$  and

$$\alpha_m(\bar{q}) = \frac{I'_m(\bar{q})K_m(\bar{q})}{I_m(\bar{q})K'_m(\bar{q})}. \quad (5.9)$$

The quantity  $A(m, \bar{q}, \bar{Q})$  given by:

$$A(m, \bar{q}, \bar{Q}) = \frac{\mu_m J_m(\bar{Q})}{I_m(\bar{q})K'_m} \times \left\{ \epsilon_\omega I'_m(\bar{q})f_m^{(1)} + \epsilon_0 K'_m(\bar{q})f_m^{(2)} \right\}. \quad (5.10)$$

Here,  $J_m$  is a Bessel function of the first kind,  $K_m, I_m$  are modified Bessel functions with prime denoting derivative with respect to the argument (e.g.  $I' = dI/d\bar{q}$ ). Terms  $\bar{q} = q_z R$  and  $\bar{Q} = QR$  are defined such that  $|\mathbf{q}|^2 = Q^2 + q_z^2$ . The quantities  $\mu_m$  are the Neumann numbers, such that  $\mu_m = 1$  for  $m = 0$  and  $\mu_m = 2$  for  $m \geq 1$ . Finally, the quantities  $f_m^{(1,2)}$  in Eq. 5.10 are given by:

$$f_m^{(1)} = \bar{q} J_m(\bar{Q}) K_{m-1}(\bar{q}) + \bar{Q} J_{m-1}(\bar{Q}) K_m(\bar{q}) \quad (5.11)$$

and

$$f_m^{(2)} = \bar{q} J_m(\bar{Q}) I_{m-1}(\bar{q}) - \bar{Q} J_{m-1}(\bar{Q}) I_m(\bar{q}) \quad (5.12)$$

respectively. Note that the longitudinal modes are defined by the poles of Eq. 5.8 (see Appx. E, Equation E.11). Upon inspection we note that the modes due to the cylindrical geometry (under summation over  $m$ ) are determined by the denominator of the fraction and hence by the quantity  $\alpha_m(\bar{q})$  (Eq. 5.9). In the case of damping, i.e.  $\omega \rightarrow \omega + i\Gamma$ , the relative amplitude of the modes is determined from Eq. 5.10. We note that this formalism was derived for the case of an infinite wire. In the case of a wire of length  $L$ , we introduce quantization of the  $q_z$  component of the total wavevector  $q$ , analogous to Eq. 5.3, such that [171]:

$$\bar{q}_l = \frac{\pi l R}{L} \quad (5.13)$$

where  $l$  is an odd integer (see Landau damping section). With this notation, the longitudinal modes are described by a set of  $(m, l)$  integers, where  $m$  is due to the cyclic continuity condition of the mode with respect to the azimuthal angle (as usual per cylindrical symmetry) and  $l$  is the quantization of the axial wavevector component of the mode. Figure 5.9a shows the dispersion relation of the longitudinal modes of the system, as determined by the denominator in Eq. 5.8 (as motivated above). The frequency axis is normalized with respect to the bulk plasmon frequency. Note that the dispersion curves are depicted as continuous but in fact are discrete as defined at each point allowed by  $\bar{q}_l$ . Continuous curves are equivalent to the limit when  $L \rightarrow \infty$ . The first  $m = 0$  mode exhibits acoustic dispersion for small  $\bar{q}$  and approaches the planar surface plasmon frequency  $\omega_{sp} = \omega_p/\sqrt{2}$  for  $\bar{q} \gg 1$ . Higher modes ( $m \geq 1$ ) are essentially dispersion-less around the  $\omega_{sp}$  frequency.

The radiation modes are obtained from Eq. 5.4, with  $n \rightarrow 1$  and dielectric function from Eq. 5.8. For  $\bar{Q} = 0$ , one can separate the integrals (as discussed in Chpt. 4). The only difference is that now in addition to the characteristic length scale associated with the beam size, we have another transverse scale, set by the diameter of the nanowire itself. Since the diameter is much smaller than the wavelength, this dimension results in broadband phase-matching, i. e. a Hertzian dipole emission from each NW. These contributions are summed over the size of the beam  $W$  to generate

an effective Airy function  $\mathcal{A}(k \sin \theta W/2)$ . This function is identical to the previously discussed cases (Landau damping) for the case when NW fill factor is large. For beam sizes covering only few nanowires, coherent modulation revealing low-order symmetries of few sampled wires might be present, subject to the diffractive low-frequency cut-off. We are not concerned with this case here however as we have over 500 NWs even for the case of smallest excitation spot sizes.

As in the case of Landau damping, phase-matching in the z-direction can not be satisfied as  $L < \lambda$ . Radiation out-coupling can still occur for:

$$\frac{\pi L \cos(\theta)}{\lambda} - l \frac{\pi}{2} = \mathbf{n} \frac{\pi}{2} \quad (5.14)$$

where  $\mathbf{n}$  is an odd integer. This condition is satisfied for odd  $l$  modes, as before.

We thus perform the numerical calculation of the emitted modes, using dielectric function Eq. 5.8 in radiation integral Eq. 5.4. Experimental results are plotted in Fig. 5.9b along with the calculation. To simulate a realistic scenario, we consider calculation for the first three axial modes of the NW ( $l = 1, 3, 5$ ) and we average over a flat distribution of the nanowire lengths ( $L = 5 - 20 \mu\text{m}$ ) and diameters ( $D = 100 - 300 \text{ nm}$ ). We also consider finite temporal bandwidth of the excitation by multiplying the calculated spectra with a corresponding Lorentzian lineshape (dashed blue line). There is a very good agreement between the peak and overall shape of the emission. For reference, Fig. 5.9b(inset) shows calculated emission from the first 3 axial modes of the NW.

From the calculation, the bulk plasma frequency is at 5 THz, which corresponds to carrier density of  $N = 2 \times 10^{17} \text{ cm}^{-3}$ . This carrier density is in a very good agreement with the transconductance measurements. We thus conclude that our experimental results and modeling indicate the presence of a low-energy acoustic surface plasmon mode in THz emission from InAs nanowires. Surface plasmon cavity modes in metallic nanowires have been recently observed using near-field microscopy [182] and optical loss spectroscopy [171]. Our data indicates that we observe radiation

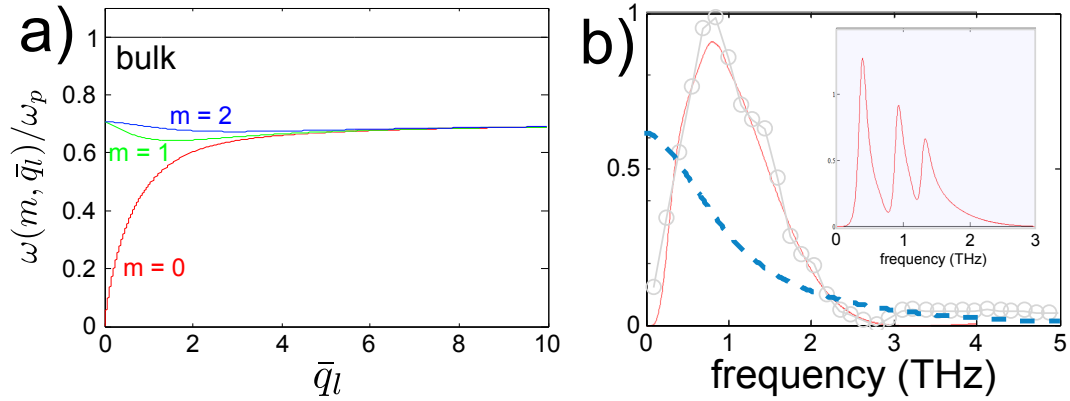


Figure 5.9: (a) Dispersion of the longitudinal bulk and surface plasmon modes; (b) Normalized measured emission spectrum of the InAs nanowire along with a qualitative fit (red), taking into account ensemble average; (inset) emission from single NW, showing  $l = 1, 3, 5$  modes

directly from the surface plasmon modes in the Hertzian dipole geometry. These results are corroborated by a recent observation of THz emission from Si nanowires, where the role of surface modes has also been discussed [176]. We also want to point out that we have investigated THz emission from high aspect ratio ( $L < 300$  nm,  $R \sim 30$  nm) nanowires [178]. We did not detect any measurable THz for the following plausible reasons: (i) a high aspect ratio  $R/L$  would blue-shift the  $m = 0$  mode out of the detection bandwidth; (ii) the resultant momentum mismatch is too large to be compensated by the lowest axial modes even in the Hertzian dipole approximation; (iii) strong Landau damping of plasmons is likely to exist in short wires, further reducing THz emission [178, 170]. The absence of THz from short nanowires is thus consistent with the explanation of acoustic surface plasmon modes offered above.

# Chapter 6

## Coherent control

### 6.1 Introduction

In Chapter 1 we mentioned that one of the attractive features of plasmonic research in semiconductors is the possibility of direct optical control of the collective mode excitations. We have demonstrated in Chapter 4 the possibility of shifting the plasma frequency on a picosecond time scale, under photo-Dember excitation mechanism. In fact, all of the excitation mechanisms we have considered so far depended only on the amplitude or square amplitude of the excitation beam. In this chapter we address the possibility of exciting longitudinal modes *coherently*, meaning the possibility of controlling the modes with the phase of the input beam.

Consider a semiconductor of bandgap  $E_g$  with an incident optical field of the form:

$$\mathbf{E}(t) = \mathbf{E}(\omega)e^{i(\omega t + \phi_1)} + \mathbf{E}(2\omega)e^{i(2\omega t + \phi_2)} + c.c. \quad (6.1)$$

If  $\omega > E_g/2$ , then either linear absorption ( $2\omega$ ) or two-photon ( $\omega$ ) absorption are possible, leading to generation of a photo-current (Chpt. 3.2). However the situation changes when both transitions happen simultaneously. Since both initial and final

states of these transitions are the same, this will lead to an interference. In this context, interference implies injection of the photoelectrons into the conduction band [8], resulting in the *current* of the form [183]:

$$\frac{d\mathbf{J}}{dt} = \nu^{(3)} \mathbf{E}(\omega) \mathbf{E}(\omega) \mathbf{E}^*(2\omega) e^{i\Delta\phi} + c.c. \quad (6.2)$$

where  $\nu^{(3)}$  is in general a frequency-dependent fourth-rank tensor and  $\Delta\phi = 2\phi_1 - \phi_2$ . Thus, by manipulating the mutual phase difference  $\Delta\phi$  and polarization states of the generating  $\omega$  and  $2\omega$  beams, we can coherently control the photocurrent vector, i. e. we have a process of *quantum-interference current control* (QUICC). This also means that we can in principle excite collective modes in a controlled manner. For the case of a planar semiconductor interface, the resultant wavevector of the collective mode would be parallel to the surface<sup>†</sup>, corresponding to a more preferential orientation for the radiation outcoupling (Chpt. 5.3). QUICC has been demonstrated in a number of semiconductors, mainly with  $\omega$  in the visible-NIR portion of EM spectrum [8]. Sheik-Bahae predicted QUICC current to scale with the electronic mobility and inversely with the bandgap energy – thus narrow-gap semiconductors are of particular interest. This fact served as a motivation for the work presented in Sect. 6.4.

The process of QUICC corresponds to the “real” manifestation of the  $\chi^3$  response (i.e.  $\nu^{(3)} \propto \Im\chi^{(3)}$ ), since it involves single and two-photon absorption events [8]. Khurgin has shown that the “virtual” equivalent of the QUICC process is the process of third-order optical rectification (TOR) [184, 185]:

$$E_{THz} \propto \chi^{(3)} E_\omega(t) E_\omega(t) E_{2\omega}^*(t) e^{i\Delta\phi} \quad (6.3)$$

where  $\chi^{(3)}$  is a real fourth-rank optical susceptibility tensor. Recently, intense THz emission has been demonstrated by the TOR process in air [186], with subsequent coherent control [187].

---

<sup>†</sup>photocurrent vector is in the plane of the polarization states of the input beams

In the first part of this chapter (Sect. 6.2) we present some experimental details relevant to the coherent control experiments and present two methods of controlling the mutual phase delay  $\Delta\phi$ . Following the experimental section, we provide demonstration of coherent control using third-order optical rectification in the air-breakdown plasmas [187] (Sect. 6.3). We conclude with some preliminary results concerning QUICC in bulk InAs substrates (Sect. 6.4).

## 6.2 Experimental details

The experimental setup for coherent control needs to have the following functionality:

- Generate  $2\omega$  beam and ensure temporal overlap between  $\omega$  and  $2\omega$ ;
- Control polarization states of  $\omega$  and  $2\omega$  beams independently;
- Control phase-delay between  $\omega$  and  $2\omega$  beams.

Hence, we need to modify the setup presented in Chpt. 3.4 to satisfy these criteria. To begin, we use a spherical silver mirror to focus fundamental ( $\omega$ ) pulses onto the target of interest (Fig. 6.1). To generate  $2\omega$  we use a Type-I  $\beta$ -BBO, cut at  $\theta = 29^\circ$  for doubling 800 nm light. In the case of high energy pulses (800 nm) we use the doubling crystal before the focusing mirror, while the OPA pulses (Sec. 2.2.5) are focused through the BBO onto a target. The thickness of BBO crystal is  $30\mu\text{m}$ , optically contacted to inactive fused-silica substrate of thickness 1 mm. A thin crystal ensures (i) broadband phase-matching is satisfied; (ii) existence of minimal temporal walk-off between the  $\omega$  and  $2\omega$  beams. During the experiments, BBO-layer is oriented toward the target. Type-I phase-matching condition results in a second harmonic output that is perpendicularly polarized to the fundamental beam. As was predicted by Sheik-Bahae, this is the least optimal polarization state for generation of QUICC in semiconductors [8]. Therefore, we consider the need for



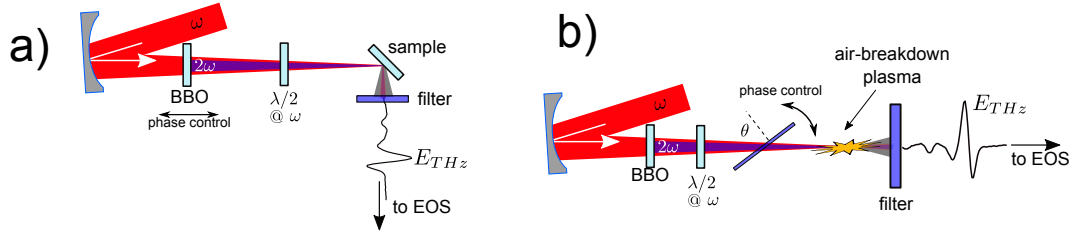


Figure 6.1: Experimental methods of coherent control: fundamental beam at  $\omega$  is focused onto a target: air (a) or semiconductor sample (b) through a second-harmonic crystal (BBO), generating  $2\omega$ . Polarization of the  $\omega$  is rotated with respect to  $2\omega$  beams by a true-zero order  $\lambda/2$  waveplate at  $\omega/2\pi c$  wavelength. Introducing an optical path difference between  $\omega$  and  $2\omega$  by either (a) moving BBO or (b) rotating a thin glass plate, the phase  $\Delta\phi$  can be varied. Phase-delay methods (a,b) and sample geometries (a,b) can be interchanged.

polarization control between the two beams. True-zero-order  $\lambda/2$  waveplate at 800 nm (AR coated at 400 nm and 800 nm, Newlight Photonics) allows for rotation of the polarization of the  $\omega$  beam with respect to the  $2\omega$  with minimal temporal walk-off (free-standing  $40\mu\text{m}$  thick). Up to now we have only introduced an optical train that minimizes temporal walk-off between the  $\omega$  and  $2\omega$  pulses as well as controls the relative polarization between the two beams. We should also point out that all reflective optics is used in order to avoid phase-front distortion of the pulse. For this reason silver mirrors deposited onto an optical substrate with at least  $\lambda/4$  surface quality are used (Thorlabs).

The main requirement for these experiments (see list above) is to introduce a variable time delay between the two beams, which translates into a direct control of the relative phase  $\Delta\phi$ . We employ two methods of controlling the phase-delay, both depicted in Fig. 6.1. In the first implementation we utilize dispersion of air, such that:

$$\Delta\phi = \frac{4\omega l}{c} (n_\omega - n_{2\omega}), \quad (6.4)$$

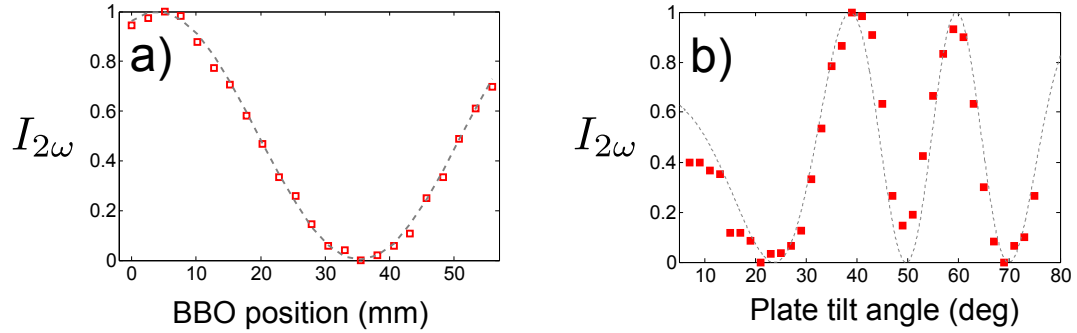


Figure 6.2: Experimental verification of coherent control via SHG interferometer. Phase-delay between  $\omega$  and  $2\omega$  is varied either by moving a BBO crystal (a) or tilting the fused-silica plate ( $92 \mu\text{m}$ ) thick (b). Here,  $\omega$  beam corresponds to  $\lambda = 800 \text{ nm}$ . Squares are experimental data, dashed gray lines correspond to fits as per Eq. 6.4 and Eq. 6.5 respectively.

where  $n$  is the refractive index of air, and  $l$  is the distance by which the the BBO crystal is moved and  $c$  is the speed of light. As a second method, we control the tilt angle of a thin fused-silica plate to introduce path-length difference between the beams [188]. In this case, taking into account angular dependence of the delay, we obtain:

$$\Delta\phi = \frac{4\omega l_p}{c} \left( \frac{n_p(\omega)}{\cos(\theta_\omega)} - \frac{n_p(2\omega)}{\cos(\theta_{2\omega})} - \sin\{\tan(\theta_\omega) - \tan(\theta_{2\omega})\} \right) \quad (6.5)$$

where  $n_p$  is the refractive index of the plate of thickness  $l_p$ . The angles  $\theta_{\omega,2\omega}$  are internal angles to the plate, which are related to tilt angle  $\theta$  (Fig. 6.1b) by the Snell's law:  $\sin(\theta) = n_s(\omega, 2\omega) \sin(\theta_{\omega,2\omega})$ .

We verify the ability to impose a coherent control in our experiment by using an interferometer between second-harmonic outputs, as per Chudinov *et. al.* [189]. In our implementation, this interferometer consists of two Type-I BBO crystals, with variable delay in between. The resultant intensity of the second harmonic  $I_{2\omega}$  experiences interference, such that:

$$I_{2\omega} = I_{2\omega}^{(1)} + I_{2\omega}^{(2)} + \sqrt{I_{2\omega}^{(1)} I_{2\omega}^{(2)}} \cos(\Delta\phi) \quad (6.6)$$

where  $I_{2\omega}^{(1,2)}$  are intensities of second harmonic after first and second BBO crystals, and  $\Delta\phi$  is given by either Eq. 6.4 (e. g. one of the BBO crystals is moved) or Eq. 6.5, when the delay plate is introduced in between the crystals. The result of the interference is depicted in Fig. 6.2. We note that both BBO position shift and delay-plate rotation generate interference, observed in second-harmonic output. We point out that the overall signal is more noisy from the delay-plate (Fig. 6.2b), as due to an optical surface defects of the thin optic. Furthermore, signal is especially noisy for angles less than  $\sim 15^\circ$ , due to contributions of reflections from the delay-plate into the balanced detection of the EOS setup. While the moving the BBO crystal is easier to implement, this method requires large Rayleigh range of the generating beam, otherwise position-dependent  $I_{2\omega}$  would complicate the data analysis. In the case of MIR pulses derived from the relatively weak OPA,  $2\omega$  beam has to be generated by focusing into the BBO, rendering delay-plate as the only method of  $\Delta\phi$  control in that situation.

### 6.3 Coherent control via third-order optical rectification

To test our experimental setup and verify that coherence is preserved in the THz detection, we focus 800 nm (2.5 mJ) and 400 nm (0.2 mJ) pulses in air (spot size  $\sim 100\mu\text{m}$ ). This process has been shown [186] to generate THz radiation by means of a third-order optical rectification (Eq. 6.3). This THz can also be coherently controlled [187]. Here, we change the  $\Delta\phi$  between the two beams by moving the BBO crystal and we use co-polarized case of  $\omega$  and  $2\omega$  beams. At each position of the BBO ( $\Delta\phi$ ) we detect  $E_{THz}$  as a function of the gate-pulse delay  $\tau$  (Chpt. 3.4), generated via the third-order optical rectification (TOR), thus obtaining  $E_{THz}(\Delta\phi, \tau)$ . At zero-delay ( $\tau = 0$ , Fig. 6.3a) clear modulation of the THz is observed as a function of the  $\Delta\phi$  (calibrated via Fig. 6.2). This interference is true for any delay of the gate

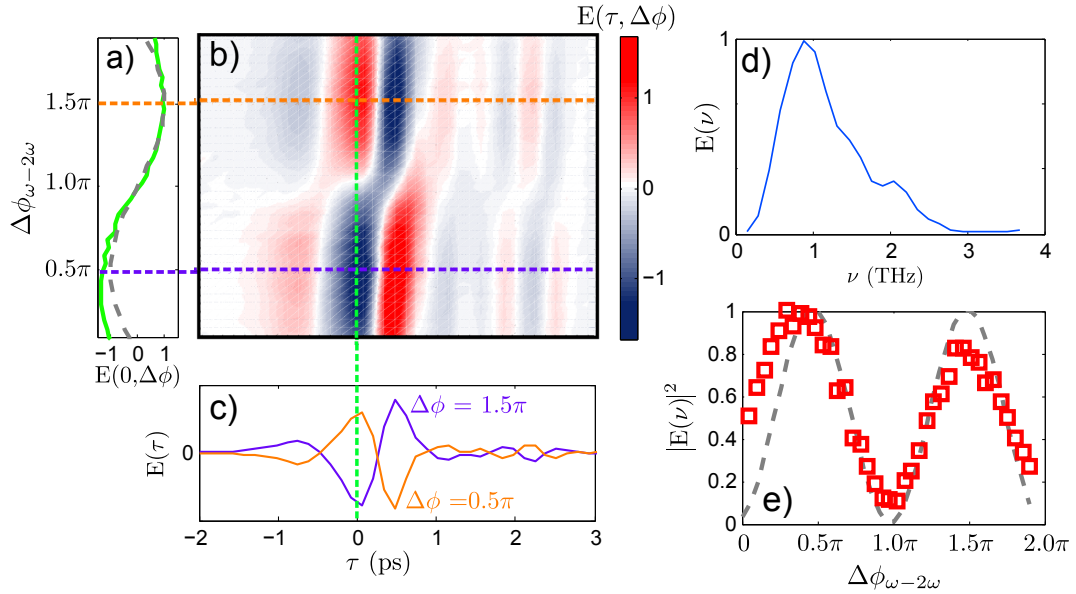


Figure 6.3: Coherent control of THz generated via  $\chi^{(3)}$  optical rectification in air-breakdown plasma. Surface plot of the  $E_{THz}(\Delta\phi)$  is shown in (b) along with cut at zero delay ( $E_{THz}(0, \Delta\phi)$ , a) showing interference fringes, as predicted by the theory (dashed gray line); in (c) two orthogonal (to (a)) cuts at  $E_{THz}(\tau, \pi/2)$  and  $E_{THz}(\tau, 3\pi/2)$  highlight nearly perfect out-of-phase behavior of the temporal traces; (d) displays Fourier transform of the time trace  $E_{THz}(\tau, \pi/2)$ , while (e) shows interference fringes as calculated from integration of  $|E(\nu)|^2$ , revealing nearly  $\sim 90\%$  of the full modulation depth, as per calculation (dashed gray line).

pulse  $\tau$  as can be evidenced from the contour plot of the  $E_{THz}(\Delta\phi, \tau)$  (Fig. 6.3b). By the virtue of the Parseval's theorem, the same modulation should be observed in the frequency domain, and is verified in Fig. 6.3e. Excellent visibility of fringes is a manifestation of the zero-background detection, as either  $\omega$  or  $2\omega$  produce negligible THz by themselves. Slight departure from the predicted modulation (dashed line) is explained by the total translation distance being comparable to the Rayleigh range of the fundamental beam.

The above experiment serves as a verification of excellent coherent control available in our experimental setup, i. e. mutual phase of the  $\omega$  and  $2\omega$  is preserved through multiple reflective optics.

Very recent experiments have demonstrated that polarization of the emitted THz field can be coherently controlled also [190, 191]. This physical insight can not be obtained from the simple  $\chi^{(3)}$  theory of optical rectification, however more detailed quantum mechanical calculations have been carried out [190] to verify the experimental observation and reveal the non-perturbative nature of the THz generation.

## 6.4 QUICC in InAs: preliminary results

In this section we briefly discuss some preliminary results in coherent control of the quantum-interference current (QUICC) in a narrow gap semiconductor InAs. As predicted by Sheik-Bahae [8], QUICC current should scale linearly with the electronic mobility. This motivates us to study narrow gap semiconductors, such as InAs. We perform our experiments at room temperature, such that  $E_g = 0.354eV$ , corresponding to  $3.5\mu\text{m}$ .

In these experiments, the fundamental pulse  $\omega$  is a signal pulse from the OPA ( $\lambda = 1.3\mu\text{m}$ ,  $300\mu\text{J}$ ,  $60\text{ fs}$ ). We collimate the pulses with the one-to-one reflecting telescope and subsequently focus them via a short ( $f = 5\text{ cm}$ ) spherical mirror onto the sample. The second harmonic is generated from a  $200\mu\text{m}$ -thick BBO crystal, placed in the middle of the telescope. At the sample plane, energies of the pulses are  $E_\omega \sim 200\mu\text{J}$  and  $E_{2\omega} \sim 15\mu\text{J}$ , with the excitation spot size  $\sim 150\mu\text{m}$ .

We note that in our case both pulse energies are above the bandgap. For the conventional QUICC, ( $\omega \sim E_g/2$ ), generated carrier distribution is spatially homogeneous (for the case when sample is much thinner than the Rayleigh range of the excitation). This implies that  $\omega$  beam would be unlikely to contribute to total THz emission in that case. Situation is contrasted to the case at point here, where we deal with above-gap excitation  $\omega > E_g$ . Here, large carrier gradient would result in a broadband photo-Dember current (Chpt. 4). Thus we expect the coherent signal

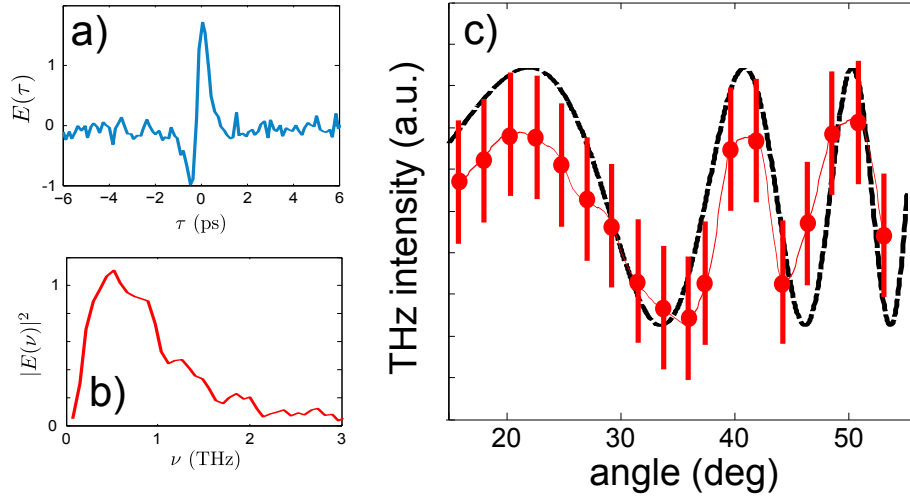


Figure 6.4: Preliminary results on coherent control in InAs: (a) time traces  $E(\tau)$  are analyzed by calculating  $|E(\nu)|^2$  (b) as a function of the delay plate angle. THz intensity with subtracted DC background is plotted in (c), along with the predicted modulation, as per Eq. 6.5.

to result in some modulation, superimposed with the DC offset which results from the incoherent sum of the  $\omega$  and  $2\omega$  THz emissions.

Preliminary results of QUICC control in InAs are shown in Fig. 6.4. THz waveforms are electro-optically sampled using 800 nm pulses, which are picked off by a 10% pellicle beam splitter before the parametric amplifier (Sec.3.4). Panel (a) shows a characteristic THz emission from InAs when excited by both  $\omega$  and  $2\omega$  beams. The resulting spectra  $|E(\nu)|$  are shown in Fig. 6.4b. We note that there is a factor of  $\sim 15$  increase in the amplitude noise of electro-optic signal when using OPA pulses. This noise can be decreased by a factor of 3 upon careful reduction of the aperture prior to supercontinuum generation for the parametric seed. This points to the fact that some of the amplitude instability is due to the nature of the nonlinear amplification in the OPA. Additional noise is expected to be due to the contributions from the room vibrations. Indeed, the optical path-length is nearly 5 meters before the point

where the OPA pulses are overlapped with the gating 800 nm pulse. Electro-optic sampling is extremely sensitive to room vibrations, due to the nature of balanced the detection.

The phase delay between  $\omega$  and  $2\omega$  beams is varied via angle-tuned fused-silica plate ( $l_d = 250\mu\text{m}$ ), as described in Section 6.2. To minimize effects of noise, traces are averaged for 10 minutes. Figure 6.4c shows the resulting integrated spectra as a function of plate tilt angle. Results of THz intensity versus the incidence are shown for angles larger than  $15^\circ$ , to avoid excess noise resulting from retro-reflections (Fig. 6.4c). Contributions from the above-gap excitation has been subtracted out. The resultant intensity shows modulation that corresponds to 4% depth of the total signal. This modulation is resolved with a signal to noise ratio of 2. We plot data against the expected modulation, as per Eq. 6.5. The results are in good agreement with the expected modulation. We should point out that no modulation is evident when the  $\lambda/2$  plate is removed. Current results are sub-optimal due to the fact that we use a  $\lambda/2$  plate designed for 800 nm. This means that we expect  $\sim \lambda/2$  rotation for the  $2\omega$  beam and  $\sim \lambda/4$  rotation for the  $\omega$  beam. As Sheik-Bahae predicted [8], no modulation should result from the cross-polarized excitation. In the current configuration we estimate that only half of the excitation is co-polarized, resulting in effective reduction of QUICC.

To our knowledge this is the first experimental attempt to detect QUICC for the above-bandgap excitation, especially in the narrow-gap semiconductors. No theoretical predictions exist for this regime either. In the subsequent experiments we want to verify these results and extend this study as a function of the excitation energy. Since QUICC is sensitive the band symmetries [8], by tuning the excitation energy we envision the ability to map out properties of the nearby electronic L- and X-valleys that lie within the spectral tuning range of the OPA.

# Chapter 7

## Concluding remarks

The best way to have a good idea is to have a lot of ideas.

---

Linus Pauling

### 7.1 Dissertation summary

In this dissertation we applied methods of ultrafast terahertz spectroscopy to study several aspects of semiconductor physics and in particular of collective mode excitations in semiconductors. The weak THz, emitted by the excited collective modes in semiconductor serves as a non-perturbative probe. We detect this radiation and analyze its characteristics to reveal the underlying dynamics of the emission process.

In order to accomplish sensitive THz detection system, we began this work with the development of a broadband stable femtosecond seed source for the regenerative amplifier. As an added flexibility in the choice of the excitation energy, we have designed, implemented and characterized an optical parametric amplifier (OPA) delivering 60 femtosecond tunable (1.1 - 3  $\mu\text{m}$ ) pulses with energies above 200  $\mu\text{J}$ . We



have implemented and characterized both coherent and incoherent THz detection schemes.

Using the developed experimental apparatus we have performed series of experiments, investigating the collective mode behavior and underlying physics in narrow gap semiconductors.

We began by performing temperature characterization of the plasma frequency in InSb. Detailed analysis revealed the importance of non-parabolicity correction in explaining the temperature dependence. We have extracted electronic mobility from the radiation signals and compared it to the published results. Due to the presence of additional scattering mechanisms, we determine the low-bound limit of the electronic mobility to be within 20-30% from the Hall measurements. Exhibited sensitivity to non-parabolicity and electronic mobility is especially interesting in studies of the transport properties in the nanostructures.

In the subsequent experiments we used a pump pulse to inject photo-carriers which upon cooling contributed to the background plasma density. We have demonstrated nearly 20% pump-induced shift of the plasmon frequency on an ultrafast time scale. Ultrafast all-optical control provides an interesting venue for exploring fundamental and practical applications of this control.

On the subject of control, we have also investigated coherent control of the electron dynamics using both virtual and real manifestations of the third-order nonlinear response in gases and condensed matter. Our preliminary experimental results indicate the ability to induce quantum-interference current control (QUICC) in InAs. This would be the first demonstration of this effect in the III-IV narrow gap semiconductors. What makes these observations more interesting is possibility of studying satellite valleys, as QUICC is sensitive to the overall symmetries of the bands.

We have also been concerned with the understanding of the radiation out-coupling mechanisms for the longitudinal collective modes. Analytical model of the radiation

fields from the longitudinal modes at various excitation conditions was discussed. We have performed experiments where we manipulate the plasmon modes in InSb to shift them into the regimes where non-local electron-electron interaction is enforced. Utilizing a plasmonic cavity we demonstrated the possibility of manipulating the plasmon wave into the dispersion region where individual particle excitations are allowed. As a result of these excitations, the collective mode was observed to be damped. The measured features of the Landau damping are in good agreement with the predictions made within the random-phase approximation. This demonstration is a first systematic mapping of the Landau damping in a solid-state system.

Building on results of the Landau damping experiment, we have invoked plasmon confinement in all three dimensions via a nanowire geometry. We demonstrated enhanced THz emission from InAs nanowires as compared to bulk InAs crystal. We attribute this enhancement due to highly leaky modes of the waveguide and provide some experimental measurements that support this view. Using existing dielectric function analysis of the cylindrical cavity geometry with our analytic radiation coupling model we numerically predict the emission spectrum of the nanowires and obtain a good match with the measurement. The analysis points to several key features of the plasmon confinement. The main result is the prediction and experimental verification of the radiation emitted by the low-energy acoustic surface plasmon mode. This observation allows us to infer the carrier density in the nanowires, which is in a good agreement with the independent transport measurements of our collaborators.

## 7.2 Future outlook

Investigations of this dissertation were concerned with the spectroscopy and control of the collective mode excitations in condensed matter systems. As was motivated in the Introduction chapter, one of the features that semiconductor/THz spectroscopy platform offers is the possibility of a near-field control. For instance, near-field studies

would allow investigation of single nanowires to be carried out, directly accessing dispersive plasmon modes on an ultrafast time scale. Author envisions to apply demonstrated ideas of this work to the near-field ultrafast terahertz spectroscopy. Localized probe of the femtosecond dynamics would provide fascinating access to the “microscopic” properties of the elementary excitations of condensed matter.

# Appendices

## Appendix A

# Transverse Hermite-Gaussian modes of a laser cavity

The paraxial solution of the Helmholtz equation is Gaussian beam of the form:

$$E(r, z) = E_0 A_{m,n} \frac{w_0}{w(z)} e^{-r^2/w^2(z)} \exp \left( -i \left[ kz - (1 + n + m) \operatorname{atan} \frac{z}{z_0} + \frac{kr^2}{2R(z)} \right] \right) \quad (\text{A.1})$$

where  $w_0$  is the minimum beam radius, such that  $w(z)$  is:

$$w(z) = w_0 \sqrt{1 + \left( \frac{z}{z_0} \right)^2}, \quad (\text{A.2})$$

where Rayleigh range  $z_0$  is:

$$z_0 = \frac{n\pi w_0^2}{\lambda}. \quad (\text{A.3})$$

Radius of curvature of the Gaussian beam  $R(z)$  evolves according to:

$$R(z) = z \left[ 1 + \left( \frac{z_0}{z} \right)^2 \right]. \quad (\text{A.4})$$

The quantity  $A_{m,n}$  describes amplitude of the Hermite-Gaussian modes and defined as:

$$A_{m,n} = H_n \left( \sqrt{2} \frac{x}{w(z)} \right) H_m \left( \sqrt{2} \frac{y}{w(z)} \right) \quad (\text{A.5})$$

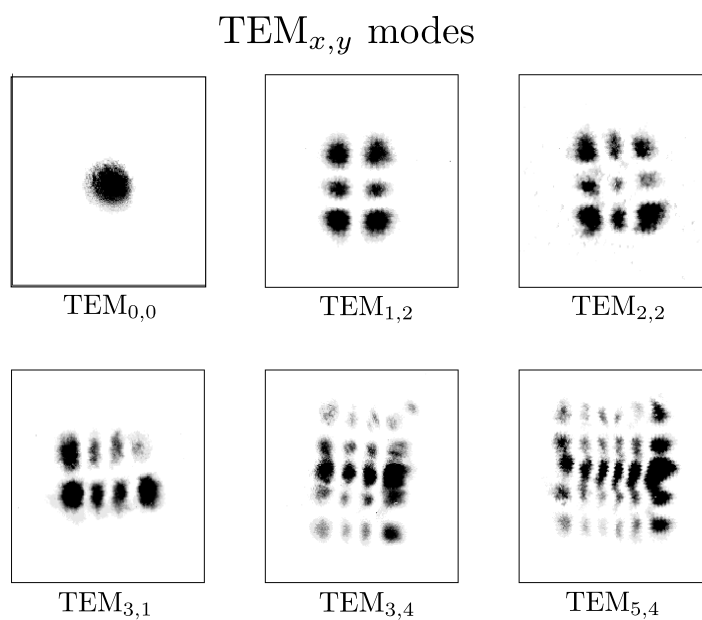
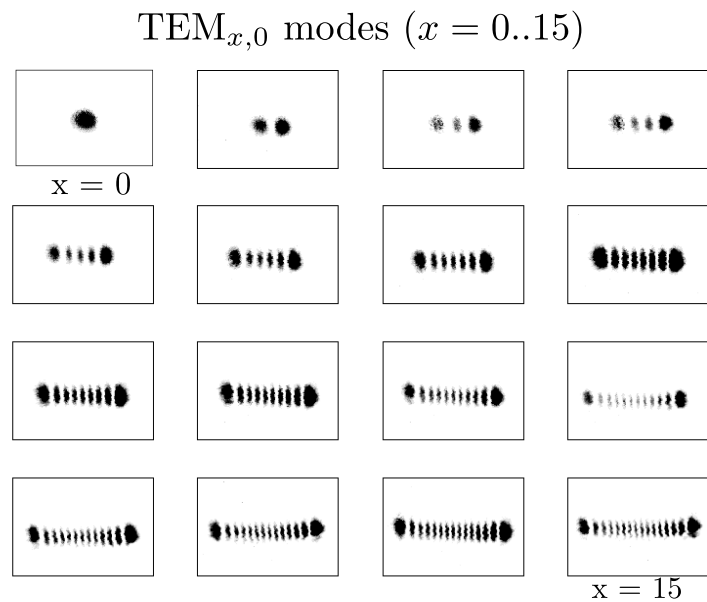


Figure A.1: Transverse Hermite-Gaussian modes of the Ti:Sa laser cavity: (top) TEM<sub>*x*,0</sub> horizontal modes, with  $x$  from 0 to 15; (bottom) Various TEM<sub>*x*,*y*</sub> modes.

where  $H_k$  is a Hermite polynomial of order  $k$  [192], Fig. A.1.

## Appendix B

# Propagation of a Gaussian pulse in a linear-response medium

Consider a Gaussian pulse in the time domain:

$$E(t) = \mathcal{E}_0 e^{i(\omega_0 t + \phi(t))} e^{-\frac{t^2}{\tau^2}} \quad (\text{B.1})$$

where  $\mathcal{E}_0$  is a peak amplitude of the pulse,  $\omega_0$  is the carrier frequency,  $\phi(t)$  is time-varying phase. We keep in mind that the real quantity of electric field is obtained by taking one half of the real part of  $E(t)$  (Eq. B.1). The quantity  $\tau$  is a broadening that defines pulse width  $\tau_p$  at FWHM of the intensity  $I(t) = E(t)E^*(t)$  as:

$$\tau_p = \sqrt{2\ln 2} \tau. \quad (\text{B.2})$$

We are going to be considering frequency domain in a moment, and hence taking the Fourier transforms. Let us first note that electric field of the pulse in Eq. B.1 is of the form  $F(t)\exp(i\omega_0 t)$ , where  $F(t)$  is in general complex function and  $\exp(i\omega_0 t)$  is a phasor. Obtaining Fourier transform of such function yields

$$\mathcal{F}[e^{i\omega_0 t} F(t)] = \int_{-\infty}^{\infty} e^{i(\omega_0 - \omega)t} F(t) dt = \hat{F}(\omega_0 - \omega) \quad (\text{B.3})$$

where  $\hat{F}$  is the Fourier transform  $\mathcal{F}[\ ]$  of the function  $F(t)$ . The property of the Fourier transform is to shift the frequency variable by a constant  $\omega_0$ , thus we can drop the phasor term in time description of the pulse (Eq. B.1) as long as we agree on the new frequency variable  $\Omega = \omega_0 - \omega$ , which represents detuning from the carrier frequency of the pulse.

Taking the Fourier transform of Eq. B.1 for a case of time-independent phase ( $\phi(t) = 0$ ) we obtain

$$E(\Omega) = \sqrt{\pi\tau}e^{-\frac{\Omega^2\tau^2}{4}}. \quad (\text{B.4})$$

The physical observable is the spectral density  $S(\Omega) = E(\Omega)E^*(\Omega)$  and therefore the FWHM  $\Delta\Omega$  is

$$\Delta\Omega = \frac{\sqrt{8\ln 2}}{\tau}. \quad (\text{B.5})$$

The widths in time and frequency domains are related. Considering Eq. B.2 and Eq. B.5 the product is

$$\Delta\nu\tau_p = \frac{\Delta\Omega}{2\pi}\tau_p = \frac{2\ln 2}{\pi} \approx 0.44. \quad (\text{B.6})$$

This is a manifestation of the uncertainty principle. Physically this means that given spectral content of the pulse defines minimum pulse duration  $\tau_p$ . A useful approximate relation to calculate minimum pulse width at a wavelength of 800 nm is:

$$\tau_p \approx \frac{0.94}{\Delta\lambda_0} \text{fs} \quad (\text{B.7})$$

if  $\Delta\lambda_0$  is in micrometers. For example, consider a pulse with a Gaussian spectrum with FWHM of 15 THz ( $\Delta\lambda = 32$  nm) at the center frequency of 375 THz (800 nm). The minimum pulse width is 29 fs (Eq. B.6), or 11 optical cycles. The relation (Eq. B.1) being independent of the spatial coordinate is only true in vacuum<sup>1</sup>, where  $n(\omega) = 1$ . The linear vacuum is uneventful.

---

<sup>1</sup>For intensities below pair-creation in quantum vacuum



As we will see below, upon interaction with matter the phase  $\phi(t)$  becomes non-constant and with  $\tau_p$  acquires dependence on the propagation distance. So in general for Gaussian pulses Eq. B.6 becomes

$$\Delta\nu\tau_p \geq 0.44 \quad (\text{B.8})$$

Light-matter interaction depends on many parameters, but in general it is not instantaneous. By non-instantaneous we mean that there is a finite time over which pulse interacts with a medium. If this time is much shorter than the  $1/\omega_0$ , i.e. a duration of the single cycle of light, only then we can speak of instantaneity as a very good approximation for coherent interaction.

The frequency domain picture is that upon propagation through a medium a polychromatic pulse will experience varying refractive index for different spectral components of the pulse. This effect, called *dispersion* is just another manifestation of non-instantaneous action of the pulse. Let us now analyze what is the effect that propagation through dielectric medium has on the pulse. To avoid convolution integrals in the time domain it is more natural to treat the effect of linear response as multiplication in the frequency domain.

Assuming plane wave propagation in the  $z$ -direction, the wave equation is [107]

$$\left( \frac{\partial^2}{\partial z^2} - \frac{1}{c^2} \frac{\partial^2}{\partial t^2} \right) E(z, t) = \mu_0 \frac{\partial^2}{\partial t^2} P(z, t), \quad (\text{B.9})$$

where  $c$  is speed of light,  $\mu_0$  is magnetic permeability of the free space and  $P(z, t)$  is the polarization of the medium induced by the action of the pulse. Non-instantaneous but linear and lossless (no absorption or gain) response of the medium is manifested in the frequency domain as [107]

$$P(z, \Omega) = \epsilon_0 \chi(\Omega) E(z, \Omega), \quad (\text{B.10})$$

where  $\chi$  is the frequency dependent dielectric susceptibility. To see how such response affects the pulse we transform in into a more convenient frequency domain. Using

Eq. B.10, the Fourier transform of the wave equation (Eq. B.9) is now:

$$\left[ \frac{\partial^2}{\partial z^2} + \Omega^2 \epsilon(\Omega) \mu_0 \right] E(z, \Omega) = 0, \quad (\text{B.11})$$

where

$$\epsilon(\Omega) = \epsilon_0 [1 + \chi(\Omega)] \quad (\text{B.12})$$

is the total dielectric constant. The general solution is a plane wave, propagating in the  $z$ -direction, i.e.

$$E(z, \Omega) = E(0, \Omega) e^{-ik(\Omega)z}, \quad (\text{B.13})$$

where  $E(0, \Omega)$  is known spectral amplitude of the pulse at the position  $z = 0$ , while  $k(\Omega)$  is a frequency-dependent wavevector which is given by

$$k(\Omega) = \Omega \sqrt{\epsilon(\Omega) \mu_0} = \frac{\Omega}{c} n(\Omega), \quad (\text{B.14})$$

with  $n(\Omega)$  being the refractive index of the medium. To quantify variation of the  $k(\Omega)$  over the range centered at the pulse carrier frequency we approximate index dependence by performing Taylor expansion up to the second order about  $\omega_0$ :

$$k(\Omega) = k(\omega_0) + \left. \frac{dk}{d\Omega} \right|_{\omega_0} (\Omega - \omega_0) + \frac{1}{2} \left. \frac{d^2k}{d\Omega^2} \right|_{\omega_0} (\Omega - \omega_0)^2 \quad (\text{B.15})$$

We are in the position to transform back into the time domain and analyze how various orders of  $n(\Omega)$  approximation affect the pulse. Taking inverse Fourier transform of  $E(\Omega)$  (Eq. B.13) while retaining only up to the linear term of the  $k(\Omega)$  expansion:

$$E(z, t) = \frac{1}{2\pi} e^{-ik_0 z} \int_{-\infty}^{\infty} E(0, \Omega) e^{-ik'_0(\Omega - \omega_0)z} e^{i\Omega t} d\Omega \quad (\text{B.16})$$

$$\Omega' = \Omega - \omega_0, \quad (\text{substituting})$$

$$E(z, t) = \frac{1}{2} e^{i(\omega_0 t - k_0 z)} \int_{-\infty}^{\infty} E(0, \Omega' + \omega_0) e^{i\Omega' (t - k'_0 z)} d\Omega' \quad (\text{B.17})$$

$$(\text{B.18})$$

where  $k_0 = k(\omega_0)$  and  $k'_0$  is the first derivative of  $k(\Omega)$  with respect to  $\Omega$  evaluated at  $\omega_0$  (Eq. B.15). Equation B.17 is just an inverse Fourier transform with the new time variable  $t'$  given by:

$$t' = t - \left. \frac{dk}{d\Omega} \right|_{\omega_0} \quad z = t - \frac{z}{v_g}, \quad (\text{B.19})$$

where  $v_g$  stands for the group velocity - velocity with which pulse envelope moves. We see that approximating frequency dependence of the wavevector  $k$  up to the first order results in no pulse shape change. The only consequence of such linear dispersion is that the pulse envelope is ensured to move at the group velocity  $v_g$ . Since  $k'_0 = 1/v_g$ , the  $k''_0$  represents group velocity dispersion or GVD. While the effect of GVD on the pulse can be considered in general terms [24], here we apply it to the example of a Gaussian pulse (Eq. B.1).

The GVD term contributes quadratic phase to the pulse in the frequency domain (Eq. B.4):

$$E(z, \Omega) = E(\Omega, 0) e^{-ik_0 z} e^{-ik'_0(\Omega - \omega_0)z} e^{-\frac{\Omega^2 \tau^2}{4} [1 + 2ik''_0 z / \tau^2]}. \quad (\text{B.20})$$

Since the effect of linear dispersion was shown to shift time into the coordinate system moving at group velocity (Eq. B.19), we lump this and propagator  $\exp(-ik_0 z)$  all into the term  $E'_\Omega$  to separate effect of GVD. Transforming back into the time domain (inverse of the Eq. B.1  $\rightarrow$  Eq. B.4) we obtain

$$E(z, t) = E'_t \exp \left[ -\frac{t^2}{\tau^2} \frac{1}{1 + 2ik''_0 z / \tau^2} \right], \quad (\text{B.21})$$

where  $E'_t$  is the time domain equivalent of  $E'_\Omega$ . Identifying length scaling parameter

$$l_d = \frac{\tau^2}{2k''_0}, \quad (\text{B.22})$$

equation B.21 can be simplified to

$$E(z, t) = E'_t \exp \left[ -\frac{t^2}{\tau^2 [1 + (z/l_d)^2]} (1 - iz/l_d) \right] \quad (\text{B.23})$$

Pulse duration is given by the FWHM of the  $I(t)$  and therefore

$$\tau_p = \sqrt{2\ln 2} \tau \sqrt{1 + \frac{z^2}{l_d^2}}. \quad (\text{B.24})$$

Pulse duration is no longer a constant as in the case of propagation in vacuum. As a result of non-zero  $k_0''$ , pulse envelope in the time domain experiences broadening that is dependent on the spatial coordinate. The length scale associated with this broadening is parametrized by the dispersive length  $l_d$  (Eq. B.22). For propagation distance  $z \ll l_d$  effects of the broadening can be ignored and vacuum-like pulse description applies. For  $z = l_d$ , pulse duration increases by  $\sqrt{2}$ . For  $z \gg l_d$  the relation B.24 asymptotes to  $\sqrt{2\ln 2} z/l_d$ .

The description of pulse duration (Eq. B.24) broadening has an analogy for the Gaussian beams as eigenmode solutions to the far-field diffraction. In such case

$$w(z) = w_0 \sqrt{1 + \frac{z^2}{z_0^2}} \quad (\text{B.25})$$

where  $w(z)$  is the spatial extent of the beam in transverse direction to the propagation, while  $z_0 = \pi w_0^2/\lambda$  with  $\lambda$  being the free-space wavelength of the beam (see for instance Verdeyen [192]). The beam waist  $w(z)$  is minimum at  $w_0$  and otherwise diverges. There is also a position dependent radius of curvature of the phase-front of a Gaussian beam that is uniquely specified by the value of  $z_0$  [192]. In this analogy, minimum pulse width  $\tau_p$  (Eq. B.2) determined by the spectral content of the pulse  $\Delta\Omega$  (Eq. B.5) only occurs for unique position (here  $z=0$ ) and increases otherwise with the speed controlled by the value of  $l_d$ . Pulse envelope broadening is also accompanied by the position-dependent phase modulation (Eq. B.23):

$$\omega_t = \omega_0 + \frac{z}{\tau_p^2 l_d} t, \quad (\text{B.26})$$

where  $\tau_p$  is given by Eq. B.24. The observed linear change of instantaneous frequency  $\omega_t$  with time is known as pulse *chirp*. Pulse chirp is akin to the radius of curvature of the spatial Gaussian beam, both are uniquely determined by the broadening of

the real part (envelope) such that the frequency (spatial or temporal) content is unchanged. In particular, Eq. B.26 shows a linear sweep in frequencies corresponding to broadening in the frequency domain, however such broadening is precisely canceled by the pulse envelope broadening in the time domain. After all, we have chosen a case of a linear response and therefore spectral content of the pulse has to be unchanged upon propagation. Chirped pulse cannot be produced without accompanying pulse envelope broadening in the medium described by the linear response. However, by inducing nonlinear response it is possible to produce chirp without corresponding pulse broadening, as in the effect of *self-phase modulation* (SPM, Chpt. C). The action of SPM will lead to broadening of the frequency content, leading to possibility of shorter pulse. This is completely analogous to the action of the lens on a spatial Gaussian pulse and hence sometimes is called *temporal lens* [24].

Finally, minimum of the time-bandwidth product (Eq. B.6) can be formed

$$\Delta\Omega\tau_p = \frac{2\ln 2}{\pi} \sqrt{1 + \frac{z^2}{l_d^2}} \quad (\text{B.27})$$

where the action of GVD is seen to increase pulse duration for the linear response of the medium.

# Appendix C

## Velocity matching condition

In this appendix we briefly discuss derivation of velocity matching condition for optical rectification. Consider an optical pulse of intensity envelope  $I(t)$ , propagating in a  $z$  direction through a material of thickness  $L$  with the  $\chi^2$  response (Fig. C.1). The induced second order polarization associated with the optical rectification is (Eq. 3.11):

$$\mathbf{P}_{OR}^{(2)} = \chi_{OR}^{(2)} I(t) \hat{\mathbf{p}}. \quad (\text{C.1})$$

where  $\hat{\mathbf{p}}$  is a unit vector in the direction of the polarization, as determined by tensor properties of  $\chi^2$  (Appx. C). From Eqn. D.14 (with the *polarization current*:  $J(\omega) = -i\omega P(\omega)$ ), the radiated field at a point  $\mathbf{r}$  in space becomes:

$$E(\mathbf{r}, \omega) = -\frac{\omega^2}{c^2} \frac{e^{ikr}}{r} I(\omega) \hat{\mathbf{k}} \times \hat{\mathbf{k}} \times \hat{\mathbf{p}} \int e^{-i(\mathbf{k} \cdot \mathbf{r}_s + \omega z/v_g)} d^3 r_s. \quad (\text{C.2})$$

Here, vector  $\mathbf{r}_s$  runs over the spatial extent of the polarization current (Fig. C.1). Time has been shifted (Eq. B.17) into the frame of reference which is propagating with the group velocity  $v_g$  of the pulse (Eq. B.19). The Eq. C.2 can be re-written:

$$\mathbf{E}(\mathbf{r}, \omega) = -\omega^2 E_0 \hat{\mathbf{E}} \int_0^L e^{-i\omega z/c[n(\omega) \cos(\theta) - n_g]} dz \int e^{-i\mathbf{k}_\perp \cdot \mathbf{r}_{s\perp}} d^2 r_{s\perp} \quad (\text{C.3})$$

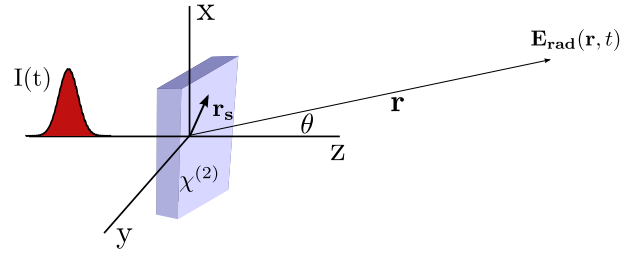


Figure C.1: Schematic diagram of the situation as described in the text below. Optical pulse propagates through a nonlinear medium with a  $\chi^{(2)}$  response (blue), inducing a nonlinear polarization current. This current radiates  $\mathbf{E}(\mathbf{r}, t)$  field.

where the first integral is along the direction of the propagation and is responsible for the *phase-matching*. The second is a *diffraction* integral in the plane perpendicular to  $z$ , with the appropriate components in the dot product, e.g.  $\mathbf{k}_\perp = \mathbf{k} - k\hat{\mathbf{z}}$ .

The solution to the phase-matching integral is a *sinc* function:

$$\int_0^L e^{-i\Delta kz} dz = L e^{-i\Delta kL/2} \text{sinc}(\Delta kL/2), \quad (\text{C.4})$$

where:

$$\Delta k = \omega/c[n(\omega) \cos(\theta) - n_g]. \quad (\text{C.5})$$

The phase-matching bandwidth is identified by the first zero of the *sinc* function and is referred to as *coherence length*.

# Appendix D

## Far-field radiation

In this Appendix a radiation from the electric dipole is derived in the far-field approximation. This is accomplished by solving Maxwell's equations, which is a set of four first order differential equations. It is often more convenient to introduce potentials, obtaining a smaller number of the second-order differential equations [107]. Two coupled second-order differential equations for a scalar  $\Phi$  and a vector  $\mathbf{A}$  potentials are equivalent to the Maxwell's equations in a vacuum<sup>1</sup>:

$$\nabla^2\Phi + \frac{\partial}{\partial t}(\nabla \cdot \mathbf{A}) = -\frac{\rho}{\epsilon_0} \quad (\text{D.1})$$

$$\nabla^2\mathbf{A} - \frac{1}{c^2}\frac{\partial^2\mathbf{A}}{\partial t^2} - \nabla\left(\nabla \cdot \mathbf{A} + \frac{1}{c^2}\frac{\partial\Phi}{\partial t}\right) = \mu_0\mathbf{J} \quad (\text{D.2})$$

The only physical observables are the electric and magnetic fields, which are defined through the potentials as:

$$\mu_0\mathbf{H} = \nabla \times \mathbf{A} \quad (\text{D.3})$$

---

<sup>1</sup>most of this Appendix chapter follows J.D.Jackson's Classical Electrodynamics [107] and lecture notes from *Laser Physics II* course taught by Prof. Sheik-Bahae (UNM, Fall 2006)



and

$$\mathbf{E} = -\nabla\Phi - \frac{\partial\mathbf{A}}{\partial t}. \quad (\text{D.4})$$

This means that the potentials are unique only up to an additive term which obeys equations D.3 and D.4, such as to leave the fields unchanged (*gauge invariant*). If chosen properly, the additive term can lead to uncoupling of Eq. D.1 and Eq. D.2. Different choices of this shift allow for different *gauges*, leading to some simplifications of the particular problem at hand.

## D.1 Lorentz gauge

This gauge is defined by the Lorentz condition:

$$\nabla \cdot \mathbf{A} + \frac{1}{c^2} \frac{\partial\Phi}{\partial t} = 0, \quad (\text{D.5})$$

which uncouples Eq. D.1 and Eq. D.2 to generate two second order inhomogeneous differential equations for both potentials:

$$\left( \nabla^2 - \frac{1}{c^2} \frac{\partial^2}{\partial t^2} \right) \Phi = -\frac{\rho}{\epsilon_0} \quad (\text{D.6})$$

and

$$\left( \nabla^2 - \frac{1}{c^2} \frac{\partial^2}{\partial t^2} \right) \mathbf{A} = -\mu_0 \mathbf{J} \quad (\text{D.7})$$

where  $c$  is the speed of light. The fact that both potentials are determined from their respective wave equations naturally satisfies causality in the Lorentz gauge.

In the frequency domain, Eq. D.7 transforms into an inhomogeneous Helmholtz wave equation:

$$(\nabla^2 + k^2) \mathbf{A}(\mathbf{r}, \omega) = -\mu_0 \mathbf{J}(\mathbf{r}, \omega) \quad (\text{D.8})$$

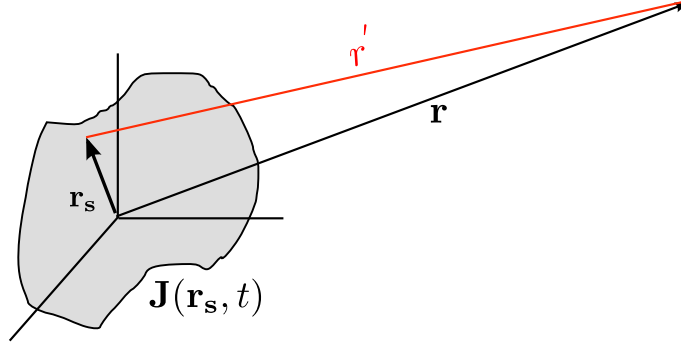


Figure D.1: Diagram represents the radiation field at a point  $\mathbf{r}$  which is calculated by integrating over all possible contributions from the current distribution  $\mathbf{J}(\mathbf{r}_s, t)$ . The distance  $r'$  (red) is relevant for calculation of the Green function for a point source excitation (see text).

where  $k = \omega/c$  is the magnitude of the wavevector. The Green function of Eq. D.8 satisfies:

$$(\nabla^2 + k^2) G_k(\mathbf{r}, \mathbf{r}_s) = -\mu_0 \delta(\mathbf{r} - \mathbf{r}_s) \quad (\text{D.9})$$

for a point source located at  $\mathbf{r}_s$ . In an isotropic homogeneous medium the spherical symmetry dictates that  $G_k$  can only be a function of  $r' = |\mathbf{r}'| = |\mathbf{r} - \mathbf{r}_s|$  (see Fig. D.1). It can be shown that:

$$G_k(r') = M \frac{e^{ikr'}}{r'} + (1 - M) \frac{e^{-ikr'}}{r'} \quad (\text{D.10})$$

where  $M$  depends on the choice of the boundary conditions. For instance, for a source switched on at time  $t = 0$ , only the outgoing wave ( $M = 1$ ) is relevant. The incoming wave described by the  $\exp(-ikr')$  is needed to satisfy causality for an arbitrary choice of the initial conditions.

The vector potential in Eq. D.8 is now determined by the convolution of the point-source Green function (Eq. D.10,  $M = 1$ ) with the spatially-extended current source (Fig. D.1):

$$\mathbf{A}(\mathbf{r}, \omega) = \frac{\mu_0}{4\pi} \int \frac{e^{ik|\mathbf{r}'|}}{|\mathbf{r}'|} \mathbf{J}(\mathbf{r}_s, \omega) d^3 r_s. \quad (\text{D.11})$$

This is the exact solution for the vector potential in the frequency domain while in the Lorentz gauge in the absence of boundaries. Next, we consider some relevant simplifications.

## D.2 Far-field approximation

In the *far-field*, i.e. when  $(k|\mathbf{r}| \gg 1)$ , the denominator of Eq. D.11 is approximated by:

$$\mathbf{r}' = |\mathbf{r} - \mathbf{r}_s| \simeq r - \mathbf{r}_s \cdot \hat{\mathbf{r}} \quad (\text{D.12})$$

where  $\hat{\mathbf{r}} = \mathbf{r}/r$  is a unit vector in the direction of the observation. With this approximation, Eq. D.11 is simplified to:

$$\mathbf{A}(\mathbf{r}, \omega) = \frac{\mu_0}{4\pi} \frac{e^{ikr}}{r} \int e^{-i\mathbf{k} \cdot \mathbf{r}_s} \mathbf{J}(\mathbf{r}_s, \omega) d^3r_s, \quad (\text{D.13})$$

where  $\mathbf{k} = k\hat{\mathbf{r}}$ . Using Eq. D.13 in Eq. D.3 together with Faraday's law ( $\epsilon_0\omega\mathbf{E} = i\nabla \times \mathbf{H}$ ), the electric field is determined by:

$$\mathbf{E}(\mathbf{r}, \omega) = -\frac{i\omega}{4\pi\epsilon_0c^2} \frac{e^{ikr}}{r} \hat{\mathbf{k}} \times \hat{\mathbf{k}} \times \int e^{-i\mathbf{k} \cdot \mathbf{r}_s} \mathbf{J}(\mathbf{r}_s, \omega) d^3r_s. \quad (\text{D.14})$$

The integral represents a three-dimensional Fourier transform of the  $\mathbf{J}(\mathbf{r}_s, \omega)$ . Equation D.14 allows one to calculate the electric part of the electromagnetic field in the frequency domain at a point  $\mathbf{r}$ , radiated by the extended current source  $\mathbf{J}$ , while in the far-field approximation ( $kr \gg 1$ ). In arriving at Eq. D.14 ignored the role of the boundary conditions, in other words we assumed that the current is not bounded by a dielectric medium. If a boundary exists around the current distribution, such that the dielectric function is different within and outside of the surface, the solution to the Helmholtz equation (Eq. D.8) by Green's theorem would include derivatives of Green function along the surface normal. As to how exactly this would modify Eq. D.14, depends on the whether the potential (Dirichlet boundary conditions) or

charge distribution (Neumann boundary condition) have been specified at the surface. Approximations relevant to particular cases treated in this dissertation are reviewed in the context of those cases (Chpt. 4, Chpt.5).

### D.3 Dipole radiation

In the previous section (Eq. D.13), we determined the vector potential in the far-field ( $kr \gg 1$ ) of the spatially-extended current source. If the dimension of the source is small compared to the observation distance ( $|\mathbf{r}_s| \ll r$ ), exponent  $\exp(-i\mathbf{k} \cdot \mathbf{r}_s)$  can be expanded in a series:

$$\mathbf{A}(\mathbf{r}, \omega) = \frac{\mu_0}{4\pi} \frac{e^{ikr}}{r} \sum_n \frac{(-ik)^n}{n!} \int \mathbf{J}(\mathbf{r}_s, \omega) (\hat{\mathbf{k}} \cdot \mathbf{r}_s)^n d^3r_s. \quad (\text{D.15})$$

If we are to keep only the leading term of the expansion ( $n=0$ ), the corresponding vector potential becomes:

$$\mathbf{A}(\mathbf{r}, \omega) = \frac{\mu_0}{4\pi} \frac{e^{ikr}}{r} \int \mathbf{J}(\mathbf{r}_s, \omega) d^3r_s. \quad (\text{D.16})$$

After integration by parts [107] and use of a continuity equation  $i\omega\rho = \nabla \cdot \mathbf{J}$ , Eq. D.16 can be written as so:

$$\mathbf{A}(\mathbf{r}, \omega) = -\frac{i\mu_0\omega}{4\pi} \frac{e^{ikr}}{r} \mathbf{p}(\omega), \quad (\text{D.17})$$

where

$$\mathbf{p}(\omega) = \int \mathbf{r}_s \rho(\mathbf{r}_s) d^3r_s \quad (\text{D.18})$$

is the *electric dipole moment*.

Using Eq. D.17 we are in a position to simplify Eq. D.14 for the case of the time-dependent electric dipole:

$$\mathbf{E}(r, \omega) = \frac{k^2}{4\pi\epsilon_0} \frac{e^{ikr}}{r} \hat{\mathbf{k}} \times \hat{\mathbf{k}} \times \mathbf{p}(\omega). \quad (\text{D.19})$$

Due to the condition  $|\mathbf{r}_s| \ll r$ , electric field depends only on the distance  $r$  away from the *point-like* source. By the properties of the Fourier transform, Eq. D.19 implies that the electric field is proportional to the second time derivative of the dipole moment:

$$\mathbf{E}(r, t) \propto \frac{d^2 p(t)}{dt^2}. \quad (\text{D.20})$$

Physically, this means that any extended oscillating current source in the far-field can be approximated to the lowest order as an oscillating “point-source” electric dipole – Hertzian dipole. A Hertzian dipole represents an impulse response (Green function) of the vector diffraction theory. It is in analogy with the impulse response of the scalar diffraction theory – namely Huygen’s wavelet. This analogy becomes even more clear when one considers the respective functional forms of the Hertzian dipole and the Huygen’s wavelet.

Consider the vector product:

$$\hat{\mathbf{k}} \times \hat{\mathbf{k}} \times \hat{\mathbf{p}} = \hat{\mathbf{k}}(\hat{\mathbf{k}} \cdot \hat{\mathbf{p}}) - \hat{\mathbf{p}} \quad (\text{D.21})$$

Without loss of generality, let us take Hertzian dipole  $\hat{\mathbf{p}} = \hat{\mathbf{z}}$ , while  $\hat{\mathbf{k}} = \hat{\mathbf{r}}$  in spherical coordinates, where also  $\hat{\mathbf{r}} \cdot \hat{\mathbf{z}} = \cos \theta$  and  $\hat{\mathbf{z}} = \cos \theta \hat{\mathbf{r}} - \sin \theta \hat{\boldsymbol{\theta}}$ . Equation D.21 becomes:

$$\hat{\mathbf{k}} \times \hat{\mathbf{k}} \times \hat{\mathbf{p}} = \hat{\mathbf{r}}(\hat{\mathbf{r}} \cdot \hat{\mathbf{z}}) - \hat{\mathbf{z}} = \hat{\mathbf{r}} \cos \theta - (\hat{\mathbf{r}} \cos \theta - \hat{\boldsymbol{\theta}} \sin \theta) = \sin \theta \hat{\boldsymbol{\theta}} \quad (\text{D.22})$$

where  $\hat{\boldsymbol{\theta}}$  is the unit vector in spherical coordinates, which lies in the  $\hat{\mathbf{z}} \cdot \hat{\mathbf{r}}$  plane, perpendicular to  $\hat{\mathbf{r}}$ .

The  $\sin \theta$  dependence of the radiated field from the Hertzian dipole is a manifestation of the vectorial nature of the radiated field. But if we were to ignore the vector nature of the dipole, then  $E_{rad} \propto \exp(-ikr)/r$  (Eq. D.17), which is exactly the Huygen’s wavelet.

Huygen’s wavelet is spherically symmetric. Radiation from the Hertzian dipole is polarized in the  $\hat{\boldsymbol{\theta}}$  direction. The field on the axis of the dipole is zero, because

coherent addition of  $\hat{\theta}$  on that line amounts to such. This is the consequence of broken spherical symmetry by the axis of the dipole. In scalar diffraction theory we can approximate Hertzian dipole by the Huygen's wavelet. The vector nature is accounted for with the assumption of the radiated field (Huygen's wavelet) to have the *same* polarization as the source ( $\hat{\mathbf{E}}_{\text{rad}} = \hat{\mathbf{p}}$ ), while the broken spherical symmetry ( $\hat{\mathbf{k}} \times \hat{\mathbf{k}} \times \hat{\mathbf{p}}$ ) is accounted for by the obliquity factor.

# Appendix E

## Dielectric function formalism

### E.1 Plasma frequency

A standard textbook derivation of the plasma frequency is as follows (see for instance Ashcroft and Mermin [110]). Consider electron ensemble of density  $N$  moving some displacing from the equilibrium position by some  $\mathbf{x}$ , with respect to the positive background charge. This sets up the polarization

$$\mathbf{P} = -Nex, \tag{E.1}$$

which leads to the electric field:

$$\mathbf{P} = -\frac{1}{\epsilon_0} \mathbf{E}. \tag{E.2}$$

The equation of motion is then:

$$m\ddot{\mathbf{x}} = e\mathbf{E} = -\frac{Ne^2}{\epsilon_0}\mathbf{x}, \tag{E.3}$$

which is a simple harmonic oscillator<sup>1</sup> of frequency  $\omega_p$ , given by:

$$\omega_p = \sqrt{\frac{Ne^2}{\epsilon_\infty m^*}}, \tag{E.4}$$

---

<sup>1</sup>notation  $\ddot{a}$  represents second derivative of the quantity  $a$  with respect to time  $t$ .

where  $m^*$  stands for an effective mass of the electron, which arises once background positive charge represents a lattice [110, 193]. The constant  $\epsilon_\infty$  arises from the contributions of the valence electrons [153]. The Eq. E.4 is due to Langmuir and defines a *plasma frequency*  $\omega_p$  [194].

## E.2 Local dielectric function

In the case of an isotropic medium, linearized response is:

$$D = 1 + \frac{P}{\epsilon_\infty E}, \quad (\text{E.5})$$

which, with Eq. E.3 lead to:

$$\frac{\epsilon(\omega)}{\epsilon_\infty} = \left( 1 - \frac{\omega_p^2}{\omega^2 + i\gamma\omega} \right). \quad (\text{E.6})$$

Here we include the broadening  $\gamma$ , due to the inelastic scattering processes (electron-phonon scattering, impurity scattering, etc.). Eq. E.6 describes the response of the electron gas to an applied DC field, it is a long-wavelength limit of the dielectric function. In this limit, all electrons respond as a whole, i.e. constituting an incompressible flow. In general,  $\epsilon(\mathbf{k}, \omega)$ , but in the long wavelength limit, the  $\epsilon(\mathbf{k} \rightarrow 0, \omega)$  describes the *local* response of the electron gas.

## E.3 Longitudinal and transverse modes

Plasma, by definition is electrostatically neutral, and hence application of the Gauss law gives:

$$\nabla \cdot \mathbf{D} = 0, \quad (\text{E.7})$$

or equivalently (for isotropic, homogeneous medium):

$$\epsilon(\mathbf{k} \cdot \mathbf{E}_0) = 0, \quad (\text{E.8})$$



where  $\mathbf{E}_0$  and  $\mathbf{k}$  are amplitude and wavevector of the propagating plane-wave mode  $\mathbf{E}(\mathbf{r}, t) = \mathbf{E}_0 \exp[i(\omega t - \mathbf{k} \cdot \mathbf{r})]$ . This condition can be satisfied when either i)  $\mathbf{k} \cdot \mathbf{E}_0 = 0$  or ii)  $\epsilon = 0$ . The former condition defines transverse propagating modes, while the latter corresponds to the longitudinal modes of the system.

### E.3.1 Transverse modes

From the electromagnetic wave equation, the dispersion relation is given by the solutions of  $\epsilon(k, \omega)\omega^2 = c^2 k^2$ , where  $c$  is the speed of light. Using Eq. E.6 and ignoring the broadening, the dispersion relation for the electromagnetic wave inside of a plasma is:

$$\omega = \omega_p^2 + \frac{1}{\epsilon_\infty} c^2 k^2. \quad (\text{E.9})$$

For frequencies below the  $\omega_p$ , electromagnetic wave is attenuated as the wavevector  $k$  of the mode becomes purely imaginary. This is the well-known fact of plasma edge reflectance and has been observed in a number of metals [193]. In passing we note that the role of the background charge has so far been ignored. For frequency of the EM wave that is comparable to the transverse phonon frequency of the lattice, coupling of the two transverse modes occurs and results in a formation of the hybrid mode, termed *polariton*. The manifestation of this coupling is in the dispersion relation that exhibits two branches with the anti-crossing point corresponding to the case when the two frequencies  $\omega$  and  $\omega_{TO}$  would otherwise be identical. This coupling leads to the appearance of the energy gap between the longitudinal optical  $\omega_{LO}$  and transverse optical  $\omega_{TO}$  phonon frequencies, where the wave can not propagate as  $k$  becomes purely imaginary. This gap region is called the *Reststrahlen band* for historical reasons.

### E.3.2 Longitudinal modes

As can be shown [195], the potential  $\Phi$  generated in response to the externally applied potential  $V$  is:

$$\Phi(\mathbf{k}, \omega) = \frac{V(\mathbf{k}, \omega)}{\epsilon(\mathbf{k}, \omega)}. \quad (\text{E.10})$$

From here it is evident that the condition for the longitudinal modes ( $\epsilon = 0$ ) corresponds to a situation when infinitesimal external perturbation  $V$  leads to a large response  $\Phi$ . For instance, longitudinal mode in the limit  $\mathbf{k} \rightarrow 0$  corresponds to (Eq.E.6 with  $\gamma = 0$ ) an oscillation at the plasma frequency  $\omega_p$  – this mode is called *plasmon*. Plasmon is a quantum of the excitation of the electron gas <sup>2</sup>. In case of broadening ( $\gamma \neq 0$ ), longitudinal modes (LM) are manifested by the maxima of the loss function <sup>3</sup>:

$$\text{LM} \equiv \left( -\Im \frac{1}{\epsilon(\mathbf{k}, \omega)} \right) \Big|_{max}. \quad (\text{E.11})$$

## E.4 Non-local response

In general, long-range ( $r^{-2}$ ) Coulomb interaction between the individual electrons modifies the dielectric function. Consider a case when a (locally) excessive charge at  $\mathbf{r}_0$  is formed inside of the plasma region. Coulomb coupling would cause neighboring charges to respond in such a way as to reduce (i.e. *screen*) the total charge in the vicinity of  $\mathbf{r}_0$ . A charge cloud would be formed around the localization, with the spatial distribution decaying exponentially from the center located at  $\mathbf{r}_0$ . Debye has shown that the characteristic length scale of this cloud (Debye radius  $\lambda_D$ ) is inversely proportional to the electron density  $N$ . Bohm and Gross have shown the dispersion

<sup>2</sup>more formal quantum mechanical development can be found for e.g. in Fetter and Walecka [196]

<sup>3</sup>which is proportional to the structure factor within the Born approximation in the quantum-mechanical scattering theory [181]

relation for the longitudinal plasma wave to be:

$$\omega_p^2(k) \simeq \omega_p^2(1 + k^2\lambda_D^2) \quad (\text{E.12})$$

to the quadratic term in the  $k$ . Semiclassical treatment of electron-electron interaction in metals was applied by Thomas and Fermi only to arrive at a similar dispersion relation as Eq. E.12, but with the  $\lambda_D$  being replaced by the  $\sim 1/k_F$ ,  $k_F$  being the radius of the Fermi sphere<sup>4</sup> at low temperatures.

The question of electron-electron interaction is one of the central ones in the quantum theory of many-particle systems [196]. Green function formalism is the most natural way to describe these interactions. This is beyond the scope of this work however and we resort to Lindhard formalism, which allows one to obtain the full dielectric function  $\epsilon(\mathbf{k}, \omega)$  within the *random phase approximation*.

Before we develop the L-M dielectric function we should make a general remark about the dispersion relation of the longitudinal plasma wave. From the argument of Debye or Thomas-Fermi, the screening length introduces a characteristic length scale into the problem. It is therefore natural to anticipate a qualitative change in the behavior of the wave for wavelengths approaching the  $1/k_F$  [197]. In fact, by the virtue of the screening mechanism, for wavelengths smaller than the  $1/k_F$  electronic charge can no longer be “smoothed out” and individual behavior of the charges emerges. In 1946 Lev D. Landau has provided correct solutions to the Vlasov’s transport equation [198], in where he pointed out that the plasma wave will be damped once the wavelength approaches the characteristic screening length. This results in collisionless damping, in the sense that the collective electron behavior is lost and gives rise to individual particle excitations. The reader (or hopefully readers) is/are referred to Chpt. 5, for more detailed discussion of the *Landau damping* in the case of a solid-state plasma.

---

<sup>4</sup>System of  $N$  electrons condenses to  $N/2$  states at  $T = 0$ , which results in a spherical distribution of momentum states for a large number of  $N$  [110].

## E.5 Lindhard dielectric function

Following Ridley [166], consider an external potential  $V_0 \exp(i(\mathbf{q} \cdot \mathbf{r} + \omega t))$  applied to a free-electron gas. Assuming linear response, we can say that the electron density is:

$$N(q, \omega) = F(q, \omega) V_0 \quad (\text{E.13})$$

where  $F(q, \omega)$  is the density-response function and  $q = \mathbf{q} \cdot \hat{\mathbf{r}}$ . The variation in charge density causes an induced potential  $V_{ind}$  (screening). The total potential  $\Phi$  is the sum of the applied and induced potentials and hence:

$$\Phi = V_{ind} + V_0 = \left(1 + \frac{e^2}{\epsilon_0 q^2}\right) V_0 \quad (\text{E.14})$$

where second term in the bracket is the induced potential, obtained from the Poisson equation. Eq. E.13 can be applied to  $\Phi$ :

$$N(q, \omega) = G(q, \omega) \Phi \quad (\text{E.15})$$

where  $G(q, \omega)$  is now the response to the total potential. Note that Eq. E.14 is of the form of Eq. E.10. Reading off the electron-electron interaction  $\epsilon_e(q, \omega)$ :

$$\epsilon_e(q, \omega) = \epsilon_\infty - \frac{e^2}{q^2} G(q, \omega). \quad (\text{E.16})$$

Lindhard has provided a first-order perturbation solution for  $G(q, \omega)$  where:

$$\epsilon_e(\mathbf{q}, \omega) = \epsilon_\infty - \frac{e^2}{|\mathbf{q}|^2} \sum_{\mathbf{k}} \frac{f(E_{\mathbf{k}+\mathbf{q}}) - f(E_{\mathbf{k}})}{E_{\mathbf{k}+\mathbf{q}} - E_{\mathbf{k}} - \hbar\omega - i\hbar\gamma} \quad (\text{E.17})$$

where  $f(E)$  is the energy distribution function and  $\gamma$  is the collisional damping term. Total dielectric function is then:

$$\epsilon(\mathbf{q}, \omega) = \epsilon_\infty + \epsilon_e(\mathbf{q}, \omega) + \frac{\epsilon_0 - \epsilon_\infty}{1 - \left(\frac{\omega}{\omega_{LO}}\right)^2 \frac{\epsilon_0}{\epsilon_\infty}} \quad (\text{E.18})$$

where the last term is the response function of the lattice. Eq. E.18 together with Eq. E.17 fully describe electron-phonon system and the possible modes that can

emerge as a result of interaction. These results are within the *random phase approximation*, which resulted from the assumption that electron density reacts only at the frequency and the wavevector of the externally applied potential.

# References

- [1] J. Pendry. Playing tricks with light. *Science*, 285:1687 – 1688, 1999.
- [2] Yablonovitch E. Photonic crystals: semiconductors of light. *Scientific American*, 285:47 – 55, 2001.
- [3] H.A. Atwater. The promise of plasmonics. *Scientific American*, 296:56 – 63, 2007.
- [4] S. Zhang, W. Fan, N. C. Panoiu, K. J. Malloy, R. M. Osgood, and S. R. J. Brueck. Demonstration of near-infrared negative-index materials. *Physical Review Letters*, 95:137404, 2005.
- [5] M. P. Hasselbeck, D. Stalnaker, L. A. Schlie, T. J. Rotter, A. Stintz, and M. Sheik-Bahae. Emission of terahertz radiation from coupled plasmon-phonon modes in InAs. *Physical Review B*, 65:233303, 2002.
- [6] R. Huber, C. Kübler, Q. T. Vu, H. Haug, S. Tübel, F. Köhler, M.-C. Amann, and A. Leitenstorfer. Femtosecond formation of phonon-plasmon coupled modes in InP: ultrabroadband THz experiment and quantum kinetic theory. *Physical Review Letters*, 94:027401, 2005.
- [7] A. Haché, Y. Kostoulas, R. Atanasov, J. L. P. Hughes, J. E. Sipe, and H. M. van Driel. Observation of coherently controlled photocurrent in unbiased, bulk gaas. *Physical Review Letters*, 78:306–309, 1997.
- [8] M. Sheik-Bahae. Quantum interference control of current in semiconductors: Universal scaling and polarization effects. *Physical Review B, Rapid Communications*, 60:11258–11260, 1999.
- [9] A. J. Huber, F. Keilmann, J. Wittborn, J. Aizpurua, and R. Hillenbrand. Terahertz near-field nanoscopy of mobile carriers in single semiconductor nanodevices. *NanoLetters*, 8:3766–3770, 2008.

- [10] F. Junginger, A. Sell, O. Schubert, B. Mayer, D. Brida, M. Marangoni, G. Cerullo, A. Leitenstorfer, and R. Huber. Single-cycle multiterahertz transients with peak fields above 10 mv/cm. *Optics Letters*, 35:2645–2647, 2010.
- [11] S. Leinß, T. Kampfrath, K. v. Volkman, M. Wolf, J. T. Steiner, M. Kira, S. W. Koch, A. Leitenstorfer, and R. Huber. Terahertz coherent control of optically dark paraexcitons in Cu<sub>2</sub>O. *Physical Review Letters*, 101:246401, 2008.
- [12] P. Gaal, W. Kuehn, K. Reimann, M. Woerner, T. Elsaesser, and R. Hey. Internal motions of a quasiparticle governing its ultrafast nonlinear response. *Nature*, 450:1210–1213, 2007.
- [13] G. Günter, A. A. Anappara, J. Hees, A. Sell, G. Biasiol, L. Sorba, S. De Liberato, C. Ciuti, A. Tredicucci, A. Leitenstorfer, , and R. Huber. Sub-cycle switch-on of ultrastrong lightmatter interaction. *Nature*, 458:178, 2009.
- [14] M. F. DeCamp, D. A. Reis, P. H. Bucksbaum, B. Adams, J. M. Caraher, R. Clarke, C. W. S. Conover, E. M. Dufresne, R. Merlin, V. Stoica, and J. K. Wahlstrand. Coherent control of pulsed x-ray beams. *Nature*, 413:825–828, 2001.
- [15] N. Dudovich, O. Smirnova, J. Levesque, Y. Mairesse, M. Yu. Ivanov, D. M. Villeneuve, and P. B. Corkum. Measuring and controlling the birth of attosecond xuv pulses. *Nature Physics*, 2:781–786, 2006.
- [16] Xiaoshi Zhang, Amy L. Lytle, Tenio Popmintchev, Xibin Zhou, Henry C. Kapteyn, Margaret M. Murnane, and Oren Cohen. Quasi-phase-matching and quantum-path control of high-harmonic generation using counterpropagating light. *Nature Physics*, 3:270–275, 2007.
- [17] Thomas Brabec and Ferenc Krausz. Intense few-cycle laser fields: Frontiers of nonlinear optics. *Review of Modern Physics*, 72(2):545–591, Apr 2000.
- [18] Ferenc Krausz and Misha Ivanov. Attosecond physics. *Review of Modern Physics*, 81(1):163–234, Feb 2009.
- [19] P. B. Corkum and F. Krausz. Attosecond science. *Nature Physics*, 3:381–387, 2007.
- [20] G. A. Mourou, T. Toshiki, and S. V. Bulanov. Optics in the relativistic regime. *Review of Modern Physics*, 78(2):309–371, Apr 2006.
- [21] N. Bloembergen. Chapter 1: From millisecond to attosecond laser pulses. In E. Wolf, editor, *Progress in Optics*, volume 50, pages 1 – 12. Elsevier, 2007.

- [22] M. T. Asaki, C.-P. Huang, D. Garvey, J. Zhou, H. C. Kapteyn, and M. M. Murnane. Generation of 11-fs pulses from a self-mode-locked ti:sapphire laser. *Optics Letters*, 18(12):977–979, June 1993.
- [23] Günther Krauss, Sebastian Lohss, Tobias Hanke, Alexander Sell, Stefan Egger, Rupert Huber, and Alfred Leitenstorfer. Synthesis of a single cycle of light with compact erbium-doped fibre technology. *Nature Photonics*, 4:33–36, 2010.
- [24] Jean-Claude Diels and Wolfgang Rudolph. *Ultrashort Laser Pulse Phenomena*. Academic Press, 2nd edition, 2006.
- [25] A. J. DeMaria, D. A. Stetser, and W. H. Glenn, Jr. Ultrashort light pulses. *Science*, 156:1557–1568, 1967.
- [26] L. E. Hargrove, R. L. Fork, and M. A. Pollack. Locking of He-Ne laser modes induced by synchronous intracavity modulation. *Applied Physics Letters*, 5:4–5, 1964.
- [27] O. G. Peterson, S. A. Tuccio, and B. B. Snavely. cw operation of an organic dye solution laser. *Applied Physics Letters*, 17:245–247, 1970.
- [28] Ferenc Krausz, Martin E. Fermann, Thomas Brabec, Peter F. Curley, Martin Hofer, Manfred H. Ober, Christian Spielmann, Ernst Wintner, and A. J. Schmidt. Femtosecond solid-state lasers. *IEEE Journal of Quantum Electronics*, 28:2097–2121, 1992.
- [29] J. P. Heritage and R. K. Jain. Subpicosecond pulses from a tunable cw mode-locked dye laser. *Applied Physics Letters*, 32:101–103, 1978.
- [30] A. J. DeMaria, D. A. Stetser, and H. Heynau. Self mode-locking of lasers with saturable absorbers. *Applied Physics Letters*, 8:174–176, 1966.
- [31] I. S. Ruddock and D. J. Bradley. Bandwidth-limited subpicosecond pulse generation in modelocked CW dye lasers. *Applied Physics Letters*, 29:296–297, 1976.
- [32] R. L. Fork, B. I. Greene, and C. V. Shank. Generation of optical pulses shorter than 0.1 psec by colliding pulse mode locking. *Applied Physics Letters*, 36:671–672, 1981.
- [33] C. V. Shank, R. L. Fork, R. Yen, R. H. Stolen, and W. J. Tomlinson. Compression of femtosecond optical pulses. *Applied Physics Letters*, 40:761–763, 1982.



- [34] O. E. Martinez, R. L. Fork, and J. P. Gordon. Theory of passively mode-locked lasers including self-phase modulation and group-velocity dispersion. *Optics Letters*, 9:156–158, 1984.
- [35] J. J. Fontaine, W. Dietel, and J.-C. Diels. Chirp in a mode-locked ring dye laser. *IEEE Journal of Quantum Electronics*, 19:1467–1469, 1983.
- [36] R. L. Fork, O. E. Martinez, and J. P. Gordon. Negative dispersion using pairs of prisms. *Optics Letters*, 9:150–152, 1984.
- [37] W. Dietel, J. J. Fontaine, and J.-C. Diels. Intracavity pulse compression with glass: a new method of generating pulses shorter than 60 fsec. *Optics Letters*, 8:4–6, 1983.
- [38] J. A. Valdmanis, R. L. Fork, and J. P. Gordon. Generation of optical pulses as short as 27 femtoseconds directly from a laser balancing self-phase modulation, group-velocity dispersion, saturable absorption, and saturable gain. *Optics Letters*, 10:131–133, 1985.
- [39] H. Knox, R. L. Fork, M. C. Downer, R. H. Stolen, C. V. Shank, and J. A. Valdmanis. Optical pulse compression to 8 fs at a 5-kHz repetition rate. *Applied Physics Letters*, 46:1120–1121, 1985.
- [40] C. V. Shank. Investigation of ultrafast phenomena in the femtosecond time domain. *Science*, 233:1276 – 1280, 1986.
- [41] P. F. Moulton. Spectroscopic and laser characteristics of  $\text{Ti:Al}_2\text{O}_3$ . *Journal of Optical Society of America B*, 3:125–688, 1986.
- [42] E. P. Ippen, H. A. Haus, and L. Y. Liu. Additive pulse mode locking. *Journal of Optical Society of America B*, 6:1736, 1989.
- [43] P. M. French, A. R. Williams, and R. Taylor. Femtosecond pulse generation from a titanium-doped sapphire laser using nonlinear external cavity feedback. *Optics Letters*, 14:686–688, 1989.
- [44] Ursula Keller, Kurt J. Weingarten, Franz X. Kärtner, Daniel Kopf, Bernd Braun, Isabella D. Jung, Regula Fluck, Clemens Hönninger, Nicolai Matuschek, and Juerg Aus der Au. Semiconductor saturable absorber mirrors (SESAMs) for femtosecond to nanosecond pulse generation in solid-state lasers. *IEEE Journal of Selected Topics in Quantum Electronics*, 2:435–453, 1996.
- [45] R. Fluck, I. D. Jung, G. Zhang, F. X. Kärtner, and U. Keller. Broadband saturable absorber for 10-fs pulse generation. *Optics Letters*, 21:743–745, 1996.

- [46] D. E. Spence and W. Sibbett. Femtosecond pulse generation by a dispersion-compensated, coupled-cavity, mode-locked ti:sapphire laser. *Journal of Optical Society of America B*, 8:2053–2060, 1991.
- [47] D. E. Spence, P. N. Kean, and W. Sibbett. 60-fsec pulse generation from a self-mode-locked Ti:sapphire laser. *Optics Letters*, 16:42, 1991.
- [48] Robert Szipöcs, Kárpát Ferencz, Christian Spielmann, and Ferenc Krausz. Chirped multilayer coatings for broadband dispersion control in femtosecond lasers. *Optics Letters*, 19:201–203, 1994.
- [49] Richard Ell, Gregor Angelow, Wolfgang Seitz, Max Lederer, Heinz Huber, Daniel Kopf, Jonathan Birge, and Franz Kärtner. Quasi-synchronous pumping of modelocked few-cycle Titanium Sapphire lasers. *Optics Express*, 13:9292–9298, 2005.
- [50] A. Leitenstorfer, C. Fürst, and A. Laubereau. Widely tunable two-color mode-locked Ti:sapphire laser with pulse jitter of less than 2 fs. *Optics Letters*, 20:916–918, 1995.
- [51] N. Ishii, L. Turi, V. S. Yakovlev, T. Fuji, F. Krausz, A. Baltuška, R. Butkus, G. Veitas, V. Smilgevičius, R. Danielius, and A. Piskarskas. Multimillijoule chirped parametric amplification of few-cycle pulses. *Optics Letters*, 30:567–569, 2005.
- [52] H. Kogelnik and T. Li. Laser beams and resonators. *Applied Optics*, 5:1550–1567, 1966.
- [53] H. Kogelnik, E. Ippen, A. Dienes, and C. Shank. Astigmatically compensated cavities for cw dye lasers. *IEEE Journal of Quantum Electronics*, 8:373–379, 1972.
- [54] S. H. Cho, B. E. Bouma, E. P. Ippen, and J. G. Fujimoto. Low-repetition-rate high-peak-power Kerr-lens mode-locked  $\text{TiAl}_2\text{O}_3$  laser with a multiple-pass cavity. *Optics Letters*, 24:417–419, 1999.
- [55] D. Herriott, H. Kogelnik, and R. Kompfner. Off-axis paths in spherical mirror interferometers. *Applied Optics*, 3:523–526, 1964.
- [56] Maxim S Pshenichnikov, Wim P de Boeij, and Douwe A Wiersma. Generation of 13-fs, 5-MW pulses from a cavity-dumped Ti:sapphire laser. *Optics Letters*, 19:572–574, 1994.
- [57] G N Gibson, R Klank, F Gibson, and B E Bouma. Electro-optically cavity-dumped ultrashort-pulse ti:sapphire oscillator. *Optics Letters*, 21:1055–1057, 1996.

- [58] R. Huber, F. Adler, A. Leitenstorfer, M. Beutter, P. Baum, and E. Riedle. 12-fs pulses from a continuous-wave-pumped 200-nj Ti:sapphire amplifier at a variable repetition rate as high as 4 mhz. *Optics Letters*, 28:2118, 2003.
- [59] Donna Strickland and Gerard Mourou. Compression of amplified chirped optical pulses. *Optics Communications*, 56:219–221, 1985.
- [60] A. Sullivan, H. Hamster, H. C. Kapteyn, S. Gordon, W. White, H. Nathel, R. J. Blair, and R. W. Falcone. Multiterawatt, 100-fs laser. *Optics Letters*, 16:1406–1408, 1991.
- [61] J. D. Kmetec, J. J. Macklin, and J. E. Young. 0.5-tw, 125-fs ti:sapphire laser. *Optics Letters*, 16:1001–1003, 1991.
- [62] Backus Sterling, Charles G. III Durfee, Margaret M. Murnane, and Henry C. Kapteyn. High power ultrafast lasers (review article). *Review of Scientific Instruments*, 69:1207–1223, 1998.
- [63] Robert W. Boyd. *Nonlinear Optics*. Academic Press, 2nd edition, 2003.
- [64] J. A. Giordmaine and R. C. Miller. Tunable coherent parametric oscillation in  $\text{LiNbO}_3$  at optical frequencies. *Physical Review Letters*, 14:973–976, 1965.
- [65] Walter R Bosenberg, Alexander Drobshoff, Jason I Alexander, Lawrence E Myers, and Robert L Byer. 93% pump depletion, 3.5-W continuous-wave, singly resonant optical parametric oscillator. *Optics Letters*, 17:1336–1338, 1996.
- [66] G. K. Samanta and M. Ebrahim-Zadeh. Continuous-wave, single-frequency, solid-state blue source for the 425-489 nm spectral range. *Optics Letters*, 33:1228–1230, 2008.
- [67] C. W. Hoyt, M. Sheik-Bahae, and M. Ebrahimzadeh. High-power picosecond optical parametric oscillator based on periodically poled lithium niobate. *Optics Letters*, 27:1543–1546, 2002.
- [68] Andre Peremans, Dan Lis, Francesca Cecchet, Peter G. Schunemann, Kevin T. Zawilski, and Valentin Petrov. Noncritical singly resonant synchronously pumped OPO for generation of picosecond pulses in the mid-infrared near  $6.4 \mu\text{m}$ . *Optics Letters*, 34:3053–3055, 2009.
- [69] Kent C. Burr, C. L. Tang, Mark A. Arbore, and Martin M. Fejer. High-repetition-rate femtosecond optical parametric oscillator based on periodically poled lithium niobate. *Applied Physics Letters*, 70:3341–3343, 1997.

- [70] R. Gebs, T. Dekorsy, S. A. Diddams, and A. Bartels. 1-GHz repetition rate femtosecond OPO with stabilized offset between signal and idler frequency combs. *Optics Express*, 16:5397–5405, 2008.
- [71] Giulio Cerullo and Sandro De Silvestri. Ultrafast optical parametric amplifiers (Review article). *Review of Scientific Instruments*, 74:1–18, 2003.
- [72] Valentin Petrov, Frank Noack, and Richard Stolzenberger. Seeded femtosecond optical parametric amplification in the mid-infrared spectral region above 3  $\mu\text{m}$ . *Applied Optics*, 36:1164–1172, 1997.
- [73] Valentin Petrov, Frank Noack, Pancho Tzankov, Masood Ghotbi, Majid Ebrahim-Zadeh, Ivailo Nikolov, and Ivan Buchvarov. High-power femtosecond optical parametric amplification at 1 kHz in  $\text{BiB}_3\text{O}_6$  pumped at 800 nm. *Optics Express*, 15:556–563, 2007.
- [74] H. Hellwig, J. Liebertz, and L. Bohaty. Exceptional large nonlinear optical coefficients in the monoclinic bismuth borate  $\text{BiB}_3\text{O}_6$  (BIBO). *Solid State Communications*, 109:249–251, 1999.
- [75] M. Ghotbi and M. Ebrahim-Zadeh. Femtosecond nonlinear frequency conversion based on  $\text{BiB}_3\text{O}_6$ . *Optics Express*, 12:6002–6019, 2004.
- [76] A.V. Smith. SNLO nonlinear optics code. computer code by AS-Photonics.
- [77] M. Ghotbi, M. Ebrahim-Zadeh, V. Petrov, P. Tzankov, and F. Noack. Efficient 1kHz femtosecond optical parametric amplification in  $\text{BiB}_3\text{O}_6$  pumped at 800 nm. *Optics Express*, 14:10621–10626, 2006.
- [78] V. Petrov, M. Ghotbi, O. Kokabee, A. Esteban-Martin, F. Noack, A. Gaydardzhiev, I. Nikolov, P. Tzankov, I. Buchvarov, K. Miyata, A. Majchrowski, I.V. Kityk, F. Rotermund, E. Michalski, and M. Ebrahim-Zadeh. Femtosecond nonlinear frequency conversion based on  $\text{BiB}_3\text{O}_6$ . *Laser and Photonics Reviews*, 4:53–98, 2009.
- [79] Jean-Claude M. Diels, Joel J. Fontaine, Ian C. McMichael, and Francesco Simoni. Control and measurement of ultrashort pulse shapes (in amplitude and phase) with femtosecond accuracy. *Applied Optics*, 24:1270–1282, 1985.
- [80] A. Dubietis, G. Jonušauskas, and A. Piskarskas. Powerful femtosecond pulse generation by chirped and stretched pulse parametric amplification in BBO crystal. *Optics Communications*, 88:437–440, 1992.
- [81] Franz Tavella, Yutaka Nomura, Laszlo Veisz, Vladimir Pervak, Andrius Marcinkevičius, and Ferenc Krausz. Dispersion management for a sub-10-fs, 10

- TW optical parametric chirped-pulse amplifier. *Optics Letters*, 32:2227–2229, 2007.
- [82] W. Herschel. Experiments on the refrangibility of the invisible rays of the sun. *Philosophical Transactions*, 90:284–288, 1800.
- [83] R. Bowling Barnes and Lyman G. Bonner. A survey of infra-red spectroscopy. I. the early history and the methods of infra-red spectroscopy. *Journal of Chemical Education*, 14:564–571, 1937.
- [84] S.P. Langley. *Proceedings of the American Academy of Arts and Sciences*, 16:342, 1881.
- [85] Merriam-Webster Online Dictionary. "bolometer". <http://www.merriam-webster.com/dictionary/bolometers>.
- [86] S.P. Langley. *Annals of the Astrophysical Observatory of the Smithsonian Institution, Volume I*. Washington, Government Printing Office, 1900.
- [87] M.F. Kimmitt. Restrahlen to T-rays 100 years of terahertz radiation. *Journal of Biological Physics*, 29:77–85, 2003.
- [88] Ernest Fox Nichols. A method for energy measurements in the infra-red spectrum and the properties of the ordinary ray in quartz for waves of great wave length. *Physical Review (Series I)*, 4:297–313, 1897.
- [89] J. M. Chamberlain. Where optics meets electronics: recent progress in decreasing the terahertz gap. *Philosophical Transactions of the Royal Society A (London)*, 362:199–213, 2004.
- [90] H. Rubens and E. F. Nichols. Certain optical and electro-magnetic properties of heat waves of great wave-length, I. *Physical Review (Series I)*, 5:98–112, 1897.
- [91] H. Rubens and E. F. Nichols. Certain properties of heat waves of great wave-length. II. *Physical Review (Series I)*, 5:152–169, 1897.
- [92] M.J.E. Golay. Certain properties of heat waves of great wave-length. II. *Review of Scientific Instruments*, 18:357–362, 1947.
- [93] E.H. Putley. Impurity photoconductivity in n-type InSb. *Proceedings of the Physical Society*, 76:802–805, 1960.
- [94] F.J. Low. Low-temperature Germanium bolometer. *Journal of Optical Society of America*, 51:1300–1304, 1961.

- [95] A. Glagolewa-Arkadiewa. Short electromagnetic waves of wavelength up to 82  $\mu\text{m}$ . *Nature*, 113:640, 1924.
- [96] W.C. King and M. Gordy. One-to-two millimeter wave spectroscopy. *Physical Review*, 93:407–412, 1954.
- [97] Matthias Hoffmann. *Novel Techniques in THz-Time-Domain-Spectroscopy*. Doctoral dissertation, Universität Freiburg im Breisgau, 2006.
- [98] T. Y. Chang, T. J. Bridges, and E. G. Burkhardt. Cw submillimeter laser action in optically pumped methyl fluoride, methyl alcohol, and vinyl chloride gases. *Applied Physics Letters*, 17:249–251, 1970.
- [99] Eric R. Mueller, William E. Jr. Robotham, Richard P. Meisner, Richard A. Hart, John Kennedy, and Leon A. Newman. 2.5 THz laser local oscillator for the EOS Chem 1 satellite. In *Proceedings*, volume 1101 of *Ninth International Symposium on Space Terahertz Technology*, page 563, 1998.
- [100] R.F Kazarinov and R.A. Suris. Possibility of amplification of electromagnetic waves in a semiconductor with a superlattice. *Fizika i Tehnika Poluprovodnikov*, 5:797–800, 1971.
- [101] B. S. Williams. Terahertz quantum-cascade lasers. *Nature Photonics*, 1:517–525, 2007.
- [102] Kodo Kawase, Manabu Sato, Tetsuo Taniuchi, and Hiromasa Ito. Coherent tunable thz-wave generation from  $\text{LiNbO}_3$  with monolithic grating coupler. *Applied Physics Letters*, 68:2483, 1996.
- [103] E. R. Brown, K. A. McIntosh, F. W. Smith, M. J. Manfra, and C. L. Dennis. Measurements of optical-heterodyne conversion in low-temperature-grown GaAs. *Applied Physics Letters*, 62:1206–1208, 1993.
- [104] B. A. Anicin. Reading Hertz's own dipole theory. *European Journal of Physics*, 29:15–23, 2008.
- [105] D. H. Auston, K. P. Cheung, and P. R. Smith. Picosecond photoconducting Hertzian dipoles. *Applied Physics Letters*, 45:284–286, 1984.
- [106] Ch. Fattinger and D. Grischkowsky. Terahertz beams. *Applied Physics Letters*, 54:490–492, 1989.
- [107] John David Jackson. *Classical electrodynamics*. John Wiley & Sons, 3rd edition, 1999.
- [108] K. Sakai. *Terahertz Optoelectronics*. Springer, 2005.

- [109] Yun-Shik Lee. *Principles of Terahertz science and technology*. Springer, 2009.
- [110] N.W. Ashcroft and N.D. Mermin. *Solid State Physics*. Harcourt College Publishers, 1976. p. 228.
- [111] E. Castro-Camus, J. Lloyd-Hughes, and M.B. Johnston. Three-dimensional carrier-dynamics simulation of terahertz emission from photoconductive switches. *Physical Review B*, 71:195301, 2005.
- [112] Menlo Systems GmbH. Online document: Tera8-1 thz-antennas, August 2010.
- [113] Lionel Duvillaret, Frédéric Garet, Jean-François Roux, and Jean-Louis Coutaz. Analytical modeling and optimization of terahertz time-domain spectroscopy experiments using photoswitches as antennas. *IEEE journal on selected topics in quantum electronics*, 7:615–623, 2001.
- [114] M. Bass, P. A. Franken, J. F. Ward, and G. Weinreich. Optical rectification. *Physical Review Letters*, 9:446–448, 1962.
- [115] D. H. Auston. Subpicosecond electro-optic shock waves. *Applied Physics Letters*, 43:713–715, 1983.
- [116] D. H. Auston, K. P. Cheung, J. A. Valdmanis, and D. A. Kleinman. Cherenkov radiation from femtosecond optical pulses in electro-optic media. *Physical Review Letters*, 53:1555–1558, 1984.
- [117] János Hebling, Ka-Lo Yeh, Matthias C. Hoffmann, Balázs Bartal, and Keith A. Nelson. Generation of high-power terahertz pulses by tilted-pulse-front excitation and their application possibilities. *Journal of Optical Society of America B*, 25:B6–B19, 2008.
- [118] Ajay Nahata, Aniruddha S. Weling, and Tony F. Heinz. A wideband coherent terahertz spectroscopy system using optical rectification and electro-optic sampling. *Applied Physics Letters*, 69:2321–2323, 1996.
- [119] Martin van Exter, Ch. Fattinger, and D. Grischkowsky. Terahertz time-domain spectroscopy of water vapor. *Optics Letters*, 14:11281130, 1989.
- [120] Q. Wu and X.-C. Zhang. 7 terahertz broadband GaP electro-optic sensor. *Applied Physics Letters*, 70:1784–1786, 1997.
- [121] A. Rice, Y. Jin, X. F. Ma, X.-C. Zhang, D. Bliss, J. Larkin, and M. Alexander. Terahertz optical rectification from  $\langle 110 \rangle$  zinc-blende crystals. *Applied Physics Letters*, 64:1324–1326, 1994.

- [122] Konstantin L. Vodopyanov. Optical generation of narrow-band terahertz packets in periodically inverted electro-optic crystals: conversion efficiency and optimal laser pulse format. *Optics Express*, 14:2263–2276, 2006.
- [123] C. Kübler, S. Huber, R. Tübel, and A. Leitenstorfer. Ultrabroadband detection of multi-terahertz field transients with GaSe electro-optic sensors: Approaching the near infrared. *Applied Physics Letters*, 85:3360–3362, 2004.
- [124] P. Y. Han, M. Tani, F. Pan, and X.-C. Zhang. Use of the organic crystal DAST for terahertz beam applications. *Optics Letters*, 25:675–1837, 2000.
- [125] C. Kübler, R. Huber, and A. Leitenstorfer. Ultrabroadband terahertz pulses: generation and field-resolved detection. *Semiconductor Science and Technology*, 20:S128–S133, 2005.
- [126] A. Sell, A. Leitenstorfer, and R. Huber. Phase-locked generation and field-resolved detection of widely tunable terahertz pulses with amplitudes exceeding 100 MV/cm. *Optics Letters*, 33:2767–2769, 2008.
- [127] Shun Lien Chuang, Stefan Schmitt-Rink, Benjamin I. Greene, Peter N. Saeta, and Anthony F. J. Levi. Optical rectification at semiconductor surfaces. *Physical Review Letters*, 68:102–105, 1992.
- [128] R. Kersting, K. Unterrainer, G. Strasser, H. F. Kauffmann, and E. Gornik. Few-cycle thz emission from cold plasma oscillations. *Physical Review Letters*, 79:3038–3041, 1997.
- [129] G.C. Cho, W. Kütt, and H. Kurz. Subpicosecond time-resolved coherent-phonon oscillations in GaAs. *Physical Review Letters*, 65:764–766, 1990.
- [130] E.W. Weisstein. *Millimeter/Submillimeter Fourier Transform Spectroscopy of Jovian Planet Atmospheres*. Doctoral dissertation, California Institute of Technology, 1996.
- [131] R. Winston. Light collection within the framework of geometric optics. *Journal of Optical Society of America*, 60:245–247, 1970.
- [132] H. Harde, Søren Keiding, and D. Grischkowsky. THz commensurate echoes: Periodic rephasing of molecular transitions in free-induction decay. *Physical Review Letters*, 66(14):1834–1837, 1991.
- [133] P. Y. Han, M. Tani, M. Usami, S. Kono, R. Kersting, and X.-C. Zhang. A direct comparison between terahertz time-domain spectroscopy and far-infrared fourier transform spectroscopy. *Journal of Applied Physics*, 89:2357–2359, 1999.



- [134] G. Gallot, Jiangquan Zhang, R. W. McGowan, Tae-In Jeon, and D. Grischkowsky. Measurements of the THz absorption and dispersion of ZnTe and their relevance to the electro-optic detection of THz radiation. *Applied Physics Letters*, 74:3450–3452, 1999.
- [135] A. Leitenstorfer, S. Hunsche, J. Shah, M. C. Nuss, and W. H. Knox. Detectors and sources for ultrabroadband electro-optic sampling: Experiment and theory. *Applied Physics Letters*, 74:1516–1518, 1999.
- [136] J. Valdmanis, G. Mourou, and C. Gobel. Subpicosecond electrical sampling. *IEEE Journal of Quantum Electronics*, 19:664–667, 1983.
- [137] Q. Wu and X.-C. Zhang. Free-space electro-optic sampling of terahertz beams. *Applied Physics Letters*, 67:3523–3525, 1995.
- [138] A. Pashkin, M. Porer, M. Beyer, K. W. Kim, A. Dubroka, C. Bernhard, X. Yao, Y. Dagan, R. Hackl, A. Erb, J. Demsar, R. Huber, and A. Leitenstorfer. Femtosecond response of quasiparticles and phonons in superconducting  $\text{YBa}_2\text{Cu}_3\text{O}_{7-\delta}$  studied by wideband terahertz spectroscopy. *Physical Review Letters*, 105(6):067001, 2010.
- [139] Uwe Bovensiepen. A real-time view of elementary excitations in high- $T_c$  superconductors. *Physics*, 3:63, Aug 2010.
- [140] Alexander Sell, Tobias Kampfrath, Gregor Klatt, Sebastian Mhrlein, Alexej Pashkin, Manfred Fiebig, Thomas Dekorsy, Martin Wolf, Rupert Huber, and Alfred Leitenstorfer. Ultrafast coherent control of spin waves with intense terahertz magnetic transients. In *Conference on Lasers and Electro-Optics (CLEO): Joint CLEO/QELS Symposium on Quantum Control I*, volume JThC, page 2, 2010.
- [141] R. E. Slusher, W. Giarat, and S. R. J. Brueck. Multiphoton-injected plasmas in insb. *Physical Review*, 183:758, 1969.
- [142] E. Gornik and R. Kersting. Coherent thz emission in semiconductors. *Semiconductors and Semimetals*, K. T. Tsen, ed., 67:389–434, 2001.
- [143] W. Sha, A. L. Smirl, and W. F. Tseng. Coherent plasma oscillations in bulk semiconductors. *Physical Review Letters*, 74:4273–4277, 1995.
- [144] G. C. Cho, T. Dekorsy, H. J. Bakker, R. Hövel, and H. Kurz. Generation and relaxation of coherent majority plasmons. *Physical Review Letters*, 77:4062–4065, 1996.
- [145] R. Kersting, J. N. Heyman, G. Strasser, and E. Gornik. Coherent plasmons in n-doped GaAs. *Physical Review B*, 58:4553–4559, 1998.

- [146] T. Dekorsy, H. Auer, C. Waschke, H. J. Bakker, H. G. Roskos, H. Kurz, V. Wagnener, and P. Grosse. Emission of submillimeter electromagnetic waves by coherent phonons. *Physical Review Letters*, 74:738–742, 1995.
- [147] P. Gu, M. Tani, S. Kono, K. Sakai, and X.-C. Zhang. Study of terahertz radiation from inas and insb. *Journal of Applied Physics*, 51:5533–5537, 2002.
- [148] M. B. Johnston, D. M. Whittaker, A. Corchia, A. G. Davies, and E. H. Linfield. Simulation of terahertz generation at semiconductor surfaces. *Physical Review B*, 65:165301, 2002.
- [149] J. N. Heyman, A. Coates, N. Reinhardt, and G. Strasser. Diffusion and drift in terahertz emission at GaAs surfaces. *Applied Physics Letters*, 83:5476–5478, 2003.
- [150] M. P. Hasselbeck, L. A. Schlie, and D. Stalnaker. Emission of electromagnetic radiation by coherent vibrational waves in stimulated Raman scattering. *Applied Physics Letters*, 85:173–175, 2004.
- [151] D. E. Aspnes and A. A. Studna. Dielectric functions and optical parameters of Si, Ge, GaP, GaAs, GaSb, InP, InAs, and InSb from 1.5 to 6.0 eV. *Physical Review B*, 27:985–1009, 1983.
- [152] A. V. Kuznetsov and C. J. Stanton. Coherent phonon oscillations in gaas. *Phys. Rev. B*, 51:7555–7565, 1995.
- [153] P.Y. Yu and M. Cardona. *Fundamentals of Semiconductors*. Springer, 1999. 2nd edition, p. 283.
- [154] S. R. J. Brueck. Radiation from a dipole embedded in a dielectric slab. *IEEE Journal of Selected Topics in Quantum Electronics*, 6:899–628, 2000.
- [155] Shigehiko Sasa, Shinya Umino, Yutaro Ishibashi, Toshihiko Maemoto, Masataka Inoue, Kei Takeya, and Masayoshi Tonouchi. Intense terahertz radiation from inas thin films. *Journal of Infrared, Millimeter and Terahertz Waves*, pages 1–9, 2010. 10.1007/s10762-010-9694-0.
- [156] J. Shan, C. Weiss, R. Wallenstein, R. Beigang, and T. F. Heinz. Simulation of terahertz generation at semiconductor surfaces. *Optics Letters*, 26:849–851, 2001.
- [157] M. B. Johnston, D. M. Whittaker, A. Dowd, A. G. Davies, E. H. Linfield, X. Li, and D. A. Ritchie. Generation of high-power terahertz pulses in a prism. *Optics Letters*, 27:1935–1937, 2002.

- [158] G. Klatt, F. Hilser, W. Qiao, M. Beck, R. Gebbs, A. Bartels, K. Huska, U. Lemmer, G. Bastian, M.B. Johnston, M. Fischer, J. Faist, and T. Dekorsy. Terahertz emission from lateral photo-Dember currents. *Optics Express*, 18:4939–4947, 2010.
- [159] M. Joffre, A. Bonvalet, and J.-L. Martin. Femtosecond diffracting fourier-transform infrared interferometer. *Optics Letters*, 21:964–966, 1996.
- [160] Michael P. Hasselbeck, L. A. Schlie, and D. Stalnaker. Coherent plasmons in insb. *Applied Physics Letters*, 85:6116 – 6118, 2004.
- [161] P. C. Mathur, N. D. Kataria, Sushi Jain, and Vijender Sharma. Electron mobility in n-InSb from 77 to 300 K. *Journal of Physics C: Solid State Physics*, 9:L89–L91, 1976.
- [162] E. H. Putley. Electrical conduction in n-type insb between 20k and 300ok. *Proc. Phys. Soc.*, 73:280 – 290, 1959.
- [163] M. P. Hasselbeck and P. M. Enders. Electron-electron interactions in the non-parabolic conduction band of narrow-gap semiconductors. *Physical Review B*, 57:9674, 1998.
- [164] M. Hase, S. Nakashima, K. Mizoguchi, H. Harima, and K. Sakai. Ultrafast decay of coherent plasmonphonon coupled modes in highly doped GaAs. *Physical Review B*, 60:16526–16530, 1999.
- [165] T. Dekorsy, H. Auer, H. J. Bakker, H. G. Roskos, and H. Kurz. THz electromagnetic emission by coherent infrared-active phonons. *Physical Review B*, 53:4005–4014, 2001.
- [166] B.K. Ridley. *Quantum processes in semiconductors*. Oxford University Press, 1999.
- [167] J. H. Malmberg and C. B. Wharton. Collisionless damping of large-amplitude plasma waves. *Physical Review Letters*, 19:775–778, 1967.
- [168] G. Abstreiter, M. Cardona, and A. Pinczuk. Collisionless damping of large-amplitude plasma waves. *Light Scattering in Solids IV*, 1:5–150, 1984.
- [169] G. R. Bell, C. F. McConville, and T. S. Jones. Plasmon excitations and accumulation layers in heavily doped InAs(001). *Physical Review B*, 54:2654–2661, 1996.
- [170] M.P. Hasselbeck, D. Seletskiy, L.R. Dawson, and M. Sheik-Bahae. Direct observation of Landau damping in a solid state plasma. *Physica Status Solidi (c)*, 5:253–256, 2008.

- [171] G. Schider, J. R. Krenn, A. Hohenau, H. Ditlbacher, A. Leitner, F. R. Aussenegg, W. L. Schaich, I. Puscasu, B. Monacelli, and G. Boreman. Plasmon dispersion relation of Au and Ag nanowires. *Physical Review B*, 68:155427, 2003.
- [172] E. Conwell. *High Field Transport in Semiconductors*. Academic Press, 1967.
- [173] J. E. Smith, M. I. Nathan, J. C. McGroddy, S. A. Porowski, and W. Paul. Gunn effect in n-type InSb. *Applied Physics Letters*, 28:242–245, 1969.
- [174] B. B. Hu, E. A. de Souza, W. H. Knox, J. E. Cunningham, M. C. Nuss, A. V. Kuznetsov, and S. L. Chuang. Identifying the distinct phases of carrier transport in semiconductors with 10 fs resolution. *Physical Review Letters*, 74:1689–1692, 1995.
- [175] H. Ahn, Y.-P. Ku, Y.-C. Wang, and C.-H. Chuang. Terahertz emission from vertically aligned InN nanorod arrays. *Applied Physics Letters*, 91:132108, 2007.
- [176] Gyeong Bok Jung, Yong Jae Cho, Yoon Myung, Han Sung Kim, Young Suk Seo, Jeunghye Park, and Chul Kang. Geometry-dependent terahertz emission of silicon nanowires. *Optics Express*, 18:16353–16359, 2010.
- [177] J. M. Woodall, J. L. Freeouf, G. D. Pettit, T. Jackson, and P. Kirchner. Ohmic contacts to n-GaAs using graded band gap layers of  $\text{Ga}_{1-x}\text{In}_x\text{As}$  grown by molecular beam epitaxy. *Journal of Vacuum Science and Technology*, 19:626–628, 1981.
- [178] Denis Seletskiy, Michael P. Hasselbeck, Mansoor Sheik-Bahae, Jeffrey G. Cederberg, Linus C. Chuang, Michael Moewe, and Connie J. Chang-Hasnain. Observation of THz emission from InAs nanowires. In *Conference on Lasers and Electro-Optics*, volume CMM, page 2, 2008.
- [179] A.A. Talin, F. Léonard, A. M. Katzenmeyer, B. S. Swartzentruber, M. E. Picraux, S. T. Toimil-Molares, J. G. Cederberg, X. Wang, S. D. Hersee, and A. Rishinaramangalum. Transport characterization in nanowires using an electrical nanoprobe. *Semiconductor Science and Technology*, 25:024015, 2010.
- [180] A. A. Talin, F. Léonard, B. S. Swartzentruber, X. Wang, and S. D. Hersee. Transport characterization in nanowires using an electrical nanoprobe. *Physical Review Letters*, 101:076802, 2008.
- [181] Pitarke. J. M., J. B. Pendry, and P. M. Echenique. Electron energy loss in composite systems. *Physical Review B*, 55:9550–9557, 1995.

- [182] Harald Ditlbacher, Andreas Hohenau, Dieter Wagner, Uwe Kreibig, Michael Rogers, Ferdinand Hofer, Franz R. Aussenegg, and Joachim R. Krenn. Silver nanowires as surface plasmon resonators. *Physical Review Letters*, 95:257403, 2005.
- [183] R. Atanasov, A. Haché, J. L. P. Hughes, H. M. van Driel, and J. E. Sipe. Coherent control of photocurrent generation in bulk semiconductors. *Physical Review Letters*, 76:1703–1706, 1996.
- [184] J.B. Khurgin. Generation of the terahertz radiation using  $\chi^{(3)}$  in semiconductor. *Journal of Nonlinear Optical Physics and Materials*, 4:163–189, 1995.
- [185] C. Aversa and J.E. Sipe. Coherent current control in semiconductors: a susceptibility perspective. *IEEE Journal of Quantum Electronics*, 32:1570–1573, 1996.
- [186] D. J. Cook and R. M. Hochstrasser. Intense terahertz pulses by four-wave rectification in air. *Optics Letters*, 25:1210–1212, 2000.
- [187] Xu Xie, Jianming Dai, and X.-C. Zhang. Coherent control of THz wave generation in ambient air. *Physical Review Letters*, 96:075005, 2006.
- [188] A. Haché, J. E. Sipe, and H. M. van Driel. Quantum interference control of electrical currents in GaAs. *IEEE Journal of Quantum Electronics*, 34:1144–1154, 1998.
- [189] A. N. Chudinov, Yu. E. Kapitzky, A. A. Shulinov, and B. Ya. Zel'dovich. Interferometric phase measurements of average field cube  $E_{\omega}^2 E_{2\omega}^*$ . *Optical and Quantum Electronics*, 23:1055–1060, 1991.
- [190] Jianming Dai, Nicholas Karpowicz, and X.-C. Zhang. Coherent polarization control of terahertz waves generated from two-color laser-induced gas plasma. *Physical Review Letters*, 103:023001, 2009.
- [191] Haidan Wen and Aaron M. Lindenberg. Coherent terahertz polarization control through manipulation of electron trajectories. *Physical Review Letters*, 103:023902, 2009.
- [192] Joseph T. Verdeyen. *Laser Electronics*. Prentice Hall, 3rd edition, 1995.
- [193] W. G. Spitzer and H. Y. Fan. Determination of optical constants and carrier effective mass of semiconductors. *Physical Review*, 106:882–890, 1957.
- [194] Lewi Tonks and Irving Langmuir. Oscillations in ionized gases. *Physical Review*, 33:195–210, 1929.

- [195] J.M. Ziman. *Principles of the theory of solids*. Cambridge University Press, 1965.
- [196] Alexander L. Fetter and John Dirk Walecka. *Quantum theory of many-particle systems*. Dover, 2003.
- [197] A.A. Abrikosov, L.P. Gorkov, and I.E. Dzyaloshinski. *Methods of quantum field theory in statistical physics*. Dover, 1963.
- [198] L. Landau. On the vibrations of the electronic plasma. *Journal of Physics (Moscow)*, 10:25–34, 1946.